Doctoral Dissertation
Doctoral Program in Bioengineering and Medical-Surgical Sciences (38th Cycle)

Investigation of PCL/Bioactive Glass and PCL/Alumina-Toughened Zirconia Composites for Bone Tissue Engineering

Surface, Mechanical, and Biological Characterization

Riccardo Pedraza

Supervisors
Prof. Federico Mussano, Supervisor
Prof. Alessandro Massè, Co-Supervisor

Politecnico di Torino
2025

I hereby declare that, the contents and organisation of this dissertation constitute my own original work and does not compromise in any way the rights of third parties, including those relating to the security of personal data.

…….....

Riccardo Pedraza

Turin, 2025

I would like to dedicate this thesis to my loving parents

Abstract

An important worldwide health concern is bone abnormalities, which can be caused by ageing, illness, or sports-related accidents. In order to address these problems, bone tissue engineering is a novel, interdisciplinary strategy that aims to improve patients' quality of life and heal bone abnormalities. Scaffolds are essential to this method because they function as three-dimensional (3D) structures that guide cell adhesion during the formation of bone tissue. Scaffold performance is greatly influenced by variables such as mechanical strength, physicochemical properties, and pore size. Porous bone scaffolds are made using a variety of methods, but 3D printing technology is drawing a lot of attention because of its potential to completely change the manufacturing industry. Benefits from this process include fast prototyping, flexible design, waste reduction, customisation at scale and economical manufacture of complex structures. Otolaryngology/maxillofacial surgery and dentistry are two medical specialities where 3D printing has had a revolutionary effect.

Among the various materials that can be used in 3D printing, polymers are undoubtedly the most versatile. Although polymer materials provide mechanical performance concerns, they have solved certain cost challenges. Porous scaffolds for bone tissue engineering have been produced by several industrial 3D printers during the past ten years. A rising number of articles have compared the growth of 3D printing to the third industrial revolution.

Because it is lightweight and inexpensive, polycaprolactone (PCL) is often utilised as polymer materials for tissue engineering scaffolds, in particular, thanks to its biodegradability and biocompatibility, it could be used as bone substitute in regenerative medicine. Our current study has focused on identifying and evaluating several PCL-based polymer blends for use in the creation of 3D scaffolds. Toughening ceramic fillers like Alumina toughened zirconia (ATZ) and fillers with distinguishing properties, including silica-based bioactive glasses with and without copper (SBA3/SBA3_Cu), have been used in these formulations. Adipose Tissue-Derived Stem Cells (ASC52 hTERT), Dermal Microvascular Endothelial Cells (HMEC-1), palatal fibroblasts (PF), epithelial cell (SG), have been used to evaluate the biological response to the different compounds.

Samples were studied to test biocompatibility using viability tests with an illuminometer, adhesion and spreading tests using a fluorescence microscopy. From a material perspective, surface morphology was studied using SEM and mechanical properties were investigated using a dynamometer.

For the PCL/SBA3 and PCL/SBA3_Cu systems, incorporating bioactive glass improved the scaffolds' physicochemical and biological properties without compromising flexibility. Copper-doped SBA3 enhanced endothelial cell proliferation through the release of angiogenic ions, while undoped SBA3 promoted mesenchymal stem cell growth, highlighting the potential of these composites for simultaneous bone and vessel formation. Future studies should focus on 3D

scaffolds under dynamic culture to identify the optimal composition and assess long-term osteogenic and angiogenic effects, followed by in vivo validation.

For the PCL/ATZ composites, two mixing techniques solvent casting and impact milling were compared. Solvent casting produced better mechanical and biological results, particularly for PCL/ATZ 80/20, which showed high cell proliferation and balanced properties. In contrast, dry mixing caused polymer degradation and poorer performance. Notably, PCL/ATZ 80/20 also exhibited strong potential for dental applications, improving epithelial and fibroblast adhesion, thus supporting its use in enhancing the mucosal seal of dental implants.

Overall, this work demonstrated that by combining polymers with bioactive or ceramic fillers and optimizing processing, it is possible to create multifunctional composite biomaterials tailored for both bone tissue regeneration.

Table of contents

List of Figures III

List of Tables V

1. Introduction 1

1.1. Regenerative medicine: context and state of the art 1
1.2. Scaffolds 2
1.3. Biomaterials 5

1.3.1. Natural biomaterials 6
1.3.2. Synthetic biomaterials 7

1.4. Polycaprolactone 10

1.4.1. PCL synthesis 11
1.4.2. Physicochemical PCL properties 12
1.4.3. Mechanical properties of PCL 13
1.4.4. Surface PCL properties 14
1.4.5. PCL degradation properties 14

1.5. PCL as a polymer matrix in composite materials 16
1.6. Solvent casting technique 16
1.7. Additive manufacturing in bone tissue engineering 18

1.7.1. Fused Deposition Modelling 18
1.7.2. Selective Laser Sintering 19
1.7.3. Stereolithography 19

1.8. Stem cells for tissue engineering 20

1.8.1. Mesenchymal stem/stromal cells 21
1.8.1.1. Adipose-derived stem cells 21
1.8.1.2. Human Microvascular Endothelial Cells 22

1.9. Project purpose 22

2. Materials and methods 23

2.1. Sample Preparation 23
2.2. Microscopy 27
2.3. Roughness 27
2.4. Contact Angle and Surface Free Energy Evaluation 27
2.5. Protein Adsorption 28
2.7. Ion release 28

2.8. Gel Permeation Chromatography 29
2.9. Mechanical properties 29
2.10. Cell experiments 29
2.10.1. Cell Culture 29
2.10.2. Cell Adhesion and Cell Spreading 30
2.10.3. Cell Viability 31
2.11. Data management 31
3. Results 32
3.1. Microscopy 32
3.1.1. Morphology of compounds with bioactive glass 32
3.1.2. Morphology of compounds containing ATZ 33
3.1.3. Different morphologies between solvent casting and solid mixing 34
3.2. Roughness 36
3.2.1. Bioactive glass compounds surface roughness 36
3.2.2. ATZ compounds surface roughness 37
3.3. Contact angle and SFE 38
3.3.1 Bioactive glasses contact angles and SFE 38
3.3.2. ATZ compounds contact angles and SFE 39
3.4. Protein adsorption 41
3.4.1. PCL/SBA3 composites materials protein affinity 41
3.4.2. PCL/ATZ compounds protein affinity 41
3.5. Culture medium ions analysis 42
3.6. GPC 43
3.7. Mechanical characterization 44
3.7.1. PCL/SBA3 mechanical behaviour 44
3.7.2. PCL/ATZ mechanical tests 45
3.8. Materials biocompatibility 46
3.8.1. PCL/SBA3 early cell adhesion and morphology 46
3.8.2. PCL/ATZ early biological behaviour 48
3.9. Viability assays 51
3.9.1. Long term viability of PCL/SBA3 composites materials 51
3.9.2. Long term behaviour of PCL/ATZ compounds 51
4. Discussion 54
5. Conclusion 61
Bibliography 63

List of Figures

1. Scheme representing bone graft classification.
2. Example of a 3D scaffold before (left) and after (right) seeding the cells.
3. Image representing principal natural biomaterials: (a) bacterial cellulose, (b) collagen and (c) decellularized extracellular matrix.
4. Scheme representing two principal methods of Polycaprolactone synthesis.
5. Oxidation process of 6-hydroxyhexanoic acid to obtain Acetyl-CoA and enter the Krebs cycle metabolic pathway.
6. FDM system architecture.
7. SLS conceptual structure.
8. SLA framework.
9. Mesenchymal stem/stromal cells multipotency.
10. Schematic representation of PCL/ATZ composites materials: (a) solvent casting, (b) impact milling.
11. Schematic representation of PCL/Bioactive glass compounds.
12. Schematic representation of 3D printing process.
13. SEM images of PCL/bioactive glass compounds: (a) neat PCL, (b) PCL/SBA3 90/10, (c) PCL/SBA3_Cu 90/10, at 1000× magnification (filler aggregates indicated in red).
14. Scanning electron microscopy images of PCL/ATZ composites materials: (a) PCL/ATZ 90/10, (b) PCL/ATZ 80/20 and (c) PCL/ATZ 60/40.
15. SEM of PCL compounds surfaces: (a) 3D-printed PCL/ATZ 90/10 *SC*, (b) PCL/ATZ 80/20 *SC*, (c) PCL/ATZ 60/40 *SC*, (d) PCL/ATZ 90/10 *M*, (e) PCL/ATZ 80/20 *M* and (f) PCL/ATZ 60/40 *M* (relevant filler agglomeration is indicate with the red circle).
16. Cross-sections SEM images of (a) PCL/ATZ 90/10 *SC* and (b) PCL/ATZ 90/10 *M* (voids are indicate by white arrows and ATZ agglomeration are indicate by blue circle).
17. Contact angle of sample surfaces with bioactive glass in hydrophilic (a) and lipophilic (b) environments.
18. Surface contact angle of PCL/ATZ composites materials. (a) hydrophilic environment and (b) lipophilic environment.

19. BSA protein adsorbed on PCL/SBA3 samples surfaces.

20. BSA protein adsorbed on PCL/ATZ samples surfaces.

21. Hardness values HV (a) and EiT (b) of PCL/SBA3 samples.

22. Figure representing data from adhesion assay. (a) ASCs and (b) HMEC-1 cell number on specimens after 20 min of incubation.

23. Immunofluorescence images (blue represent the nuclei and green indicates cytoskeleton): (a) ASCs on neat PCL, (b) ASCs on PCL/SBA3 90/10, (c) ASCs on PCL/SBA3_Cu 90/10, (d) HMEC-1 on neat PCL, (e) HMEC-1 on PCL/SBA3 90/10, and (f) HMEC-1 on PCL/SBA3_Cu 90/10 after 24 h. Boxplot (blue for ASCs and orange for HMEC-1) representing (g) cell Area, (h) perimeter, (i) aspect ratio and (j) circularity.

24. Graph representing PF (a) and SG (b) cell adhesion evaluated after 20 min of incubation ((*) for $p < 0.05$ and (**) for $p < 0.01$). Polar histogram plot of BFE angles measured on PF cell for all samples (blue the polar bins of the distributions, red line is the mean angle value).

25. Immunofluorescence images (blue represent the nuclei and green indicates cytoskeleton): (a) PF on neat PCL, (b) PF on PCL/ATZ 90/10, (c) PF on PCL/ATZ 80/20, (d) PF on PCL/ATZ 60/40, (e) SG on neat PCL, (f) SG on PCL/ATZ 90/10, (g) SG on PCL/ATZ 80/20 and (h) PCL/ATZ 60/40 after 24 h incubation.

26. Cell viability values at 1, 3, and 7 days measured on each sample, (a) ASCs and (b) HMEC-1.

27. Cell viability of PF (a) and SG (b) after 1, 3, and 7 days ((*) for $p < 0.05$ and (**) for $p < 0.01$).

28. RLU values of ASCs after 3, 7 and 14 days ((*) for $p < 0.05$ and (**) for $p < 0.01$).

List of Tables

1. Summary table of the main natural and synthetic polymers.
2. Additive manufacturing techniques for scaffold printing.
3. Table representing percentages of filler in different composite materials.
4. Parameters for 3D printing.
5. Standard parameters of water and di-iodomethane.
6. Table representing chemical surface composition through EDX analysis.
7. Profile Roughness (R) and areal texture (S) parameters of PCL/SBA3 samples.
8. R profile roughness measured with the stylus profilometer.
9. S areal texture parameters measured with the optical profilometer.
10. S areal texture parameters of composites materials made on *M* and *SC*.
11. All surface energy components calculated on PCL/SBA3 compounds through OWRK method.
12. All surface energy components calculated on PCL/ATZ compounds through OWRK method.
13. Culture medium ions concentrations after different incubation times.
14. GPC results obtained from PCL/ATZ *M* and *SC* composites.
15. Tensile test parameters of PCL/SBA3 samples.
16. Tensile tests and hardness parameters of PCL/ATZ pomposities from solid mixing (*M*) and solvent casting (*SC*).

1. Introduction

1.1. Regenerative medicine: context and state of the art

Trauma, tumours, infections, and degenerative illnesses all cause bone tissue loss, which is a serious therapeutic burden on a global scale. It is anticipated that millions of people undergo bone restoration treatments each year, which have a significant influence not only on patients' quality of life but also on healthcare systems due to the large expenses involved [1]. Traditional reconstructive procedures, such as autografts and allografts, are still considered the clinical gold standard [2].

In particular, bone grafting strategies are classified according to the origin of graft material (Figure 1) and are characterised by specific limitations and advantages:

- **Autografts** [3,4] consist in harvesting material directly from the patient, generally from iliac crest, and subsequently transplanted to the defect site. It is considered a gold standard because of their absence of immune rejection, biocompatibility, and excellent intrinsic osteogenic, osteoconductive and osteoinductive properties. The limitations arising from this procedure includes local hematoma, the restricted amount of tissue available by donor and donor site morbidity.
- **Allografts** [2] is similar to the autograft procedure, nonetheless the donor is not the same patient but another human donor. In this way the issues of tissue availability and second surgical site are overcome. Anyway, there are still present issues linked to immune response, potential vascularization problems and risk of disease transmission despite strict controls and rigorous checks.
- **Xenografts** are grafts derived from others species, generally bovine or porcine sources. This procedure is characterised by highly tissue availability and mainly have the function of osteoconductive scaffold for the formation of new bone.

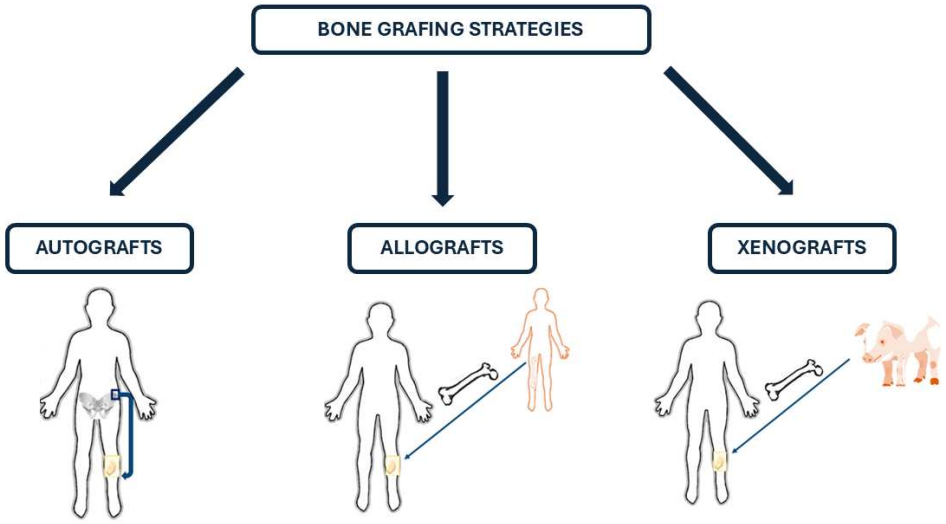

Figure 1. Scheme representing bone graft classification.

However, despite their widespread use, they are hampered by significant constraints such as the scarcity of acceptable donor tissue, the risk of post-operative complications, and the lengthy recovery times frequently required for full rehabilitation.

In this sense, bone regeneration remains one of the most serious and unsolved issues in regenerative medicine. Patients with oncological and degenerative bone loss, as well as those with severe traumatic injuries, require more effective treatment options. Conventional procedures give partial solutions, but they fall short of meeting the therapeutic criteria for safe, dependable, and patient-specific therapies. As a result, tissue engineering (TE) has developed as a novel and promising field of study, trying to overcome the limits of current treatments.

Researchers are merging developments in biomaterials, cell biology, and biomedical engineering to create novel scaffolds and devices that can promote bone regeneration in a more predictable, personalised, and effective manner. Such techniques have the potential to considerably enhance clinical outcomes while also lowering the load on healthcare systems by reducing complications and decreasing recovery times. Finally, incorporating tissue engineering into clinical practice may constitute a crucial step forward in the treatment of bone abnormalities, opening the door for a new generation of regenerative medicines.

1.2. Scaffolds

Regenerative medicine, through tissue engineering is focused on exploring potential new treatments to recover a large part of biological tissue.

Usually, tissue engineering approaches are generally divided into three strategies [5]:

- Introducing separate cells or cell replacements into the body
- Delivery of compounds that stimulate tissue proliferation, such as growth factors
- Use of various matrices or substrates seeded with cells

Generally, third option represents implantable scaffolds produced with synthetic or natural materials seeded with selected cells (Figure 2).

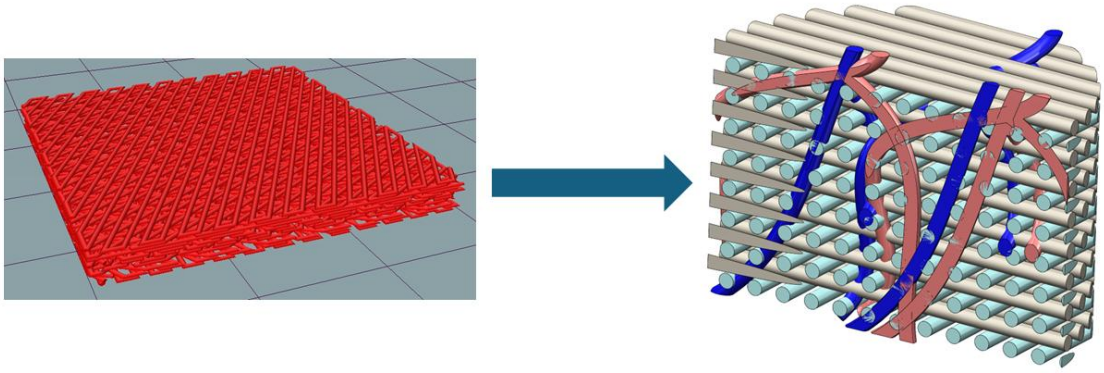

Figure 2. Example of a 3D scaffold before (left) and after (right) seeding the cells.

A scaffold is a three-dimensional structure designed to provide temporary support for cell attachment and migration, enabling tissue regeneration. This doctoral project focuses on engineering, developing, and testing innovative composite materials for scaffolds intended for bone TE.

The performance of a scaffold largely depends on the composition of the material, as it directly influences biocompatibility, mechanical strength, and degradation behaviour.

To develop a scaffold that is as customizable as possible and adaptable to as many conditions as possible, it is necessary to be able to modulate its mechanical properties, degradation rate, chemical composition, overall size and porosity. To achieve this, the most reproducible method is undoubtedly the use of polymeric scaffolds.

The most adaptable and often used alternative for scaffold production among the many groups of biomaterials are polymers and their composites. They are especially well suited for a variety of TE applications due to their excellent processability, variable mechanical strength, and changeable degradation kinetics. Moreover, polymers may be designed to have linked pore networks and high porosity, which facilitate waste disposal, nutrient delivery, cell adhesion and migration. The degree of porosity can induce a specific cellular response. Greater porosity induces cell migration, while lower porosity enhances vascularization of the implant, which is essential for the viability of the scaffold. Porosity not only influences biological response but also, if too high, it affects the mechanical properties of the scaffold.

Their chemical adaptability is crucial because it enables the creation of scaffolds that closely resemble extracellular matrix (ECM) enhancing cellular responses in both in vitro and in vivo settings. Each type of polymer naturally generated, synthetic biodegradable, or synthetic non-biodegradable offers distinct benefits in terms of long-term stability, biocompatibility, and bioresorbability, depending on the application [6].

The main objectives of a scaffold are multiple. A scaffold used for TE must enable and induce interaction between the biomaterial surface and cells. It must therefore promote cell adhesion and provide a support for the subsequent production and deposition of ECM. It is structured and designed to provide a sufficient flow of gases, nutrients and factors to support the growth and differentiation of the attached cells. The biomaterial used to produce a scaffold (both natural or synthetic) must be biodegradable and have a degradation rate that can be controlled and adjusted to the regeneration rate of the tissue it must support. One of the most important characteristics of a scaffold required for in vivo use is that it must not cause harm or alter the organism and its homeostasis in any way. The scaffold must not be immunogenic or cause toxicity [7].

Mechanical properties of the scaffold can vary significantly depending on the construct's intended use. For example, if the scaffold is used for the regeneration of soft tissues, it must be able to withstand moderate forces. Conversely, if the construct is used for hard tissues, such as bone tissue, the scaffold must be able to withstand greater forces and therefore must demonstrate superior mechanical properties. The mechanical properties (in terms of hardness, and Young modulus) must be comparable to those of the target biological tissue to ensure that the cells in the construct receive tensile or compressive signals congruent with differentiation into the desired phenotype.

The degradation rate must be proportional to the average growth rate of the newly formed tissue, as the new biological tissue must gradually replace the biomaterial forming the scaffold. The kinetics of this lytic reaction depend on the type of material and the biological context in which it is found. Some materials, such as PLA and other polyesters, are hydrolysable, while other materials, such as proteins inserted into the scaffold matrix or used as surface coatings, are enzymatically degraded. A determining factor, in addition to the composition of the material, is also the 3D structure of the scaffold as the exposed surface area is directly proportional to the degradation rate. The surface area/volume ratio plays a crucial role when designing a scaffold because it is closely related to the structure's degree of porosity. To accommodate the greatest number of cells, an implantable scaffold must have very high porosity, around 80%, and a good degree of internal interconnection [8]. This characteristic is also important for the proper flow of nutrients and the outflow of waste products.

The chemical composition of the scaffold significantly influences its performance, both biologically and mechanically. The scaffold must be chemically biocompatible, meaning it must allow cell adhesion and proliferation without being toxic or causing inflammatory reactions. In the case of polymers, the number of

monomers and the molecular weight greatly influence the scaffold mechanical properties and, in some cases, also the state of the material itself (liquid or solid).

1.3. Biomaterials

Materials used in biomedical field must possess certain characteristics that allow them to be used within the human body for therapeutic treatments or diagnostic procedures and avoid unwanted side effects.

Biology, chemistry, engineering, and medicine are highly interconnected fields in the study of biomaterials. Being a multidisciplinary field, knowledge from each of these fields is needed to study and optimize properties such as biocompatibility, mechanical strength, surface properties, and degradation rate. These materials are highly versatile, as depending on the application, biomaterials can serve as drug carriers, permanent implants, or, as in the case of this thesis, as scaffolds for tissue regeneration.

Historically, biomaterials can be divided in categories:

- **First generation**. Biologically inert or minimally reactive materials were employed to limit corrosion and the release of ions and particles after implantation, thereby reducing immune responses and foreign body reactions. This was because the initial requirements for the use of synthetic materials in biomedical applications were that they have appropriate physical properties to match those of the replaced tissue with a minimal toxic response of the host. When choosing materials for implant manufacturing, mechanical characteristics and toxicity are also important factors. A foreign fibrous capsule would form around inert biomaterials when they were inserted into the body, isolating them from the local tissue.
- **Second generation**. Combining resorbable biomaterials, which have the capacity to degrade as new tissue grows and heals, and bioactive materials, which can interact with the biological environment to enhance the biological response and the tissue/surface bonding.
- **Third generation**. Developed transient three-dimensional porous structures made of bioactive and bioresorbable materials, that can activate genes promoting live tissue regeneration. These biomaterials integrate the principles of bioactivity and biodegradability, making the combination of these two properties the most distinctive feature of third-generation biomaterials.

Generally, biomaterials can be divided into natural and synthetic origin [9]. Regarding TE, the most used materials are synthetic polymers and natural polymers. Each of them has specific characteristics and properties. To fill specific

defects, the idea is to mix them together in specific proportions to obtain specific characteristics, creating new composite biomaterials.

1.3.1. Natural biomaterials

Natural biomaterials have attracted great interest in the field of regenerative medicine thanks to their strong characteristics of biocompatibility, biodegradability, high adsorbability on substrates and ease of use [10,11]. For environmental reasons, natural biomaterials or those derived from biomasses may be favoured over synthetic ones.

Bacterial cellulose

Bacterial cellulose (BC) is a natural polymer produced by various types of bacteria, such as *Acetobacter, Stobacter, Rhizobium, Agrobacterium,* etc. These organisms are able to synthesize cellulose from glucose, lactose, fructose and other saccharides as carbon sources forming a 3D structure with β-1,4 glucan cellulose bonds [12,13]. Brown was the first to produce bacterial cellulose in 1886. As a biomaterial, BC has relevant characteristics that enhance its appeal as a desirable choice for TE. Mechanical properties such as tensile strength and flexibility are impressive. It has good chemical-physical and biological properties such as high water absorption and retention capacity, blood compatibility, permeability to liquids and gases, superior biocompatibility in the biological environment, and non-cytotoxicity [14]. Despite BC has no antibacterial properties, it has a hight surface area and porosity that can be adopted for drug release functions (biological factors, antibiotics, etc) [15].

Collagen

Collagen represent a great natural biomaterial thanks to its great biological properties such as biodegradability and degradability by enzymes, non-toxicity, biocompatibility and low immunogenicity. It can be used in various fields, such as tissue engineering, and in particular for bone tissue engineering [16].

A lot of tissue in human bodies such as cartilage, tendons, ligaments, skin and bones are constituted by collagen. This fibrous protein is a structural component in most of ECM tissue types.

In human body, 29 different types of collagens have been identified, but the most common is the collagen type I that constitutes almost 80% of total collagen. Different types of collagens have different compositions and stimulate various activation pathways. Regarding wound healing process, collagen guide cell proliferation and affect cell differentiation. It has been demonstrated that collagen, particularly collagen type I, may effectively act as either a stimulator or an inhibitor during the angiogenesis process [17]. This is due to collagen type I C-peptide fragments, that induce the endothelial cells to start the angiogenesis process and consequently the tissue regeneration. Others collagen types, for example proteolytic

fragments of collagen XVIII and IV, are fragments present on basement membranes and block the proliferation of endothelial cells. Thomasstatin, arrestin and endostatin function as endothelial cell apoptosis inducers, inhibitors of endothelial cell migration and proliferation as reported by Kareva et al. [18].

Decellularized ECM

Decellularized extracellular matrix (dECM) is obtained by using different methods removing cellular component from ECM [19] and its often used in TE. Its composition and organisation depend on what type of tissue it belongs. dECM due to its nature possess strong characteristics of biocompatibility, biodegradability and is quite similar to the natural ECM. On the other hand, its use is subject to challenges such as immunogenicity and sterilization. Some tissues from which dECM can be obtained are dermis, pancreas, kidney, oesophagus and bone [20–24].

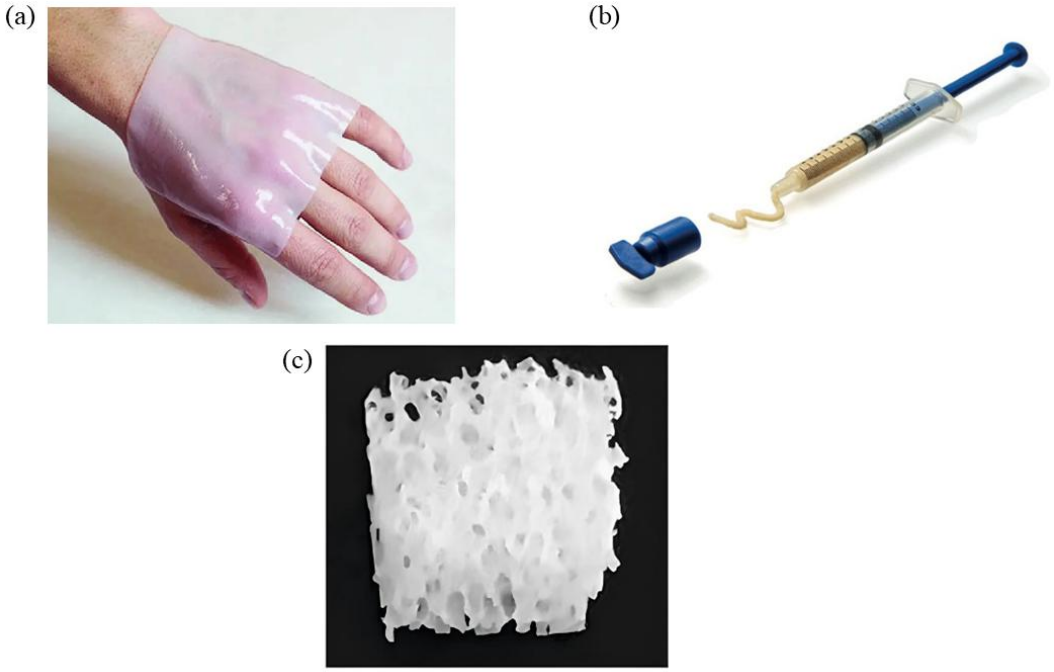

Figure 3. Image representing principal natural biomaterials: (a) bacterial cellulose [25], (b) collagen and (c) decellularized extracellular matrix [26].

1.3.2. Synthetic biomaterials

Synthetic polymers are that group of polymers that do not derive directly from a biological source but from a chemical synthesis pathway. Due to their synthetic nature, these biomaterials possess standardized and reproducible properties very useful in terms of design biomedical devices.

Synthetic polymers structural dissimilarity from the ECM poses a challenge to their bioactivity, since they often do not promote cell adhesion, proliferation, and differentiation.

On the contrary, physical chemical, mechanical and degradability properties of these biomaterials are modular and customizable depending on clinical application. These materials are easier to handle and less delicate than natural biomaterials. Synthetic biomaterials are often modified to change their properties by immobilizing or absorbing biological molecules such as protein, polysaccharides or peptide sequences enhancing the general bioactivity. This technique is called functionalization and can be used to alter the surface properties of the material as in the case of a covalent bond (salinization [27,28], plasma treatment [29], peptide sequences with adhesive properties [30], etc) or through non-covalent interactions as in the case of the layer-by-layer technique [31,32]. It is also possible to modify properties of synthetic biomaterials by incorporating fillers able to donate new properties or enhance native characteristics. In bone grafting, most used filler for tissue engineering are inorganic materials such as ceramics and bioactive glasses [6] to try to imitate the ECM of bone tissue as closely as possible.

Below is a brief overview of some of the main synthetic biomaterials used in TE.

Polyglycolic acid

Polyglycolic acid (PGA) is used in wound healing because of its high mechanical properties, gases impermeability, biodegradability and biocompatibility. PGA is a synthetic thermoplastic polymer, with a chemical formula $(C_2H_2O_2)_n$, obtained from glycolic acid by the ring-opening polymerization [33]. Researchers demonstrate that PGA possess encouraging characteristics that promote its use for wound dressing. Zha et al. [34] proven that PGA has effective in promoting inflammation control and epithelial tissue formation. Zha and his equipe developed SF/PGA-based biodegradable nanofibrous scaffolds loaded with Deferoxamine (DFO) for diabetic wound healing. These scaffolds demonstrated biocompatibility, biodegradability, and the ability to support cell growth, proliferation, and migration. Moreover, they improved mechanical strength by 70% and enhanced angiogenesis, collagen deposition, and wound healing within 14 days.

PGA has also been successfully applied to cover wounds from endoscopic and open surgeries [35]. Studies have shown that, in mice, fibrin/PGA glue can prevent gas infiltration and wound fluid secretion, ensuring complete wound closure [36].

Polyethylene glycol

Polyethylene glycol (PEG) is a biocompatible polymer obtained by synthesis. Its chemical formula is $H(OCH_2CH_2)_nOH$ and *n* correspond to the number of ethylene oxide units presents. A peculiarity of this hydrophilic biomaterial is that depending of its molecular weight PEG can have a liquid form (under 1000 Da), a waxy aspect (between 1000 and 2000 Da) or can be a crystalline solid (over 2000 Da) [37].

Thanks to its nontoxicity, low immunogenicity and general biocompatibility, PEG was selected as recommended material for drug delivery by the Food and Drug Administration (FDA). Trought “pegylation” [38], a technique that allow to attach,

through covalent or noncovalent bond, a polyethylene glycol chain with bioactive molecules such as proteins or peptides for drug delivery purposes. This technique increases the drug size because of the presence of PEG, and this prevents the kidneys from filtering the compound quickly, thereby increasing the half-life and retention time of the drug.

PEG is also used for the creation of scaffolds [39] in tissue engineering thanks to its flexibility and biocompatibility, but it's also used as a copolymer in a mixture or in a composite material [40] to compensate for the non-optimal mechanical properties.

Polylactic acid

FDA has licensed polylactic acid (PLA), a hydrophobic aliphatic polyester (chemical formula $(C_3H_4O_2)_n$), for a variety of clinical and biological uses [41]. Numerous studies have demonstrated that PLA is highly suited for additive manufacturing technology due to its exceptional biocompatibility, heat stability, and PLA degradation, as well as its low viscosity and thermoplastic qualities [42]. Interesting characteristic of PLA is that depending on the molecular weight and the distribution of stereoisomers type (D or L) in the polymeric structures, PLA undergoes significant changings in terms of degradability and physicochemical properties such as melting temperature, glass transition temperature and crystallinity degree.

During PLA degradation, the polymer undergoes ester hydrolysis reaction. This reaction releases lactic acid molecules into the environment. The lactic acid is then metabolized by the enzyme lactate dehydrogenase (LDH), converting it into pyruvate. The pyruvate transported into the mitochondria will be converted into acetyl-CoA, a molecule that is essential for the Krebs cycle.

Table 1. Summary table of the main natural and synthetic polymers.

Category	Name	Abbreviation	Characteristic	Applications
Natural biomaterials	Bacterial cellulose	BC	Produced by bacteria, excellent mechanical strength	Drug delivery, artificial blood vessels
	Collagen	/	Excellent biocompatibility and cell adhesion	Bone and cartilage scaffolds
	Decellularized Extracellular Matrix	dECM	Derived from tissues after cell removal	Tissues reconstruction
Synthetic biomaterials	Polyglycolic Acid	PGA	Aliphatic polyester. High crystallinity, high mechanical strength	Bone fixation, fast-degrading scaffolds
	Polyethylene Glycol	PEG	Polyether, highly biocompatible	Drug delivery, scaffolds, copolymer
	Polylactic Acid	PLA	Aliphatic polyester derived from renewable resources	Scaffolds, medical devices

1.4. Polycaprolactone

Unlike other biomaterials, polycaprolactone (PCL) is a linear, semicrystalline synthetic polyester that is inexpensive, highly processable, and easily mouldable into a wide range of geometries, which makes it an excellent candidate for scaffold manufacturing in tissue engineering. Its thermal stability, low melting temperature (~60 °C), and FDA approval for certain biomedical and drug-delivery applications have further contributed to its widespread adoption in both hard and soft tissue regeneration [43]. Importantly, PCL exhibits a very slow degradation rate (ranging from months to several years), but its characteristics such as hydrophobicity, crystallinity, and degradation kinetics can be significantly altered through copolymerisation, blending, or surface modification [44,45].

Thanks to its mechanical tunability and processability, PCL has been used to support the repair of defects in bone, cartilage, osteochondral tissue, skin, peripheral nerves, musculoskeletal tissues, cardiovascular structures, and hepatic tissue, demonstrating strong versatility across regenerative applications [46–48]. To overcome the limitations associated with using a single polymer especially its inherent hydrophobicity and limited cell-binding capacity PCL is often blended with natural polymers (e.g., collagen, gelatin, chitosan, alginate, silk fibroin) or synthetic polymers (e.g., PEG, PLA, PLGA), and is also frequently combined with bioceramics such as hydroxyapatite (HA), β-tricalcium phosphate (β-TCP), and bioactive glass to enhance osteoconductivity and biological performance [49–52].

These composite or hybrid biomaterials can be processed using a wide range of scaffold fabrication techniques, including electrospinning, solvent casting/salt-leaching, phase separation, gas foaming, spin coating, rapid prototyping, and fused deposition modelling (FDM). Each technique allows tailoring of scaffold porosity, fibre alignment, and microscale architecture depending on the target tissue [53–55].

Because native PCL is highly hydrophobic, extensive research has focused on surface modification strategies to enhance its cell-attracting properties. Approaches include plasma treatment, alkaline hydrolysis, immobilisation of hydrophilic polymers, and incorporation of bioactive peptides such as RGD, growth factors or natural components like fibrin or collagen [56,57] [Her. These biochemical functionalisation strategies have been shown to significantly improve biocompatibility, promoting enhanced cell adhesion, proliferation, and lineage-specific differentiation, thereby broadening the use of PCL scaffolds in tissue engineering.

1.4.1. PCL synthesis

PCL is composed by a repetition of hexanoate units forming its aliphatic polyester structure. PCL is synthesizable through two strategies (Figure 4), the ring opening polymerization of the e-CL and the condensation of 6-hydroxycaproic (6-hydroxyhexanoic) acid [58]. By employing either vacuum-assisted water removal or biologically derived lipase enzymes to change the equilibrium in favour of polymer formation, the synthesis method creates aliphatic polyesters from hydroxycarboxylic acids. Ring-opening polymerisation (ROP), on the other hand, is typically chosen because it produces polymers with a higher molecular weight, which leads to an improved mechanical behaviour, melting temperature, glass transition temperature, viscosity and a reduced degradation rate. Anionic, cationic, monomer-activated, and coordination-insertion pathways are the four primary ways that ROP can proceed. The molecular weight and distribution, the chemical makeup of the end groups, and the architecture of the final copolymer are some of the variables that affect these techniques. Metal-based, organic, and enzymatic catalysts are among the catalytic systems that support ROP; stannous(II) 2-ethylhexanoate is a commonly used example for its high efficiency and comparatively low toxicity.

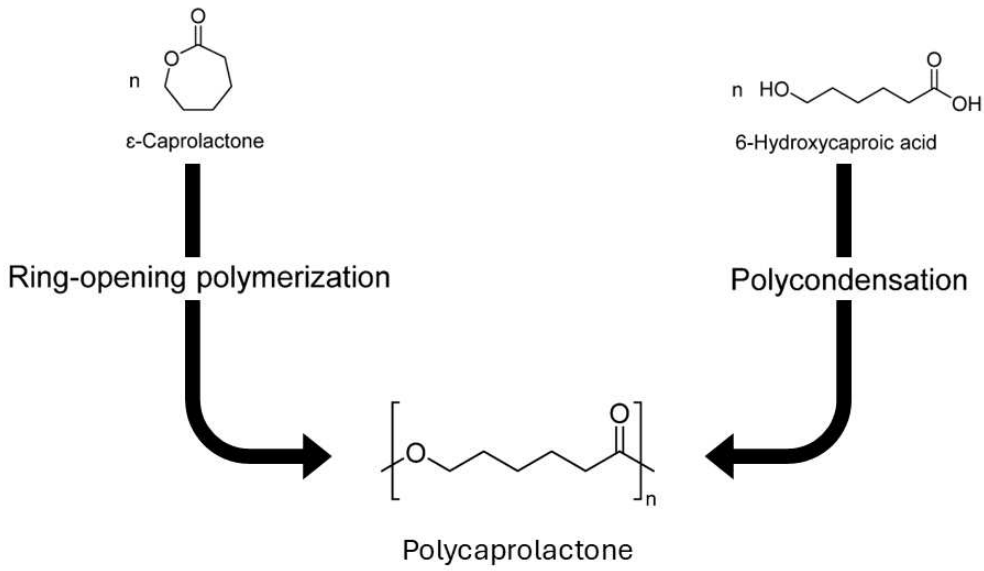

Figure 4. Scheme representing two principal methods of Polycaprolactone synthesis.

1.4.2. Physicochemical PCL properties

Poly(ε-caprolactone) (PCL) exhibits a semicrystalline structure characterized by a very low glass transition temperature (Tg ≈ −60 °C) and a melting temperature (Tm) typically ranging between 59 and 64 °C, depending on molecular weight and crystallinity. These thermal properties result in high chain mobility at room and physiological temperatures, conferring the polymer significant flexibility and toughness. The mechanical robustness of PCL is strongly associated with its high degree of crystallinity, which can reach values of up to approximately 69%, while its molecular weight can be tailored over a wide range, typically between 5,000 Da and 40,000 Da [59,60], allowing modulation of mechanical strength, degradation behavior, and processability.

From a physicochemical perspective, PCL demonstrates excellent compatibility with inorganic fillers, such as ceramics and bioactive glasses. This feature makes it one of the most promising polymer matrices for the development of polymer-ceramic composite materials, particularly in applications where improved stiffness, bioactivity, and long-term structural stability are required [61–63]. The hydrophobic nature and chemical stability of PCL further facilitate uniform dispersion of inorganic phases, contributing to enhanced interfacial interactions and overall composite performance.

Regarding solubility, PCL is insoluble in water over short time periods, in contrast to its high solubility in a wide range of organic solvents, including chloroform, carbon tetrachloride, petroleum ether, benzene, diethyl ether, toluene, dichloromethane, and cyclohexanone [64]. While PCL does not dissolve in aqueous environments as it does in these organic solvents, long-term exposure to water leads

to hydrolytic cleavage of its ester bonds. This slow hydrolysis process, which is influenced by factors such as crystallinity, molecular weight, and environmental conditions, underlies the gradual degradation of PCL rather than true dissolution. This combination of short-term water insolubility and long-term hydrolytic degradability is a key physicochemical characteristic that supports the use of PCL in applications requiring prolonged structural integrity followed by controlled resorption.

1.4.3. Mechanical properties of PCL

Mechanical properties represent a critical design parameter in the development of composite materials and tissue-engineering scaffolds, as they directly influence load-bearing capability, structural stability, and biological performance. Consequently, both the fabrication method and the material composition must be carefully tailored according to the targeted application. Bulk (PCL) typically exhibits superior mechanical properties such as tensile strength and Young's modulus when compared to porous or fibrous PCL scaffolds produced via techniques like electrospinning or additive manufacturing. This reduction in mechanical performance is primarily attributed to the presence of porosity, fibre discontinuities, and reduced effective load-bearing cross-section, which are intrinsic to scaffold architectures designed to promote cell infiltration and nutrient diffusion. Neat, bulk PCL generally shows a tensile strength ranging from 25 to 43 MPa and a Young's modulus between 330 and 360 MPa [65], values that decrease significantly once porosity and microstructural complexity are introduced.

To overcome these limitations and tailor mechanical behaviour to match that of native tissues, PCL is frequently combined with fillers such as ceramics, bioactive glasses, or natural polymers. The introduction of fillers transforms the material into a composite system, where the reinforcing phase plays a fundamental role in load transfer and stress distribution. In particular, rigid ceramic fillers such as hydroxyapatite (HA) [66], β-tricalcium phosphate (β-TCP) [61], or bioactive glass [67] can significantly increase stiffness and compressive strength, especially for bone-related applications, by acting as stress-bearing phases within the softer polymeric matrix. The extent of mechanical enhancement strongly depends on filler content, particle size, dispersion quality, interfacial adhesion, and filler morphology [49,68].

It is important to distinguish between polymer-filler composites and polymer blends, as these two strategies influence mechanical properties through different mechanisms. In composite materials, fillers are typically insoluble and mechanically distinct phases that reinforce the polymer matrix by improving stiffness, strength, and sometimes toughness through mechanical interlocking and interfacial stress transfer. In contrast, polymer blends involve the combination of two or more polymers, where the resulting mechanical properties arise from the miscibility, phase morphology, and intermolecular interactions between polymer

chains. While polymer blends are often used to tune flexibility, degradation rate, or processability, they generally do not provide the same level of mechanical reinforcement achievable with inorganic fillers unless specific compatibilization strategies are employed [43,69].

Natural polymer fillers such as collagen, gelatin, or chitosan can also influence mechanical properties, although their primary contribution is often related to improved bioactivity rather than reinforcement. These fillers may reduce stiffness while enhancing elasticity and toughness, depending on composition and phase distribution, making them particularly suitable for soft tissue engineering. However, poor interfacial bonding or filler agglomeration can negatively affect mechanical performance, leading to stress concentration and premature failure. Therefore, achieving an optimal balance between reinforcement and ductility remains a key challenge in composite scaffold design.

Overall, the strategic incorporation of fillers into PCL based systems represents a powerful approach to overcome the intrinsic mechanical limitations of porous scaffolds. Understanding how filler type, concentration, and interfacial interactions affect mechanical behaviour is essential, as this aspect, together with its biological properties, represent constitutes the core focus of composite material design in tissue engineering.

1.4.4. Surface PCL properties

The surface characteristics of a fabricated scaffold are a crucial factor, as they are directly influenced by the intended biomedical use. Attributes like pore size, overall porosity, and surface roughness become very important because scaffolds are made to mimic the extracellular matrix environment that helps cells attach and grow. A scaffold with a porous, interconnected structure helps cells grow and organise themselves in space. Also, porosity has a big effect on how nutrients move, how cells move, and how strong the structure is mechanically. Generally, surface roughness values between 5 and 50 μm are acceptable, and pore diameters should be more than 20 μm [58]. For scaffolds made of PCL nanofibers or mesh structures, the water contact angle is also very important because it accounts for porosity, surface texture and surface hydrophobicity / hydrophilicity. In general, surface properties are dependent to layer thickness and other fabrications parameters, so in literature different production technologies are employed depending on the intended use. Blending fillers also is a variable to modify surface properties of the final material.

1.4.5. PCL degradation properties

The degradation rate is an important factor in the contest of biomaterials behaviour. PCL degrades slowly compared to others biopolymers [70] because of the presence of five CH_2-moieties repeated units and its surface hydrophobicity.

The main degradation mechanism of PCL is the hydrolytic cleavage of its ester groups that can be carried out enzymatically and non-enzymatically.

Enzymatic degradation, in a physiological environment, is a non-specific reaction and is carried out by lytic enzymes that cleave the ester bonds present on the material's surface. These enzymes include lipases, nonspecific esterases present in lysosomes and various tissues, cholinesterase present in the plasma, and lysosomal hydrolases [59].

Non-enzymatic hydrolysis [71] is induced by water present in the tissue environment. There are two main conditions in which chemical hydrolysis occurs. In an acidic environment, protonation of the ester carbonyl occurs, making it more susceptible to nucleophilic attack by water. Alternatively, hydrolysis can occur in a basic environment in which the hydroxide ion (OH^-) attacks the carbonyl of the polymer chain. In a physiological environment, chemical hydrolysis of PCL is very slow due to the stable body temperature and the slightly basic physiological pH (7.4).

In both cases the reaction product is *6-hydroxyhexanoic acid* [72]. This molecule can be metabolized by cells, first undergoing oxidation which converts it into *6-hydroxyhexanoyl-CoA* and subsequently, through the β-oxidation metabolic pathway, it is split into *acetyl-CoA*. Acetyl-CoA is a fundamental molecule for the Krebs cycle, which is involved in energy metabolic pathways as shown in figure 5.

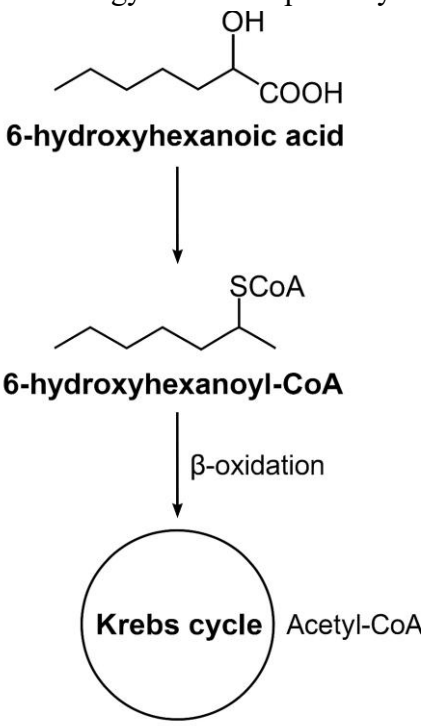

Figure 5. Oxidation process of 6-hydroxyhexanoic acid to obtain Acetyl-CoA and enter the Krebs cycle metabolic pathway.

1.5. PCL as a polymer matrix in composite materials

Among the many qualities that PCL possesses as a material for the manufacture of scaffolds, it is worth mentioning that it is soluble in certain solvents and that, following evaporation of the solvent (solvent casting), the polymer returns to its original state, allowing to be mixed with various fillers. This characteristic is fundamental for the design of composites materials. In literature [61,63,67], several studies show that the addition of a filler results in changes to fundamental properties of the polymer, such as its physicochemical, mechanical, and surface properties.

In general, new biomaterials combine biological behaviour and mechanical properties of synthetic polymers with features provided by incorporated fillers.

Among all filers available for PCL blending, the most common are synthetic, natural and ceramic materials. While natural and synthetic biomaterials have already been discussed above, ceramic materials are an excellent addition due to their mechanical characteristics, and biocompatibility features.

Beta tricalcium phosphate (β-TCP) is an excellent filler for biomaterials, particularly for bone [61]. It has excellent osteoconductive properties because its chemical composition is very similar to bone mineralized ECM, indeed it is recognized by osteoblasts as a substrate for adhesion and proliferation.

Alumina-Toughened Zirconia (ATZ) is a filler used for its excellent mechanical properties and good biocompatibility. Compared to β-TCP, it does not exhibit osteoconductive properties, but it has high mechanical strength, thus it is ideal for applications that require high loads, such as those to which bone tissue is subjected.

Bioactive glasses are very effective fillers for composite biomaterials in regenerative medicine because they are able to interact with the biological environment through regulated ionic release and surface responses. These strategies actively stimulate cell adhesion, proliferation, and differentiation, as well as osteointegration and angiogenesis, which improve the composite scaffold's overall biological performance. Being mainly composed of silicates, phosphates, and calcium and sodium oxides, when the material is placed in an aqueous environment, a series of chemical reactions occur that stimulate the environment in an osteogenic sense. They release ions such as calcium (Ca^{+}) and sodium (Na^{+}), which in turn lead to the formation of a layer of silica gel on the surface. This gel is the optimal substrate for the precipitation of calcium phosphate and the consequent formation of hydroxyapatite (one of the main components of bone ECM).

1.6. Solvent casting technique

The solvent casting technique is widely regarded as a laboratory gold standard for the fabrication of polymer blends and polymer/filler composite materials, owing to its simplicity, versatility, and high level of control over material composition. This method has been extensively applied to a broad range of biodegradable and bioresorbable polymers, including PCL, PLA, PGA, poly(lactic-co-glycolic acid)

(PLGA), and natural polymers such as chitosan and gelatin, which are all readily soluble or dispersible in organic solvents suitable for biomedical processing [73–76]. In solvent casting, the polymer matrix and, when applicable, a second polymer or dispersed solid fillers such as ceramics or bioactive glasses is dissolved or uniformly suspended in an appropriate solvent. The resulting solution is cast into a mould or onto a substrate, and controlled solvent evaporation leads to the formation of a solid film or scaffold with a homogeneous distribution of the constituent phases [73,74].

From a processing perspective, the choice of solvent is a critical parameter in solvent casting, as it directly affects polymer solubility, solution viscosity, evaporation rate, and final microstructure. Commonly used solvents for biodegradable polymers such as PCL, PLA, and PLGA include chloroform, dichloromethane, tetrahydrofuran, and dimethylformamide, selected based on polymer-solvent affinity and volatility. The solvent evaporation rate must be carefully controlled to ensure homogeneous phase distribution and reduce the risk of residual solvent entrapment within the final composite structure [69].

This approach offers several advantages that make it particularly suitable for polymer blends and composite systems:

- The ability to process thermo-sensitive polymers and bioactive fillers without exposure to elevated temperatures, which is especially relevant for polymers such as PCL with low melting temperatures.
- Precise control over polymer and filler ratios, enabling systematic tuning of mechanical, degradation, and biological properties.
- Enhanced initial dispersion of fillers due to mixing in the liquid phase, which is critical for achieving reproducible composite morphologies and reliable mechanical performance [74,75].

When combined with porogens such as salt particles, solvent casting enables the fabrication of three-dimensional porous scaffolds with tunable pore size and porosity by adjusting the porogen size and concentration, a strategy widely adopted for PCL, PLA, and PLGA based scaffolds in tissue engineering [73,75].

Despite these advantages, solvent casting also presents inherent limitations that must be considered in composite design, including the potential presence of residual solvents, environmental and safety concerns associated with volatile organic solvents, limited scalability, and difficulties in producing thick or highly interconnected 3D constructs without additional processing steps [76]. Consequently, while solvent casting is predominantly used for material formulation development, proof-of-concept studies, and comparative evaluation of polymer blends and composites, it remains a benchmark technique against which more advanced fabrication methods such as melt blending, extrusion-based additive manufacturing, and hybrid processes are frequently compared in polymer composite research [73,76]. In this work, solvent casting was used as the first step for the creation of the composite material.

1.7. Additive manufacturing in bone tissue engineering

Additive manufacturing (AM) technology is widely used in regenerative medicine, particularly for the possibility to build three dimensional supports like scaffolds. Indeed, the intrinsic versatility in generate complex structures, makes AM a widely used tool for both scientific research and clinical purposes. Various AM technologies are currently available, including Fused Deposition Modelling (FDM), Selective Laser Sintering (SLS), and Stereolithography (SLA) [77].

1.7.1. Fused Deposition Modelling

FDM is one of the first ways to do 3D printing. The method uses a thermoplastic polymer filament to make 3D scaffolds. As the filament melts, it is pushed through a hot nozzle onto a solid build platform (Figure 6). There, it cools, hardens, and forms the desired shape. Most common polymers used in FDM for biomedical purposes are PCL, poly(d,l-lactide-co-glycolide) (PLGA), and poly(d,l-lactide) (PDLA). Filaments with diameters of several hundred micrometres are usually used, and the quality of the scaffold that comes out is very much affected by factors like the size of the nozzle and the rate of extrusion. Those parameters can vary depending to the 3D printer. The FDM method is promising because it is cheap and easy to implement. This method, however, is only useful for polymers that have the right thermoplastic, viscoelastic, and processing properties (Table 2).

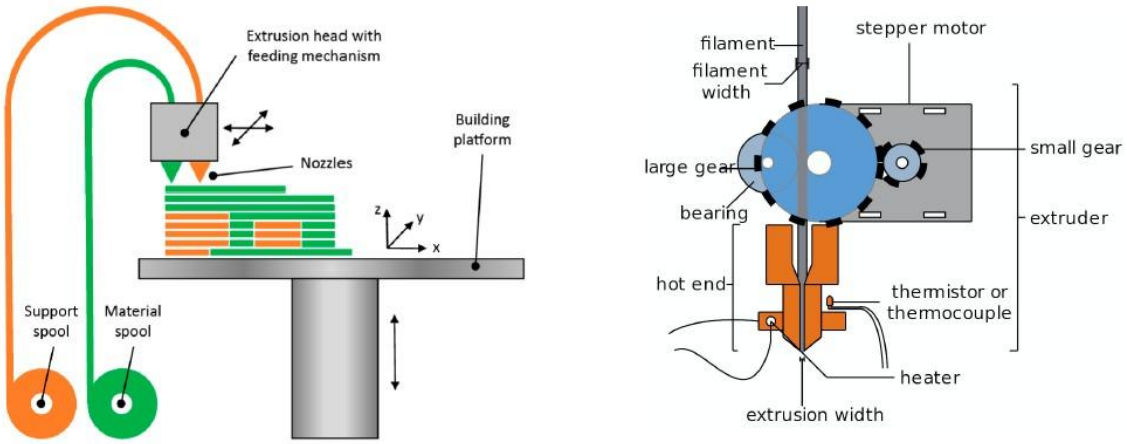

Figure 6. FDM system architecture.

1.7.2. Selective Laser Sintering

The main components of a Selective Laser Sintering system are a roller, a vertically moving piston, a powder bed, and a laser source (Figure 7). Layer by layer, powder particles are selectively fused by a high-energy laser beam in this process, and the unsintered powder acts as a natural support for the growing 3D structure. PCL [78], hydroxyapatite (HA) [66], and bioactive glass are among the powdered materials that have been used in SLS (Table 2). Laser power, particle size and processing temperature are important factors that affect the resolution, size, and mechanical integrity of scaffolds made using SLS. SLS's primary benefit is its capacity to precisely create complex geometries and provide scaffolds with exceptional mechanical strength. For example, this technique can be used to create bone repair constructs with gradient material distribution and hierarchical architectures. Even though SLS is frequently used to fabricate bone scaffolds, it still has drawbacks like high operating temperatures, high expenses, and intricate post-processing procedures (like secondary sintering to reduce scaffold porosity).

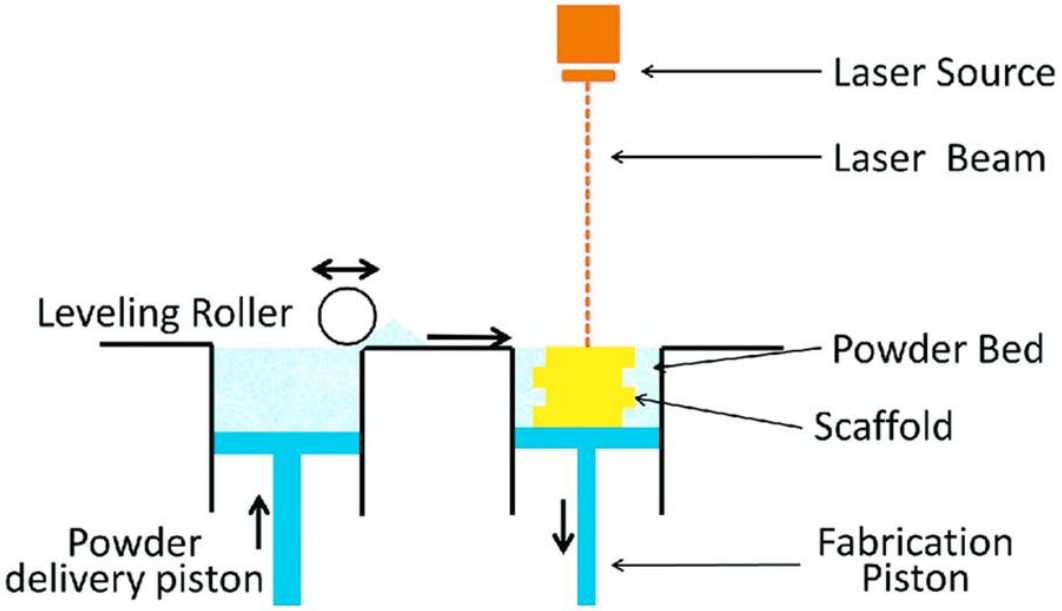

Figure 7. SLS conceptual structure.

1.7.3. Stereolithography

By employing lasers or ultraviolet light to spatially control the photopolymerization of light-sensitive polymers or precursors, SLA produces 3D-structures. According to the design pattern, a layer of photosensitive material is applied to a platform and exposed to UV light selectively (Figure 8). The structure is constructed in stages by lowering the platform to allow for the deposition and

curing of successive layers after the first layer has dried. With an average precision of about 100 µm, SLA provides the highest resolution among additive manufacturing techniques, despite the method's limitations caused by the scarcity of appropriate photosensitive precursors.

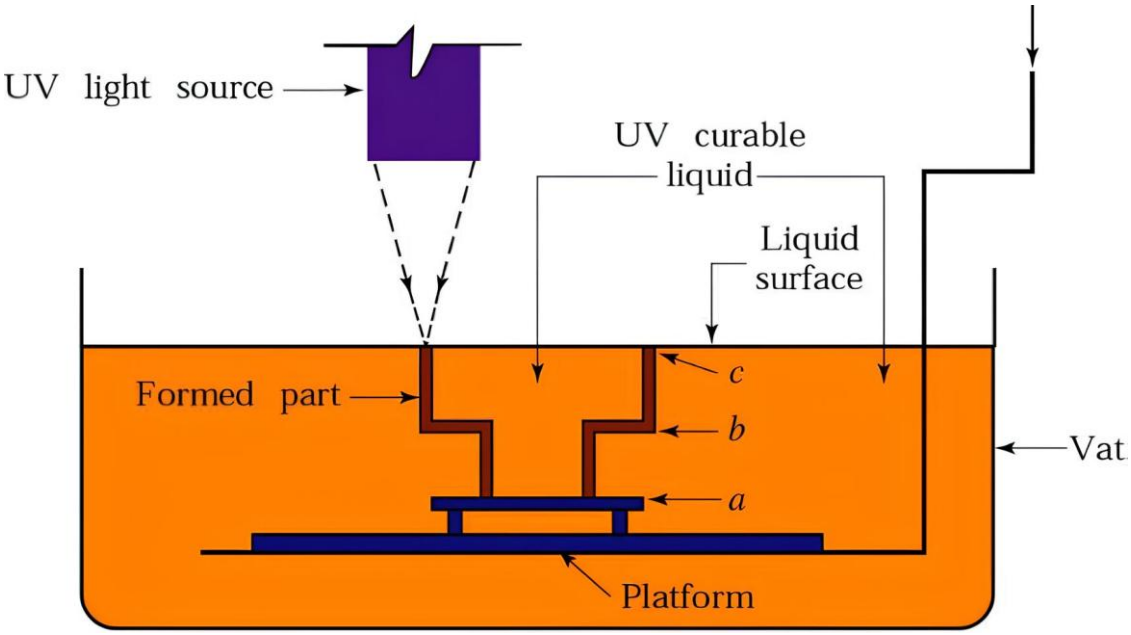

Figure 8. SLA framework.

Table 2. Additive manufacturing techniques for scaffold printing.

AM technology	FDM	SLS	SLA
Benefits	Relatively low-coast	Large size, great mechanical properties	High resolution
Restrictions	Low resolution, selected materials	Expensive, slow, non-homogeneous surface	Limited materials
Precision	50 – 200 µm	45 – 100 µm	10 – 100 µm
Available materials	Generally thermoplastic polymers	Vast	Restricted

1.8. Stem cells for tissue engineering

Stem cells are of core importance to TE because of their incredible power to self-renew and differentiate into a variety of specialized cell types. Stem cells can be employed together with biomaterial scaffolds and bioactive factors to support the replacement or repair of damaged organs and the construction of functional

tissue. The availability, immunomodulatory effect, and multilineage potential of mesenchymal stem/stromal cells have drawn widespread interest in this respect. With progress in stem cell science and additive manufacturing technologies, the development of increasingly personalized and potent regenerative therapies is being progressed, and new avenues for clinical application in biomedical engineering and medicine are opening up.

1.8.1. Mesenchymal stem/stromal cells

One kind of stromal cell that can self-renew and differentiate into several cell lineages is called mesenchymal stem/stromal cell (MSC) (Figure 9). They can be isolated from a variety of tissue, such as bone marrow [79], adipose tissue [61,63,80] and the umbilical cord. These cells are thought to be especially appropriate since they can be easily maintained in cultures and produce adequate amounts of MSCs, which makes them very useful for both possible clinical applications and experimental research.

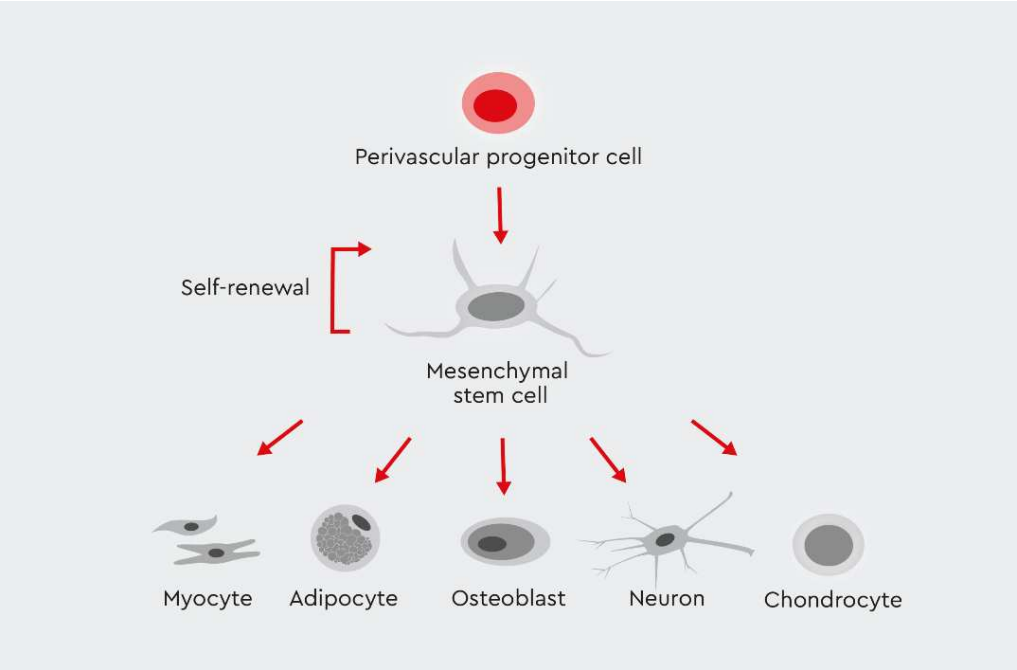

Figure 9. Mesenchymal stem/stromal cells multipotency.

1.8.1.1. Adipose-derived stem cells

Several therapeutic applications and pre-clinical studies benefit from the use of ASC because of their abundance and availability [81]. ASCs are easy to expand and possess capability to differentiate in osteogenic, neurogenic, myogenic, adipogenic and chondrogenic lineage (Figure 9) and used in various fields, such as knee arthritis [82], and bone regeneration [83] resulting safe and effective.

ASCs are an excellent model for both in vivo and in vitro experimentation. Primary adipose tissue-derived stem cells are subject to intrinsic patient variability and therefore cannot be used for standardized processes. To overcome this problem, ASC52-hTERT are an excellent alternative because they are stem cells immortalized by the continuous expression of human telomerase reverse transcriptase capable of preventing the onset of senescence.

1.8.1.2. Human Microvascular Endothelial Cells

To achieve an effective tissue regeneration, it is also important to guarantee a correct vascularization. Thus, the response of endothelial cells to different biomaterials must be studied. Endothelial cells derived from MSCs too, indeed they share the expression of some markers, such as CD146, CD90, CD73. The most common endothelial cells utilized in experimental model of regenerative medicine are HUVEC. Those cells are human umbilical vein endothelial cells and are widely used as in vitro model to study processes such as angiogenesis, cell adhesion, response to biomaterial and bone generation [84,85]. Since bone has a microvasculature, we preferred the human microvascular endothelial cells (HMEC) to perform our in vitro tests, such as tubulogenesis assay. In this regard, we recently showed that HMEC-1 formed vessel-like structure in response to stimulating factors released by periodontal ligament-derived stem cell and dental pulp-derived stem cells [86].

1.9. Project purpose

In this work, I analysed several composite materials that have been developed with different fillers and different methodologies for 3D printing applications. I investigated PCL blended both through solvent casting and by solid mixing with Alumina-Toughened Zirconia, and copper-doped bioactive glass. All composite materials have been analysed for both biocompatibility and chemical-physical characterization to investigate their potential applications in clinical practices.

2. Materials and methods

2.1. Sample Preparation

A polycaprolactone polymer with ester end groups (CAS-n 24980-41-4; CELLINK PCL TP-60505, Bico Group, Gothenburg, Sweden) was used for the creation of several composite materials loading the polymeric matrix with:

- **alumina-toughened zirconia** trough solvent casting and solid mixing. ATZ (made of 20 wt.% Al2O3 and 80 wt.% 3Y-TZP composed of 3 mol% yttria stabilized zirconia, Tosoh Bioscience, Tokyo, Japan) through solvent casting with chloroform (CHCl3, CARLO ERBA Reagents s.r.l., Cornaredo, Italy) performing agitation in solvent with the filler overnight and subsequently left to dry under a chemical hood. An impact mill that was homemade was used to perform the solid mixing technique. ATZ and PCL powders were mixed for 30 seconds at 8000 rpm (Figure 10 b). PCL/ATZ 90/10, PCL/ATZ 80/20, and PCL/ATZ 60/40 composite materials were prepared (Table 3) both for solvent casting and for solid mixed samples. To better distinguish the materials produced for the different experiments, the samples produced through solid mixing were labelled with the initials (*M*), and the samples obtained through solvent casting were labelled with the initials (*SC*) or without any initials, since solvent casting was considered the gold standard in this project.

(a)

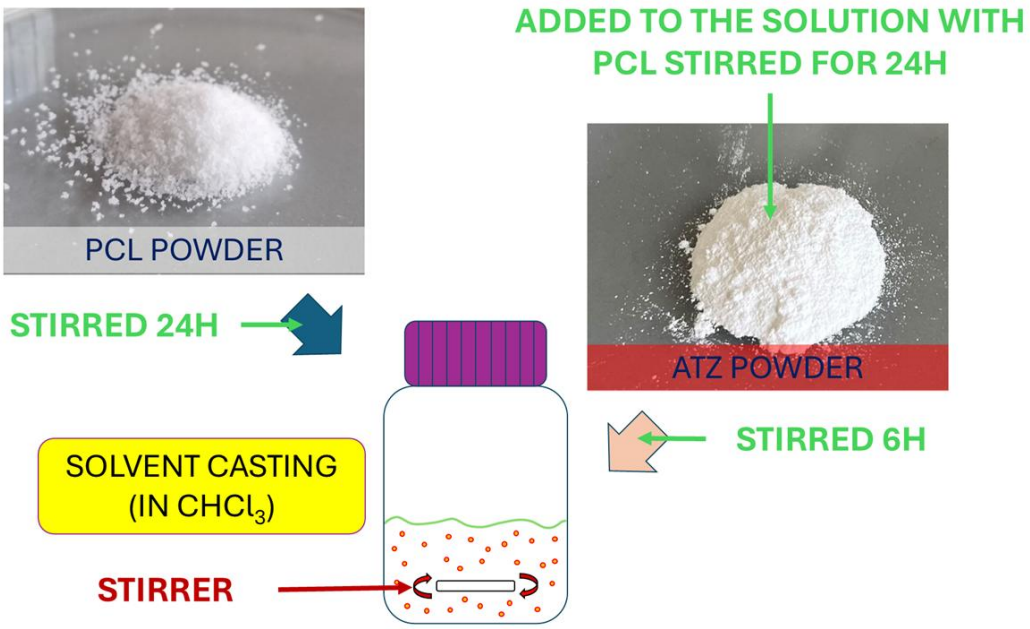

(b)

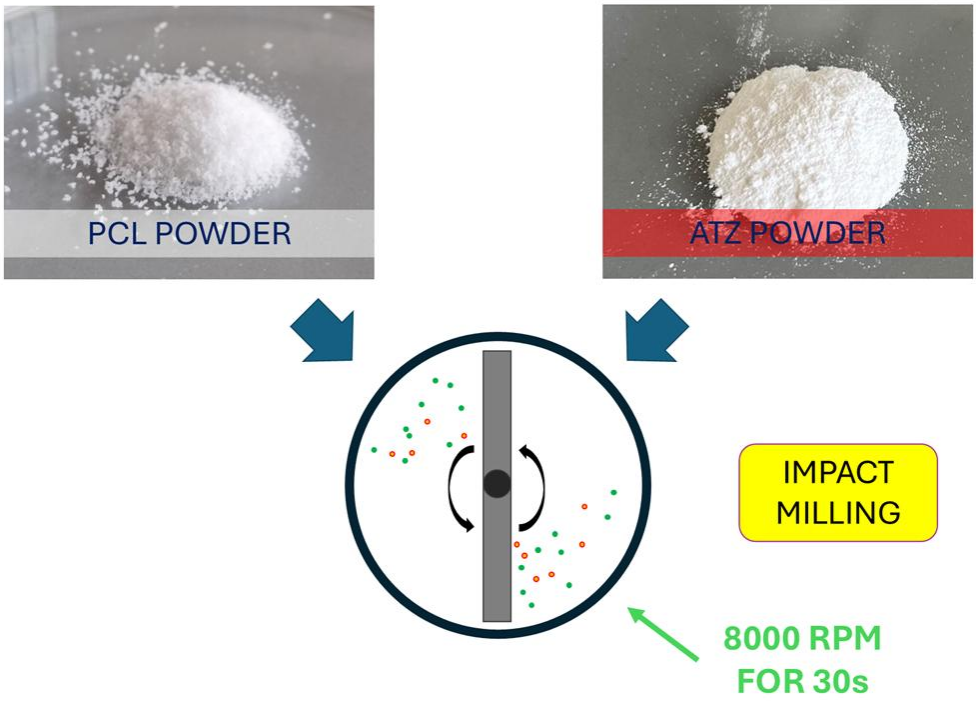

Figure 10. Schematic representation of PCL/ATZ composites materials: (a) solvent casting, (b) impact milling.

- two bioactive glasses made by solvent casting (Figure 11) with chloroform at 10 wt.%, PCL/SBA3 90/10 and PCL/SBA3_Cu 90/10 (Table 3). SBA3 glass powders < 20 μm (48% SiO_2, 26% Na_2O, 22% CaO, 3% P_2O_5, 0.43% B_2O_3, 0.57% Al_2O_3−mol%) were produced by the melting and quenching technique, followed by milling and sieving processes as reported by Miola et al. [87]. After that, copper was added to SBA3 powders using an ion-exchange procedure in a 0.01 M copper acetate solution for one hour at 37 °C.

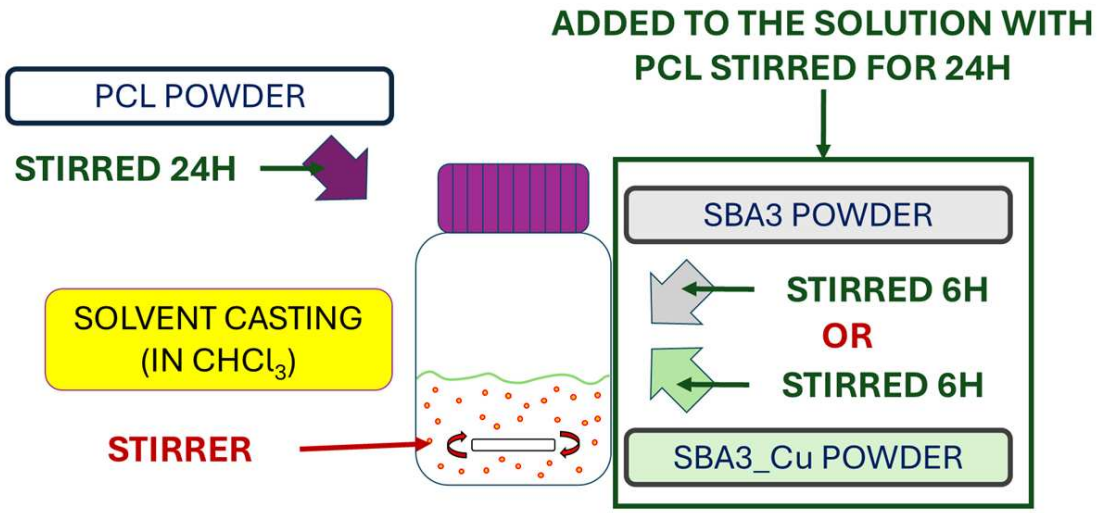

Figure 11. Schematic representation of PCL/Bioactive glass compounds solvent casting fabrication.

Neat PCL was considered as a control.

Table 3. Table representing percentages of filler in different composite materials.

Sample	PCL (%)	SBA3 (%)	SBA3_Cu (%)	ATZ (%)
PCL	100	/	/	/
PCL/ATZ 90/10	90	/	/	10
PCL/ATZ 80/20	80	/	/	20
PCL/ATZ 60/40	60	/	/	40
PCL/SBA3 90/10	90	10	/	/
PCL/SBA3_Cu 90/10	90	/	10	/

Three-dimensional planar specimens were fabricated using a thermoplastic pneumatic printhead on a BIO X 3D bioprinter (CELLINK, Bico Group, Gothenburg, Sweden). The STL (Standard Triangulation Language) models were created with SolidWorks software (Dassault Systèmes SolidWorks Corporation, Vélizy-Villacoublay, France), and the corresponding gcode files were generated by slicing them with the Repetier-Host program (Hot-World GmbH & Co. KG, Knickelsdorf, Germany). A glass surface of a Petri dish was used as print bed to ensure a clean and consistent interaction surface for each material. A standard

sample was design as a square measuring 15 mm × 15 mm, with a thickness of 0.65 mm and a 100% infill.

The previously mentioned square 3D-printed geometry had been cut using a 6 mm biopsy punch to create cylindrical discs, which were then utilised for SEM analysis, protein adsorption, cell adhesion, cell spreading, and cell viability testing. For mechanical testing, specimens with dimensions of 8 mm × 8 mm × 1 mm and 50 mm × 3 mm × 1 mm were printed. Clean chamber fan was kept on, printhead temperatures and others printing parameters are shown in Table n. A nozzle 0.4 mm in diameter was employed (Figure 12).

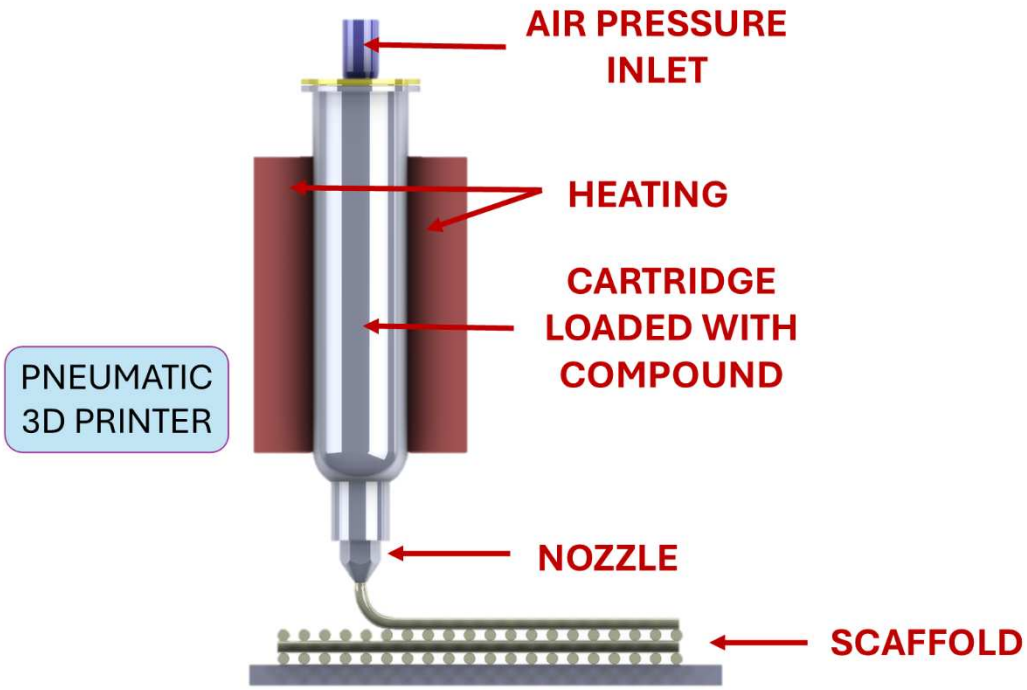

Figure 12. Schematic representation of 3D printing process.

Table 4. Parameters for 3D printing.

Sample	Print-head (°C)	Print-bed (°C)	Speed (mm/s)	Pressure (kPa)
PCL	110/115	25/30	2	190
PCL/ATZ 90/10	120	25	2	190
PCL/ATZ 80/20	125	25	2	190
PCL/ATZ 60/40	145	25	2	190
PCL/SBA3 90/10	115	30	2	190
PCL/SBA3_Cu 90/10	115	30	2	190

2.2. Microscopy

A scanning electron microscope (Phenom XL G2 Desktop SEM, Thermo Fisher Scientific, Waltham, MA, USA) was used to examine the microstructure of each sample. The samples underwent the following procedures prior to examination: distilled water washing, 70% ethanol–water solution rinsing, ultrasonography cleaning in absolute ethanol for 20 minutes, air drying in a chemical hood, and application of a thin conductive layer of gold. For micrographs and analysis, the instrument settings used were 10 kV of voltage in a MAP setup with a Back Scatter Detector (BSD).

EDX analysis was also carried out to evaluate dispersion degree of different fillers. Only PCL/ATZ samples were also observed in cross-section through a frozen bath in liquid nitrogen to induce a brittle fracture.

2.3. Roughness

Both contact-based and optical profilometers were used to analyse the samples' surface roughness in accordance with ISO 21920 (for profile R parameters) and ISO 25178 (for areal S parameters). Two stylus profilometers (Form Talysurf PGI Novus S 10, Taylor Hobson Limited, Leicester, UK / Phenom XL G2 Desktop SEM, Thermo Fisher Scientific, Waltham, MA, USA) with precision ceramic balls that are calibrated by an interferometric setup to be traceable to the International Systems of Unit (SI) were used to create the contact-based test. A cut-off of 0.08 mm and a total length of 8 mm were chosen for the measurements. Roughness parameters were obtained using the contact technique: Skewness (Rsk), Kurtosis (Rku), Maximum Height (Rz), Root Mean Square Height (Rq), and Arithmetical Mean Height (Ra).

The second method measured the topography using the optical profilometer (Sensofar Plμ 2300, Barcelona, Spain) in confocal mode. The surface size was 254.64 μm × 190.90 μm, and the cut-off was set at 0.08 mm since a Nikon LU Plan Fluor 50×/0.80 objective was employed. In order to avoid damaging the specimen, optical measurements were made before performing tactile measurements in order to quantify the surface parameters of Arithmetical Mean Height (Sa), Root Mean Square Height (Sq), Maximum Height (Sz), Skewness (Ssk), and Kurtosis (Sku). Three stylus measurements and five optical measurements were performed on each sample. Digital Surf's Mountains Map Premium 10 (Besancon, France) was used to process the profiles and topographies.

2.4. Contact Angle and Surface Free Energy Evaluation

Surface wettability was assessed on all samples with the exception of PCL/ATZ samples prepared whit solid mixing. Double-distilled water (dH_2O) and

diiodomethane (CH_2I_2) were used in the test, which was conducted using a Biolin Scientific Theta Lite Optical Tensiometer (Stockolm, Sweden). The sessile drop method was used to determine the contact angle. The integrated high-resolution camera was used to take a picture of the drop on the sample for every liquid drop (1 µL in volume) that was dispensed. Integrated software was used to extract and fit the drop profiles. Contact angles between the fitted function and the base line were computed at the liquid/solid interface. The contact-angle measurement was carried out five times on various locations for every sample and liquid probe.

As suggested by Waldner, C. et al., the Owens–Wendt–Rabel–Kaelbele (OWRK) approach [88] was used to determine a value of surface free energy. The dispersive (γ^D), polar (γ^P), and total (γ) components were computed using basic linear regression. As shown in Table 5, the properties of dH_2O and CH_2I_2 were used as standard constants to carry out the interpolation.

Table 5. Standard parameters of water and di-iodomethane.

Liquid	γ (mN/m)	γ^P (mN/m)	γ^D (mN/m)
Water	72.8	43.7	29.1
Di-iodomethane	50	2.6	47.4

2.5. Protein Adsorption

A 5% solution of bovine serum albumin (BSA) in phosphate buffered saline (PBS) was made and used to cover PCL/SBA3(Cu) and PCL/ATZ compounds in order to measure the amount of protein adsorbed onto the samples. After 20 minutes of incubation at 37 °C, the specimens underwent two PBS washes. The overall amount of adsorbed protein was measured by eluting the samples with a Tris Triton buffer (10 mM Tris, pH 7.4; 100 mM NaCl; 1 mM EDTA; 1 mM EGTA; 1% Triton X-100; 10% glycerol; and 0.1% SDS) for 10 minutes, and the resulting solution was then quantified using the Pierce™ BCA Protein Assay Kit (Life Technologies, Carlsbad, CA, USA) following the manufacturer's guidelines.

2.7. Ion release

The samples were kept in alpha-MEM in a cell culture incubator for 3, 7, and 15 days in order to examine the ionic release brought on by the presence of bioactive glasses. Using an ICPOES (iCAP Pro X, Thermo Fisher Scientific, Waltham, MA, USA), the supernatants were collected and examined. By creating a multi-elemental standards solution at the required concentration from single elemental stock solutions (1000 mg/L, Merck, Darmstadt, Germany), the concentrations of Al, P, Ca, B, Si, and Cu in the solutions were measured using an external calibration method.

2.8. Gel Permeation Chromatography

Using a GPC Max Viscotek fitted with a Malvern TDA 305 that includes refractive index (RI), right-angle laser-light scattering (RALS), low-angle laser-light scattering (LALS), and intrinsic viscosity (IV) detectors, the average molecular weight of PCL/ATZ samples was calculated by Gel Permeation Chromatography (GPC) analysis. PCL scaffold sections were cut, dissolved in 5 mg/mL chloroform, and then filtered through a 0.22 μm PTFE filter. With exclusion limits of 106 and 103 Da, a column set consisting of a precolumn and two Phenogel Phenomenex columns was used to inject and elute 100 μL in CHCl3 (Romil) at a flux of 0.8 mL/min. Every sample was assessed using universal calibration, which uses polystyrene standards with a molecular weight between 560 and 2.45 kDa.

2.9. Mechanical properties

Instron 5966 dynamometer (Norwood, MA, USA) was utilized to perform tensile tests on PCL/ATZ and PCL/SBA3(Cu) composites materials at room temperature. Samples were clamped with clamps positioned 2 cm apart. Specimens were subjected to an initial loading rate of 1 mm/min until 0.2% deformation. At this point, rate increase up to 20 mm/min until break for ATZ samples and 30 mm/min until break for specimens containing bioactive glass. Regarding PCL/SBA3(Cu) samples, parameters recorded include Young's modulus (E), elongation at yield (εy), strength at yield (σy), tensile strength (σb), and elongation at break (εb). For PCL/ATZ compounds, parameters recorded were Young's modulus (E), elongation at break (%), and tensile strength (MPa). The determination of mechanical properties is the result of the average of ten repetitions for each group for bioactive glass composites materials and five repetitions for each group for PCL/ATZ samples.

Hardness was evaluated for both group of materials, Vickers hardness (HV) and Young's moduli (EiT) for PCL/SBA3(Cu) (FISCHERSCOPE HM 2000 XYm Helmut Fischer GmbH, Sindelfingen, Germany) [61] and Shore D scale for PCL/ATZ samples (Durometer, Sauter model).

2.10. Cell experiments

2.10.1. Cell Culture

ASC52hTert cell line (ASCs), adipose-derived mesenchymal cells (ATCC, Manassas, VA, USA) were used to test SBA3, SBA3_Cu and ATZ composite materials. Human microvascular endothelial cells (HMEC-1) (CLS, Cell Lines Service GmbH, Eppelheim, Germany) were used to investigate the biocompatibility of the samples composed by bioactive glass. Primary Palatal Fibroblasts (PF) and

human gingival epithelioid cell line (SG) were utilized to characterize the biological response in vitro of PCL/ATZ samples. PF were cultured in Alpha-MEM, 10% FBS, and 5% penicillin (100 U/mL) streptomycin (100 µg/mL). SG cells were maintained in an RPMI-1640 medium (Euroclone, Pero, Italy) with 10% FBS, 100 U/mL penicillin, and 100 µg/mL streptomycin.

Both ASCs and HMEC-1 were grown in ASC medium (Mesenchymal Stem Cell Basal Medium (ATCC PCS-500-030) with a Mesenchymal Stem Cell Growth Kit (ATCC PCS-500-040)) and MCDB131 medium (Life Technologies, Carlsbad, CA, USA) + 1% L-Glutamine, 10% foetal bovine serum (FBS), 1% Penicillin (100 U/mL), Streptomycin (100 µg/mL), 1 ug/mL Hydrocortisone, and 10 ng/mL EGF (Merck KGaA, Darmstadt, Germany). PF were cultured in Alpha-MEM. SG cells were cultured in RPMI-1640 medium (Euroclone, Pero, Italy) with 10% FBS, 100 U/mL penicillin, and 100 µg/mL streptomycin.

To perform the following experiments, ASCs were seeded in Alpha-MEM (Life Technologies, Milano, Italy) with 10% FBS, 1% Penicillin (100 U/mL) Streptomycin (100 µg/mL), and HMEC-1 were kept in their expansion medium. All cells were cultured in an incubator at 37 ◦C and with a 5% CO2 atmosphere.

2.10.2. Cell Adhesion and Cell Spreading

On PCL/SBA3, PCL/SBA3_Cu, ASCs and HMEC-1 were seeded at a density of 8000 cells per well culture plates. PF and SG were plated on PCL/ATZ samples with a concentration of 4000 cell per well culture plates. For adhesion test cells were incubated for 40 min for PF and SG, ASC and HMEC-1 were incubated 8 min instead. All samples were then fixed by 4% paraformaldehyde solution, and washed with PBS; cell nuclei were stained by 1 µM DAPI (Merck, Darmstadt, Germany) for 15’ at 37 ◦C. Cells were cultured for 24 hours before being fixed and stained with DAPI for cell nuclei and Phalloidin (Cell Signalling technology, Danvers, MA, USA) for the cytoskeleton in order to assess cell spreading.
A Nikon Eclipse Ti-E microscope equipped with Nikon Plan 40×/0.75 and Nikon Plan 10×/0.10 objectives was used to take the pictures. The "Analyse particles" feature of the ImageJ software (Version 2.14.0/1.54f, ImageJ, U. S. National Institutes of Health, Bethesda, MD, USA) was used to count the number of cell nuclei. The contours of a single cell on each acquired field were obtained by pre-training with other similar images in a controlled learning process after four images were obtained in triplicate for each sample type and processed using the cellpose cyto3 segmentation algorithm.

Then, using the Set Measurements function in Fiji/ImageJ, 12 distinct shape descriptors area, perimeter, best fitting ellipse (BFE) major axis, BFE minor axis, BFE aspect ratio, BFE angle, circularity, roundness, solidity, Feret's diameter, Feret's angle, and minimum calliper diameter were measured for every detected cell. Six of these twelve descriptors area, perimeter, BFE aspect ratio, BFE angle, circularity, and roundness were chosen as pertinent characteristics for assessing cell

morphology. MATLAB (MATLAB R2024a; The MathWorks, Inc., Natick, MA, USA) was used to analyse and plot the data.

2.10.3. Cell Viability

PF and SG were plated on PCL/ATZ samples at a density of 10,000 cells/well, ASCs and HMEC-1 were seeded on samples containing bioactive glasses at a density of 10,000 cells/well. Lastly, ASCs were plated on PCL/ATZ samples produced both in solvent casting and solid mixing at a density of 25000 cells/well. 96-well culture plates were adopted for all experiments and were cultured in their cell culture media. Cell viability was assessed after 1, 3, and 7 days for PF/SG – PCL/ATZ and for ASC/HMEC-1 – PCL/SBA3(Cu). The test was conducted on in vitro cultures using the CellTiter-GLO kit (Promega, Milan, Italy) following the manufacturer's instructions. Cell viability was reported in terms of relative light units (RLU).

2.11. Data management

Statistical analyses were carried out using STATA software (version 18.0; StataCorp, College Station, TX, USA). A one-way ANOVA was applied to evaluate differences in group variances across different time points, while a T-test was employed to identify statistically significant differences between groups. A p-value below 0.05 was considered indicative of statistical significance.

3. Results

3.1. Microscopy

3.1.1. Morphology of compounds with bioactive glass

The surface morphologies of PCL/SBA3 90/10 (Figure 13b) and PCL/SBA3_Cu 90/10 (Figure 13c) were comparable. In both composite materials, the filler particles were uniformly distributed and widely spread. In PCL/SBA3 90/10, no visible bioactive glass aggregates were found. Small filler aggregates were seen in PCL/SBA3_Cu 90/10, though, most likely as a result of the copper-doped particles' (highlighted in red circles) higher electrostatic charge, which caused them to cluster and form nucleation centres. The surface of Neat PCL (Figure 13a) was uniformly clean, with a few tiny flaws that were probably brought on by the printing process.

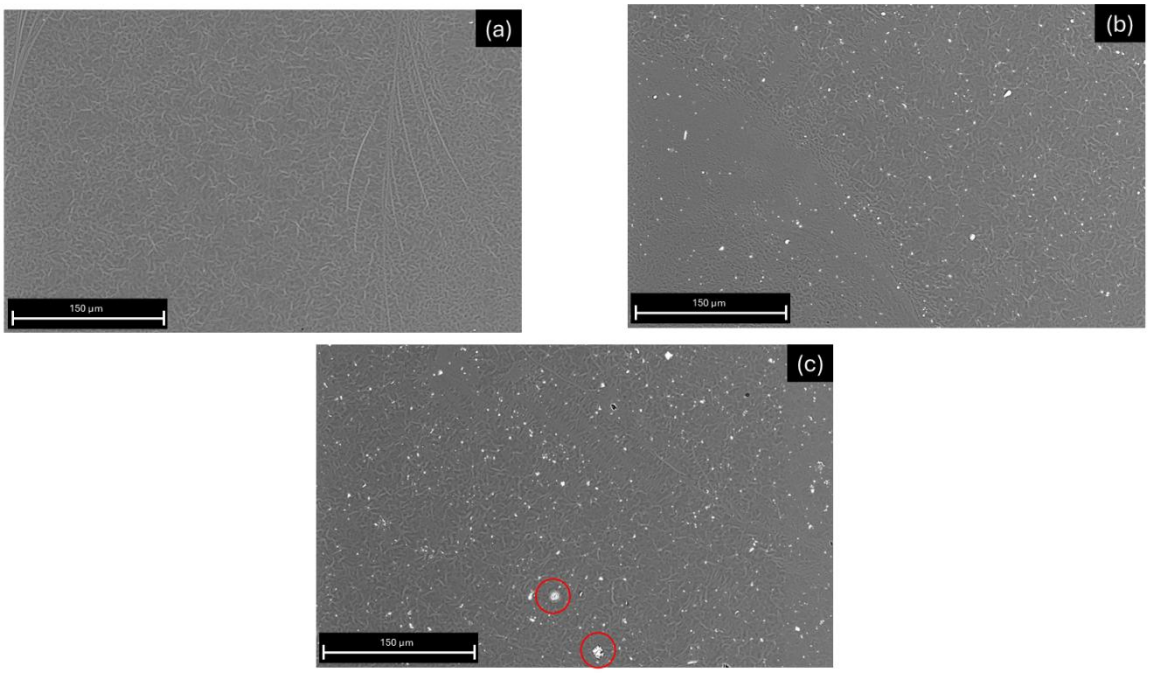

Figure 13. SEM images of PCL/bioactive glass compounds: (a) neat PCL, (b) PCL/SBA3 90/10, (c) PCL/SBA3_Cu 90/10, at 1000× magnification (filler aggregates indicated in red).

The composition of the composite materials was verified by EDX spectroscopy on the sample surfaces (Table 6). In pristine PCL, the only observed constituents were carbon, nitrogen, and oxygen, which compose the molecular backbone of the

polymer matrix. Spectroscopy of PCL/SBA3 90/10 identified all of the main filler elements, including calcium, silicon, and sodium, in relation to the bioactive glass components. Additionally to these components, copper which was added through the ion-exchange process was also found in the PCL/SBA3_Cu 90/10 sample. To prevent cytotoxic effects, a little amount of copper can be added to the glass composition using the ion-exchange process, but only at the surface level.

As demonstrated by Piatti et al. [89], the percentage of the glass elements (calcium, silicon, and sodium) was found to be higher in PCL/SBA3_Cu 90/10 than in PCL/SBA3 90/10. This is most likely because of the increased agglomeration and surface exposition (Figure 13c).

Table 6. Table representing chemical surface composition through EDX analysis.

Samples	Carbon		Nitrogen		Oxygen		Sodium		Silicon		Calcium		Copper	
	Atomic Conc. [%]	Weight Conc. [%]	Atomic Conc. [%]	Weight Conc. [%]	Atomic Conc. [%]	Weight Conc. [%]	Atomic Conc. [%]	Weight Conc. [%]	Atomic Conc. [%]	Weight Conc. [%]	Atomic Conc. [%]	Weight Conc. [%]	Atomic Conc. [%]	Weight Conc. [%]
Neat PCL	70.8	65.1	5.1	5.5	24.0	29.4	-	-	-	-	-	-	-	-
PCL-SBA3 90/10	72.5	63.0	5.5	5.6	15.2	17.6	2.9	4.8	2.5	5.1	1.3	3.9	-	-
PCL-SBA3_Cu 90/10	59.8	46.2	0.9	0.9	24.9	25.6	4.9	7.2	6.0	10.9	3.4	8.7	0.1	0.4

3.1.2. Morphology of compounds containing ATZ

The PCL/ATZ 90/10 surface appears in Figure 14a, whereas Figures 14b and 14c show the PCL/ATZ 80/20 and 60/40 surfaces. A growing number of white dots in composites indicates the augmenting presence of ATZ filler. Even though every sample was printed on the same glass support for the smoothest and most consistent surface, the ATZ distribution became more uniform as the amount of filler increased. When the maximum ATZ % was applied, the leftover ATZ stripes that were aligned with the printing direction vanished (Figure 14c). This was probably caused by the print head moving through the 3D printing process (Figure 14a, b).

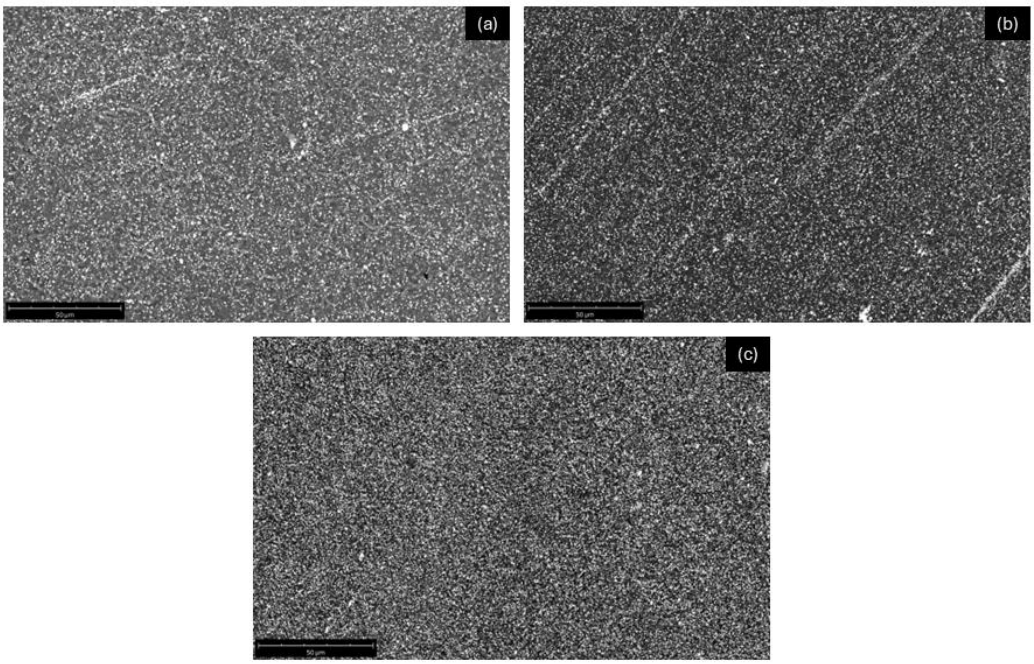

Figure 14. Scanning electron microscopy images of PCL/ATZ composites materials: (a) PCL/ATZ 90/10, (b) PCL/ATZ 80/20 and (c) PCL/ATZ 60/40.

3.1.3. Different morphologies between solvent casting and solid mixing

The filler was distributed primarily uniformly across the polymer surface of the 3D-printed material made from solvent casting (a, b, c), as seen by the secondary electron scans (Figure 15). The ATZ powder disperses less well over the scaffold surface in the composites made by dry mixing (d, e, f). The predominant occurrence of filler agglomerates (red circle in Figure 15d) indicates the filler's inadequate dispersion. It's also noteworthy that when the filer concentration rises, the agglomerates get bigger and more numerous. Additionally, the composites produced by the dry-mixing process clearly show the presence of voids.

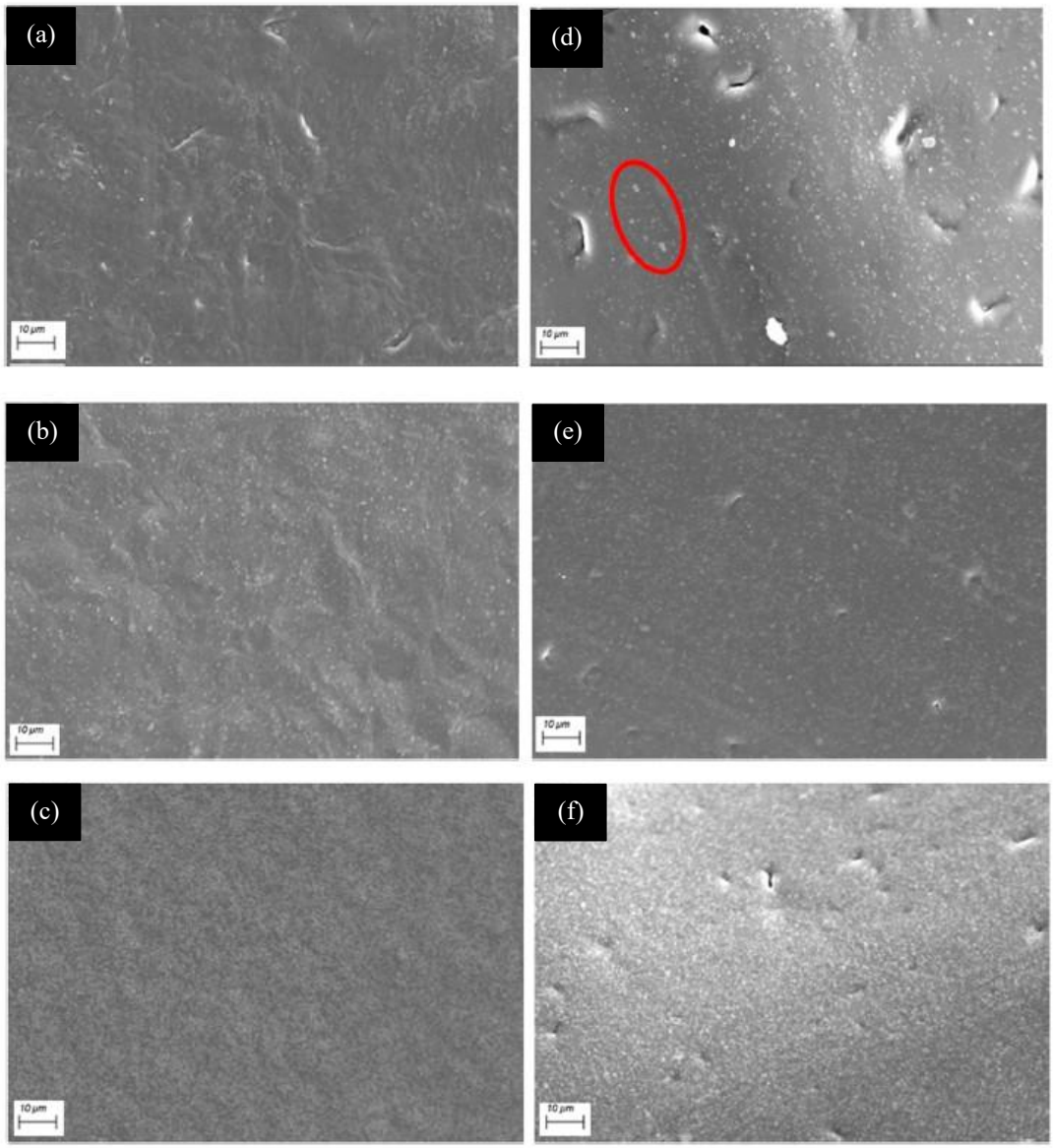

Figure 15. SEM of PCL compounds surfaces: (a) 3D-printed PCL/ATZ 90/10 *SC*, (b) PCL/ATZ 80/20 *SC*, (c) PCL/ATZ 60/40 *SC*, (d) PCL/ATZ 90/10 *M*, (e) PCL/ATZ 80/20 *M* and (f) PCL/ATZ 60/40 *M* (relevant filler agglomeration is indicate with the red circle).

The composites' fracture surfaces validate the ATZ dispersion that was previously noted in Figure 15. Only the SEM pictures of PCL/ATZ 90/10 *SC* and *M* are shown in Figure 16a and Figure 16b, respectively. The pictures unequivocally show that, in comparison to solid mixing, the solvent casting process enables a superior dispersion and distribution of the filler within the polymer matrix. ATZ agglomerations are seen (highlighted in blue). Moreover, voids (white arrows) in Figure 16b reveal a weak filler–polymer interface and show that ATZ particles are separated from the matrix. As suggested by the data obtained from the other

composites, this behaviour indicates a low affinity between the ceramic filler and the polymer matrix.

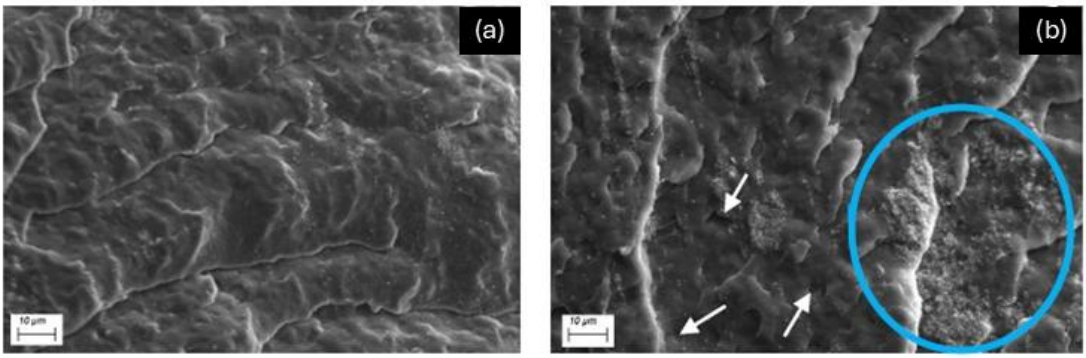

Figure 16. Cross-sections SEM images of (a) PCL/ATZ 90/10 *SC* and (b) PCL/ATZ 90/10 *M* (voids are indicate by white arrows and ATZ agglomeration are indicate by blue circle).

3.2. Roughness

The surface roughness of the materials was analysed by taking into account various parameters such as the R parameters and the S parameters.

3.2.1. Bioactive glass compounds surface roughness

According to Table 7, the composite materials' areal average roughness (Sa) was marginally lower than that of the neat polymer; in fact, the only material that deviated considerably from PCL was PCL/SBA3_Cu 90/10 ($p = 0.048$). In comparison to neat PCL, the fillers considerably reduced the Ra of both SBA3 and SBA3_Cu 90/10 PCL composites ($p < 0.01$). Additionally, the Rz parameter behaved consistently across all specimens. In particular, PCL/SBA3_Cu 90/10 had lower Rz values than PCL/SBA3 90/10 and neat PCL (both $p < 0.01$).

Table 7. Profile Roughness (R) and areal texture (S) parameters of PCL/SBA3 samples.

Sample	R_a (µm)	R_z (µm)	S_a (µm)
Neat PCL	0.266 ± 0.034	0.157 ± 0.029	0.077 ± 0.009
PCL/SBA3 90/10	0.218 ± 0.049	0.074 ± 0.022	0.076 ± 0.015
PCL/SBA3_Cu 90/10	0.211 ± 0.028	0.055 ± 0.006	0.063 ± 0.006

3.2.2. ATZ compounds surface roughness

PCL/ATZ 60/40 samples had the highest roughness values, as measured by the averages Ra and Sa, as well as the root-mean-square values R_q and S_q (Tables 8 and 9, respectively). Skewness parameters (S_{sk}) were around 1.5 for both unmixed PCL and PCL/ATZ 60/40, indicating an uneven distribution of peaks and valleys, with more peaks than valleys. The huge exponent used to calculate these values resulted in a considerable standard deviation; indeed, parameters S_{sk} and S_{ku} are sensitive to the presence of spikes as well as narrow and deep troughs.

To determine whether there was a positive or negative trend in the mean values, the measurements were conducted again. As shown by values of Kurtosis (S_{ku}) greater than 3, PCL/ATZ 80/20 displayed values of Skewness that were close to 0, indicating a uniform distribution of peaks and valleys with a highly crisp profile. A leptokurtic distribution of valleys or peaks ($S_{ku} > 3$) was present in every sample. Regardless of the proportion of ATZ, all composites displayed greater Maximum Height (S_z) values than unmixed PCL.

Table 8. R profile roughness measured with the stylus profilometer.

Sample	R_a (µm)	R_q (µm)	R_{sk}	R_{ku}	R_z (µm)
Neat PCL	0.103 ± 0.019	0.173 ± 0.035	3.273 ± 0.525	40.284 ± 15.079	0.613 ± 0.107
PCL/ATZ 90/10	0.122 ± 0.016	0.234 ± 0.102	-1.597 ± 2.772	85.616 ± 43.422	0.711 ± 0.063
PCL/ATZ 80/20	0.106 ± 0.002	0.143 ± 0.007	-0.644 ± 0.594	10.712 ± 9.004	0.641 ± 0.010
PCL/ATZ 60/40	0.207 ± 0.001	0.306 ± 0.002	-1.003 ± 0.252	11.909 ± 2.799	1.296 ± 0.015

Table 9. S areal texture parameters measured with the optical profilometer.

Sample	S_a (µm)	S_q (µm)	S_{sk}	S_{ku}	S_z (µm)
Neat PCL	0.122 ± 0.021	0.238 ± 0.066	1.825 ± 2.553	27.887 ± 22.966	4.233 ± 2.141
PCL/ATZ 90/10	0.135 ± 0.007	0.227 ± 0.016	-1.049 ± 1.461	91.515 ± 91.120	13.005 ± 6.984
PCL/ATZ 80/20	0.062 ± 0.004	0.102 ± 0.017	-0.123 ± 12.575	1400.3 ± 1223.8	13.861 ± 5.640
PCL/ATZ 60/40	0.155 ± 0.035	0.248 ± 0.057	1.515 ± 5.255	163.07 ± 217.170	14.631 ± 4.138

Surface roughness measurements were also carried out to evaluate the possible influence of solvent casting and solid mixing process on the selected surface parameters: arithmetical mean height (S_a), Skewness (S_{sk}), and Kurtosis (S_{ku}). Table 10 shows the analysis results.

In terms of the S_a parameter, all of the samples are very different from one another; it's also important to note that for both the *SC* and *M* samples, the increase in filler from 10 to 20 weight percent resulted in a notable decrease in this parameter. The S_a parameters for the *M* and *SC* techniques are identical, with the

exception of PCL/ATZ 60/40. The S_{sk} values, which were all positive for the *SC* samples and negative for the *M* samples, show a significant difference between *SC* and *M*. Specifically, the large number of negative peaks was the cause of the *M* samples' negative S_{sk} values.

Table 10. S areal texture parameters of composites materials made on *M* and *SC*.

Sample	S_a (µm)	S_{sk}	S_{ku}
Neat PCL	6.461	-0.082	2.841
PCL/ATZ 90/10 *M*	15.73	-0.293	2.751
PCL/ATZ 80/20 *M*	11.63	-0.022	2.503
PCL/ATZ 60/40 *M*	10.71	-0.147	2.601
PCL/ATZ 90/10 *SC*	9.175	0.061	2.707
PCL/ATZ 80/20 *SC*	7.484	0.504	3.035
PCL/ATZ 60/40 *SC*	11.03	0.371	2.716

3.3. Contact angle and SFE

3.3.1 Bioactive glasses contact angles and SFE

As seen in Figure 17, a wettability test was conducted to assess the materials' reaction to both hydrophilic and lipophilic environments. With values above 70°, neat PCL showed the largest and statistically significant ($p < 0.05$) contact angle (CA) of any sample in the hydrophilic environment (Figure 17a), suggesting that it was the least hydrophilic substrate. The highest affinity for the polar solvent was suggested by PCL/SBA3 90/10, which had an even lower CA than PCL/SBA3_Cu 90/10, which showed a CA just below 70°. Out of all the materials, neat PCL exhibited the most lipophilic behaviour in the lipophilic environment (Figure 17b), with the lowest CA (~30°, $p < 0.05$).

While PCL/SBA3 90/10 had the highest CA (~60°) and, thus, the least lipophilic behaviour, PCL/SBA3_Cu 90/10 showed a CA of about 50°.

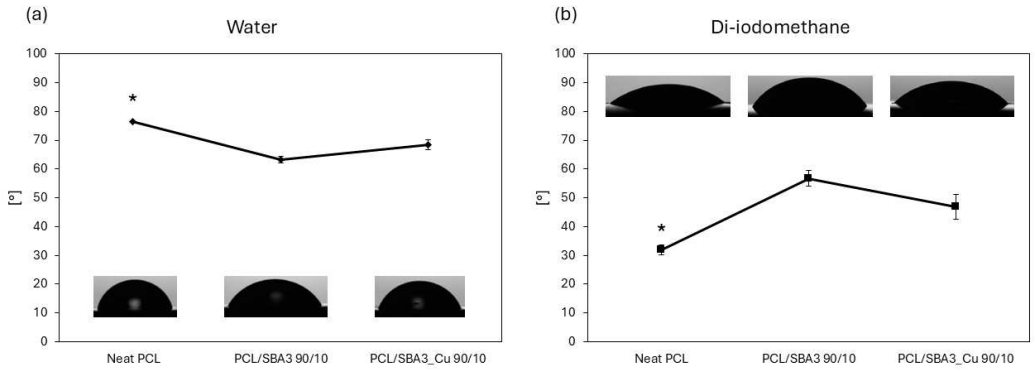

Figure 17. Contact angle of sample surfaces with bioactive glass in hydrophilic (a) and lipophilic (b) environments.

The surface free energy (SFE) calculation also clearly shows the impact of bioactive glass in the polymeric matrix in comparison to PCL. As indicated in Table 11, neat PCL had the highest total surface energy (γ) value when compared to the two composite materials, although not in a statistically relevant way. The only relevant differences have been detected between the polar component of SFE of PCL and PCL/SBA3 90/10, as well as its dispersive component compared again to PCL/SBA3 90/10 samples ($p < 0.05$).

Table 11. All surface energy components calculated on PCL/SBA3 compounds through OWRK method.

Sample	Surface Energy Total (mN/m)	Surface Energy Polar (mN/m)	Surface Energy Dispersive (mN/m)
Neat PCL	42.7	2.7	40
PCL/SBA3 90/10	39.2	17.6	21.5
PCL/SBA3_Cu 90/10	38.8	9.9	28.9

3.3.2. ATZ compounds contact angles and SFE

By using a polar solvent and an apolar solvent to carry out the standard optical contact angle (OCA) measurement, the materials' reactions to both hydrophilic and lipophilic environments were evaluated. All materials observed dH_2O contact angles stayed constant at around 67°, and there were no noticeable differences across the samples (Figure 18a). Only PCL/ATZ 80/20 was the specimen that showed a marginally different but not statistically significant result (Figure 18a). Unmixed PCL exhibited the maximum contact-angle value (41°) in a lipophilic environment with CH_2I_2, whereas other composite materials displayed a lower contact angle, measuring 36° in PCL/ATZ 90/10 and 23° in PCL/ATZ 80/20 and

PCL/ATZ 60/40 (Figure 18b). Between PCL and PCL/ATZ 80/20, there was just one statistically significant difference ($p < 0.05$).

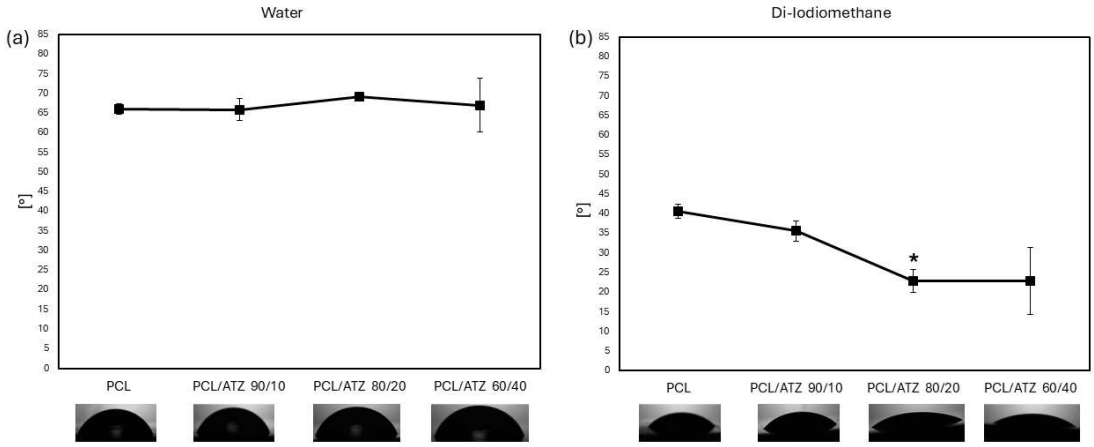

Figure 18. Surface contact angle of PCL/ATZ composites materials. (a) hydrophilic environment and (b) lipophilic environment.

SFE analysis of wettability data carried out on PCL/ATZ composite materials shows that neat PCL has a lower total surface energy (γ) component (41.81) compared to other samples (Table 12), although not in a statistically relevant way. PCL/ATZ 60/40 shows the highest value (46.74), while PCL/ATZ 90/10 has the lowest value (43.42) among composites. Regarding the polar component of surface energy, PCL/ATZ 90/10 has the highest value between composites (8.68) and PCL/ATZ 80/20 has the lowest (4.77). Concerning dispersive component of surface energy, PCL/ATZ 80/20 show the highest value (41.80) and PCL/ATZ 90/10 display the littlest (34.74). Only the dispersive component of Neat PCL differed in a statistically relevant way from PCL/ATZ 80/20.

Table 12. All surface energy components calculated on PCL/ATZ compounds through OWRK method.

Sample	Surface Energy Total (mN/m)	Surface Energy Polar (mN/m)	Surface Energy Dispersive (mN/m)
Neat PCL	41.81	9.83	31.97
PCL/ATZ 90/10	43.42	8.68	34.74
PCL/ATZ 80/20	46.57	4.77	41.80
PCL/ATZ 60/40	46.74	5.93	40.81

3.4. Protein adsorption

3.4.1. PCL/SBA3 composites materials protein affinity

The amount of BSA adsorbed on the planar samples of neat PCL, PCL/SBA3 90/10, and PCL/SBA3_Cu 90/10 is shown in the protein adsorption graph (Figure 19). Although never in a statistically significant way, the composites had a propensity to increase adsorption when compared to neat PCL, particularly materials containing copper, which had the largest amount of adsorbed proteins (about 0.3 mg/mL) of all specimens tested.

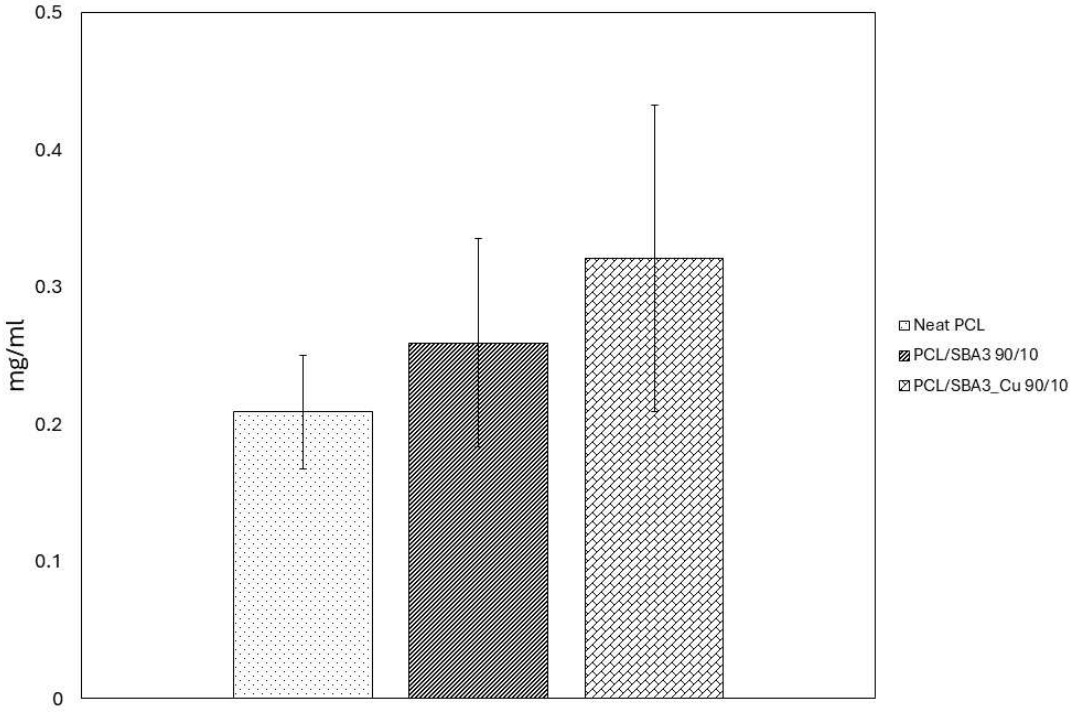

Figure 19. BSA protein adsorbed on PCL/SBA3 samples surfaces.

3.4.2. PCL/ATZ compounds protein affinity

The amount of BSA protein adsorbed on the sample surfaces tended to rise with the percentage of ceramic filler, according to the protein adsorption graph (Figure 20). When compared to composites, unmixed PCL showed the lowest value (~15 mg/mL). Specifically, among all studied conditions, PCL/ATZ 60/40 had the highest value (~45 mg/mL), and the results are significantly different from those of the pure polymer ($p < 0.05$). Although the mean values of PCL/ATZ 80/20 and PCL/ATZ 90/10 were similar, only the former deviated from PCL in a way that was statistically significant ($p < 0.05$).

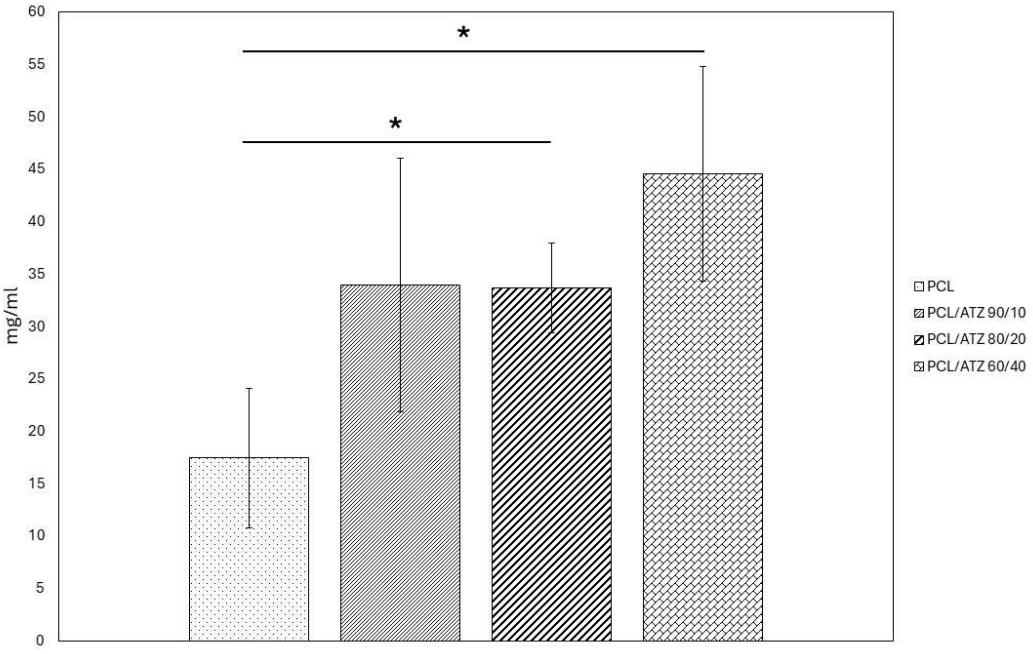

Figure 20. BSA protein adsorbed on PCL/ATZ samples surfaces.

3.5. Culture medium ions analysis

Table 13 reports the concentrations of B, Si, and Cu found in the culture media after 1, 3, and 7 days of incubation. These concentrations demonstrate an increasing pattern over time. To emphasise the impact of incubation time, the report additionally provides the concentration of these elements in the pure alpha-MEM culture medium. Since the concentration of Al was consistently found to be below the technique's detection limit for each sample, it is not reported.

On the other hand, the alpha-MEM's high P and Ca concentrations (26 and 62 mg/L, respectively) obscured the elements' release from the materials. PLC/SBA3 demonstrated an exceptionally high release of Si (up to 62.6 mg/L after 7 days), although the release of B from the two bioactive glasses was marginally higher from PLC/SBA3 than from its copper-doped analogue. Ultimately, as imagined, Cu was exclusively released from PLC/SBA3_Cu, and it measured notable amounts in the culture medium (3.39 mg/L).

Table 13. Culture medium ions concentrations after different incubation times.

Sample	B (mg/L)	Si (mg/L)	Cu (mg/L)
Alpha-MEM	0.17 ± 0.03	0.23 ± 0.01	/
PCL/SBA3 90/10 Day 1	0.85 ± 0.06	46.3 ± 0.3	/
PCL/SBA3 90/10 Day 3	1.16 ± 0.03	53.8 ± 0.4	/
PCL/SBA3 90/10 Day 7	2.14 ± 0.06	62.6 ± 0.2	/
PCL/SBA3_Cu 90/10 Day 1	0.36 ± 0.04	9.5 ± 0.1	1.33 ± 0.01
PCL/SBA3_Cu 90/10 Day 3	0.81 ± 0.03	23.0 ± 0.1	2.58 ± 0.02
PCL/SBA3_Cu 90/10 Day 7	1.63 ± 0.03	31.2 ± 0.2	3.39 ± 0.03

3.6. GPC

To assess if PCL's molecular weight changed following 3D printing, GPC studies were carried out. Table 14 lists the PCL-based composites' number-average molecular weight (M_n), intrinsic viscosity (IV), and weight-average molecular weight (M_w) as evaluated by both solvent casting and solid mixing. The partial deterioration of PCL caused by the 3D printing process was demonstrated by the comparison of the Mw and Mn of neat PCL with the 3D printed material PCL *M* and *SC*. With increased ATZ loading, a progressive reduction in molecular weights and intrinsic viscosity was noted for the composites made via solution mixing. The comparison of the molecular weights of the two types of composites (obtained from solvent casting and solid mixing) showed that PCL was further degraded by the mill's mixing operation. In fact, the *M* composites' M_w and M_n values were lower than those of their solvent casting equivalents.

Table 14. GPC results obtained from PCL/ATZ *M* and *SC* composites.

Sample	X_c (%)	M_w (Da)	M_n (Da)	IV (dL/g)
Neat PCL	52 ± 1	97,411	55,172	1.135
PCL *M*	49 ± 2	61,757	32,876	1.068
PCL *SC*	50 ± 1	65,251	37,449	1.092
PCL/ATZ 90/10 *M*	53 ± 2	53,169	44,876	0.991
PCL/ATZ 80/20 *M*	53 ± 1	46,690	39,111	0.829
PCL/ATZ 60/40 *M*	52 ± 2	31,073	23,041	0.637
PCL/ATZ 90/10 *SC*	54 ± 1	68,895	51,668	1.094
PCL/ATZ 80/20 *SC*	54 ± 1	59,614	39,653	0.936
PCL/ATZ 60/40 *SC*	54 ± 1	49,227	27,322	0.649

3.7. Mechanical characterization

3.7.1. PCL/SBA3 mechanical behaviour

Table 15 summarizes the scaffolds mechanical properties, such as tensile strength (σ_b), elongation at break (ε_b), elongation at yield (ε_y), strength at yield (σ_y), and Young's modulus (E). Young modulus was statistically significantly increased when SBA3 was added to PCL. Interestingly, we were able to obtain values of Young's modulus that were almost seven times greater than those of neat PCL when SBA3 particles and Cu were combined.

Table 15. Tensile test parameters of PCL/SBA3 samples.

Sample	E (MPa)	ε_y (%)	σ_y (MPa)	ε_b (%)	σ_b (MPa)
Neat PCL	51 ± 16	7.5 ± 0.8	14.3 ± 0.8	693 ± 60	23.4 ± 3.8
PCL/SBA3 90/10	252 ± 35	14.9 ± 3.2	12.7 ± 1.3	647 ± 48	17.8 ± 2.2
PCL/SBA3_Cu 90/10	369 ± 46	14.7 ± 1.5	13.9 ± 1.1	656 ± 47	21.1 ± 1.6

This result is consistent with the hardness values shown in Figure 21 below. Comparing the composite scaffolds to neat PCL revealed a slight reduction in yield strength and break characteristics, but an increase in elongation at yield.

Nevertheless, the composites preserved the ductile and yielding properties of neat PCL.

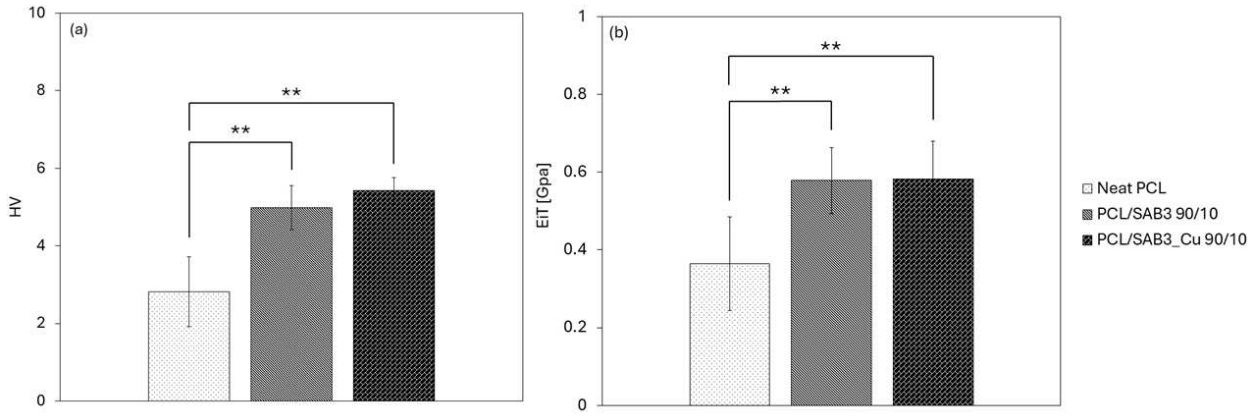

Figure 21. Hardness values HV (a) and EiT (b) of PCL/SBA3(Cu) samples.

Figure 18 illustrates the Vickers hardness (HV) and Young's modulus (EiT) outcomes. The addition of bioactive glass radically boosted the HV values of PCL ($p < 0.01$), in particular, Cu-doped bioactive glass nearly doubling the value. Also, the addition of SBA3 and SBA3_Cu results in a decrease of data standard deviation. Young's modulus showed a significant increase in EiT values for PCL/SBA3 90/10 and PCL/SBA3_Cu 90/10 samples ($p < 0.01$), resulting in lower data dispersion.

3.7.2. PCL/ATZ mechanical tests

The mechanical properties of PCL/ATZ samples were assessed through stress-strain and hardness tests (Table 16).

For *SC* composites, the Young's modulus (E) significantly increased as ATZ filler concentration rose, confirming the expected reinforcing effect described in the literature [90]. For example, E increased from 516 ± 37 MPa, in neat PCL, to 943 ± 205 MPa in PCL/ATZ 60/40 *SC*. Conversely, both elongation at break (ε_b) and tensile strength (σ_b) decreased with increased ATZ loading; ε_b dropped drastically from 581% in neat PCL to just 5% in PCL/ATZ 60/40 *SC*. Hardness (Shore D) also showed a slight, gradual increase.

In contrast, *M* samples showed a general reduction in mechanical properties as the ATZ amount increased. While PCL/ATZ 90/10 *M* composite was comparable to neat PCL, higher ATZ concentrations led to significant worsening of both E and ε_b . This mechanical decline is attributed to the formation of filler aggregates, voids and the degradation of the PCL polymer chains during the solid mixing process, which reduces the molecular weight as demonstrated by GPC analysis.

Table 16. Tensile tests and hardness parameters of PCL/ATZ pomposities from solid mixing (*M*) and solvent casting (*SC*).

Sample	E (MPa)	ε_b (%)	σ_b (MPa)	Shore D
Neat PCL	516 ± 37	581 ± 42	20.8 ± 2.7	56.2 ± 1.3
PCL/ATZ 90/10 *M*	521 ± 134	430 ± 36	22.1 ± 2.8	56.1 ± 2.8
PCL/ATZ 80/20 *M*	543 ± 277	348 ± 41	17.2 ± 1.1	65.5 ± 1.1
PCL/ATZ 60/40 *M*	246 ± 138	9.54 ± 4.46	10.2 ± 0.6	65.7 ± 4.5
PCL/ATZ 90/10 *SC*	630 ± 64	533 ± 43	21.6 ± 2.1	57.3 ± 2.1
PCL/ATZ 80/20 *SC*	810 ± 90	324 ± 26	15.2 ± 0.6	62.8 ± 2.5
PCL/ATZ 60/40 *SC*	943 ± 205	4.7 ± 0.7	9.1 ± 0.8	65.1 ± 3.1

3.8. Materials biocompatibility

3.8.1. PCL/SBA3 early cell adhesion and morphology

At 20 minutes, all samples showed adhesion of ASCs and HMEC-1 (Figure 22 a, b). The number of attached ASCs would appear to lead not only from neat PCL but also SBA3 composite, while the maximum value was observed for SBA3_Cu; these differences were found not to be significant.

In particular, the number of total adhered ASCs was significantly supported by PCL/SBA3_Cu 90/10, even if lower than neat PCL ($p = 0.063$). Only with HMEC-1 significant enhancement of cytocompatibility was shown for the PCL/SBA3 90/10 and the PCL/SBA3_Cu 90/10 compared to neat PCL ($p < 0.01$).

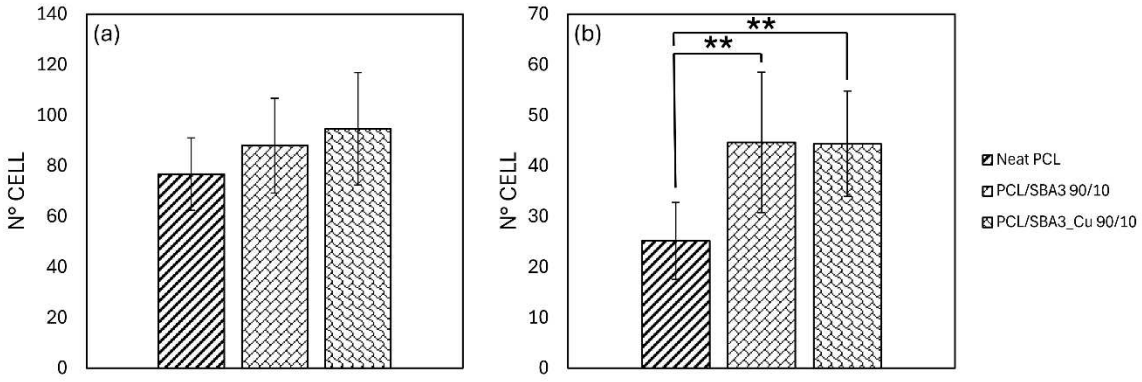

Figure 22. Figure representing data from adhesion assay. (a) ASCs and (b) HMEC-1 cell number on specimens after 20 min of incubation.

Cell spreading was quantitated based on confocal immunofluorescence microscopy images acquired at the same magnification (Figure 23). In the case of ASCs (Figure 23a–c), the average cell area (Figure 23g) on PCL/SBA3 90/10 was significantly larger compared to neat PCL and PCL/SBA3_Cu 90/10 ($p < 0.01$). These had a lower perimeter than PCL/SBA3 90/10 (Figure 23h). Neat PCL also consistently showed the highest perimeter (Figure 23h) and aspect ratio values (Figure 23i), and the lowest circularity value (Figure 23j), allowing for more cell elongation and filopodia outgrowth as was qualitatively observed. After 24 h of culture, the ASCs on PCL/SBA3_Cu 90/10 exhibited smaller sizes and a more rounded morphology in comparison to neat PCL and PCL/SBA3 90/10, which was in agreement with their lower mean area (Figure 23g), smaller perimeter (Figure 23h) and higher roundness values (Figure 23j). The aspect ratio was the only parameter where there was no significant difference between PCL/SBA3 90/10 and PCL/SBA3_Cu 90/10 ($p = 0.152$).

For HMEC-1 cells (Figure 23d−f), mean area, perimeter and aspect ratio (Figure 23g−i) values were significantly greater on neat PCL ($p < 0.01$ vs. PCL/SBA3_Cu 90/10), while the lowest roundness (Figure 23j). In contrast, PCL/SBA3_Cu 90/10 showed the lowest average of area, perimeter and aspect ratio (Figure 23g–i) and the highest roundness (Figure 23j). The PCL/SBA3 90/10 displayed intermediate properties between the other two states.

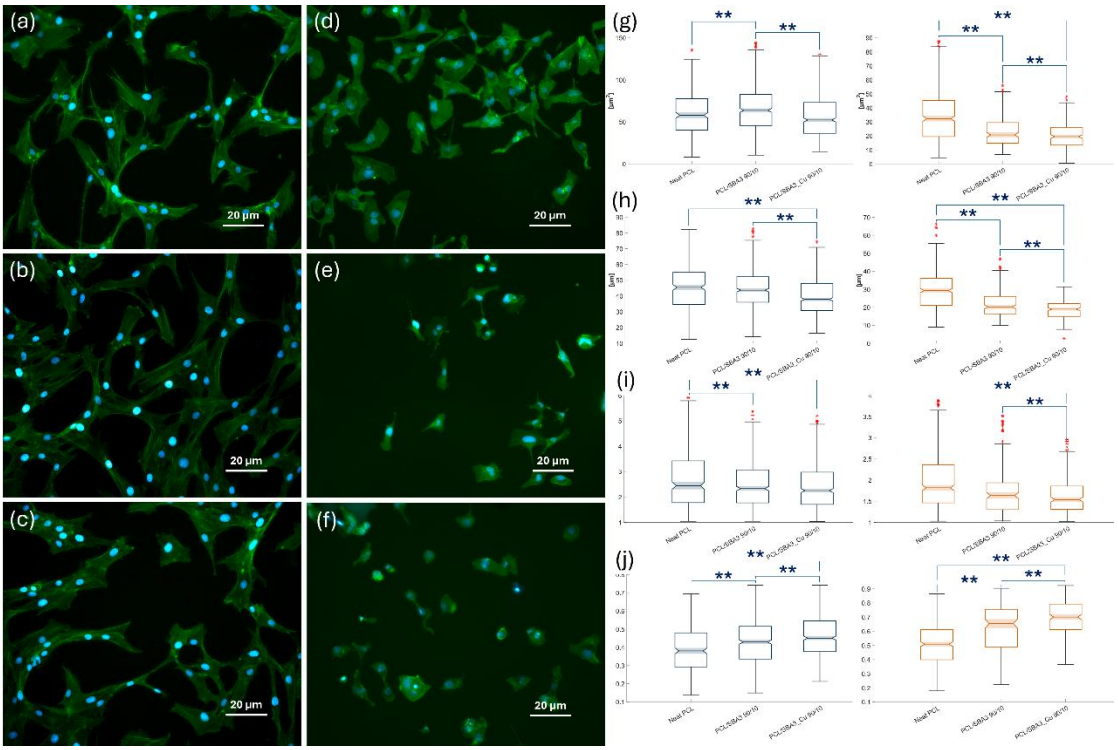

Figure 23. Immunofluorescence images (blue represent the nuclei and green indicates cytoskeleton): (a) ASCs on neat PCL, (b) ASCs on PCL/SBA3 90/10, (c) ASCs on PCL/SBA3_Cu 90/10, (d) HMEC-1 on neat PCL, (e) HMEC-1 on PCL/SBA3 90/10, and (f) HMEC-1 on PCL/SBA3_Cu 90/10 after 24 h. Boxplot (blue for ASCs and orange for HMEC-1) representing (g) cell Area, (h) perimeter, (i) aspect ratio and (j) circularity.

3.8.2. PCL/ATZ early biological behaviour

All samples facilitated cell adhesion. In relation to PF (Figure 24a), it was observed that the number of adherent cells increased in direct proportion to the filler quantity within the composites. Specifically, PCL/ATZ 90/10 exhibited the lowest number of adherent cells on surface when compared to PCL/ATZ 80/20 and PCL/ATZ 60/40 (with respective p-values of 0.03 and 0.008), which demonstrated a rise in cell nuclei numbers. However, none of the composites surpassed the performance of pure PCL in a statistically relevant manner.

The addition of ATZ particles into the polymeric matrix improved the surface properties, triggering the adhesion of SG cells (Figure 24b). This enhancement was particularly notable in PCL/ATZ 80/20, which recorded the highest overall number of adherent cells in a statistically significant way ($p < 0.05$).

Cell spreading analysis, assessed through the Best Fitting Ellipse (BFE) angle in segmented cells, is illustrated in a polar histogram plot (Figure 24). In this instance, PF spreading exhibited a loss of partial orientation as the concentration of ATZ increased within the PCL matrix. This behaviour was not corroborated with

SG cells, likely due to their more rounded morphology and random distribution across surfaces.

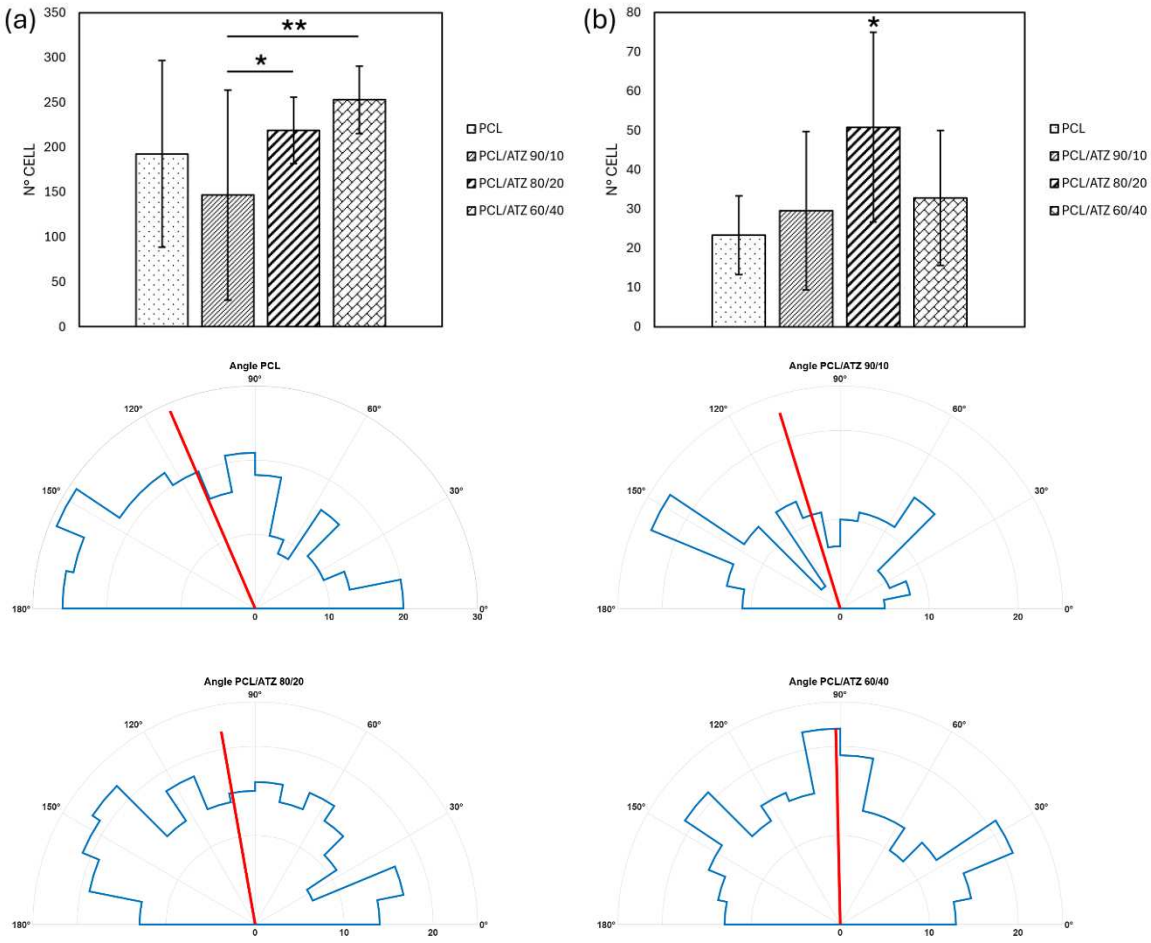

Figure 24. Graph representing PF (a) and SG (b) cell adhesion evaluated after 20 min of incubation ((*) for $p < 0.05$ and (**) for $p < 0.01$). Polar histogram plot of BFE angles measured on PF cell for all samples (blue the polar bins of the distributions, red line is the mean angle value).

Measurements of area and perimeter from PF images (Figure 25) indicated higher values for compounds containing ATZ compared to unmodified PCL samples. Notably, PCL/ATZ 80/20 and PCL/ATZ 60/40 showed significantly elevated values for both descriptors ($p < 0.05$).

In line with these findings, aspect ratio values were significantly lower for pure polymer compared to those containing fillers. The detailed metrics of circularity and roundness highlighted a statistically significant difference between PCL/ATZ 90/10 and unfilled PCL samples ($p = 0.004$ and $p = 0.017$). Overall, the total area occupied by cells is correlated with results from previous adhesion tests (Figure 24a). For SG cells, PCL/ATZ 80/20 displayed significantly smaller dimensions

concerning area and perimeter values related to cell spreading. Additionally, aspect ratio, circularity, and roundness were significantly lower for this composite while being higher for other measures in unfilled PCL samples ($p < 0.05$ and $p < 0.01$). The cumulative area measurements reported aligned with results from adhesion tests (Figure 24b).

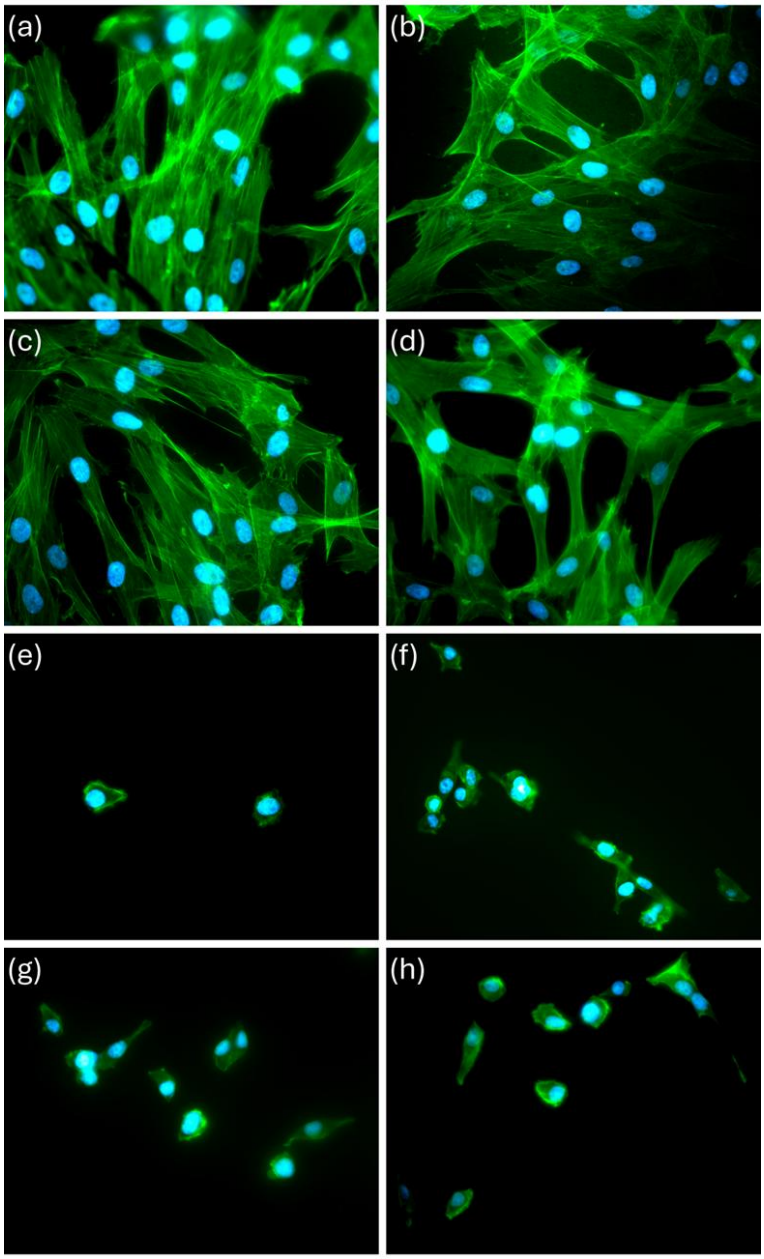

Figure 25. Immunofluorescence images (blue represent the nuclei and green indicates cytoskeleton): (a) PF on neat PCL, (b) PF on PCL/ATZ 90/10, (c) PF on PCL/ATZ 80/20, (d) PF on PCL/ATZ 60/40, (e) SG on neat PCL, (f) SG on PCL/ATZ 90/10, (g) SG on PCL/ATZ 80/20 and (h) PCL/ATZ 60/40 after 24 h incubation.

3.9. Viability assays

3.9.1. Long term viability of PCL/SBA3 composites materials

Following viability studies with two different cell lines, all tested biomaterials showed to be biocompatible since they allowed for the long-term proliferation of cells. ASCs (Figure 26a) also showed a significantly higher growth in PCL/SBA3 90/10 compared to neat PCL, at all the different time points considered. In contrast, the growth of ASCs was not improved on PCL/SBA3_Cu 90/10; they behaved in a similar manner as neat PCL.

In contrast, HMEC-1 cells (Figure 26b) initially show a lower proliferation compared to neat PCL but then proliferated well on both PCL/SBA3 90/10 and PCL/SBA3_Cu 90/10 composites, displaying significantly higher proliferation at days 3 and 7 than neat PCL ($p < 0.05$).

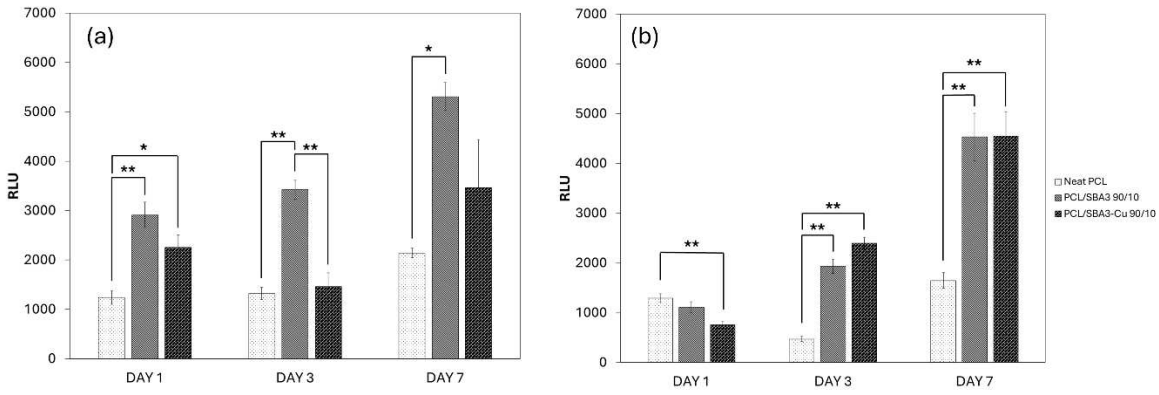

Figure 26. Cell viability values at 1, 3, and 7 days measured on each sample, (a) ASCs and (b) HMEC-1.

3.9.2. Long term behaviour of PCL/ATZ compounds

The PF cells showed similar growth in all samples after 1 and 3 days. However, on day 7, there was a significant decrease in the proliferation of PF cells cultured on PCL/ATZ 60/40 ($p < 0.01$) and PCL/ATZ 80/20 ($p < 0.05$) when compared to neat PCL and PCL/ATZ 90/10 material (Figure 27a).

With respect to viability, SG cells showed lesser absolute values as compared to PF. The SG cells proliferation was significantly higher on day 3 for the PCL/ATZ 80/20 when compared to other composites ($p < 0.05$). On day 7, the proliferation of SG cells on composites was similar and significantly better than with neat PCL (Figure 27b). These findings imply the role of the filler as an inducer for SG cell growth.

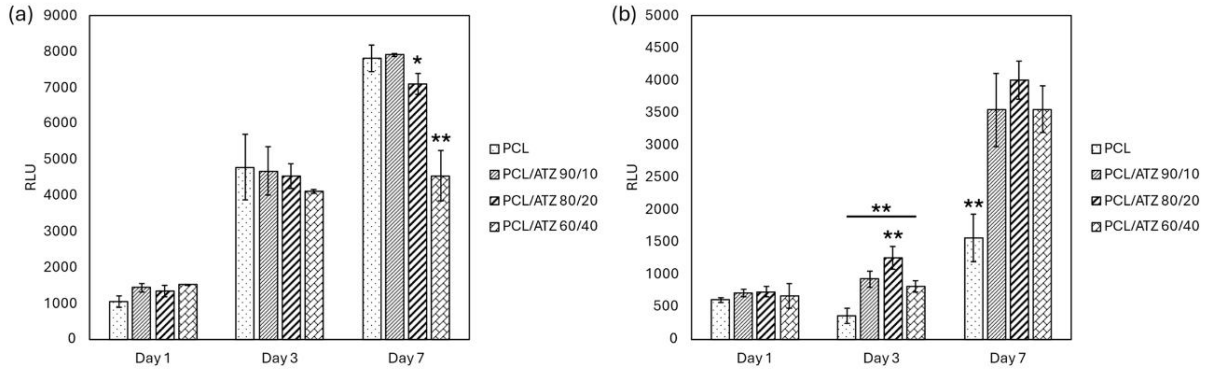

Figure 27. Cell viability of PF (a) and SG (b) after 1, 3, and 7 days ((*) for $p < 0.05$ and (**) for $p < 0.01$).

Two mixing methods, solvent casting and solid mixing trough impact milling, were tested in terms of long-term biocompatibility to determine which method is best and thus optimize the production process.

The viability tests conducted over 3, 7, and 14 days showed an increase in RLU values, which confirm proliferation of the cells (Figure 28). On day 3, there were no significant differences in ASC proliferation of any samples tested, and the transduced cells' growth was comparable in all conditions. The *SC* samples took slightly higher values than milled ones, but it's worth mentioning that the *SC* sample did not reach significance ($p = 0.018$).

This tendency was maintained on day 7, with the exception of the PCL/ATZ 90/10 *SC* group that significantly exceeded its milled counterpart (PCL/ATZ 90/10 *M*) in growth ($p << 0.01$).

Conversely, at 14 days, a significant difference was seen between the *SC* and *M* samples for the PCL/ATZ 80/20 and PCL/ATZ 60/40, with both showing significantly higher values when prepared by casting compared to milling ($p = 0.003$ and $p = 0.001$, respectively).

As such, it can be deduced that solvent casting resulted in a higher degree of cell proliferation compared with milling.

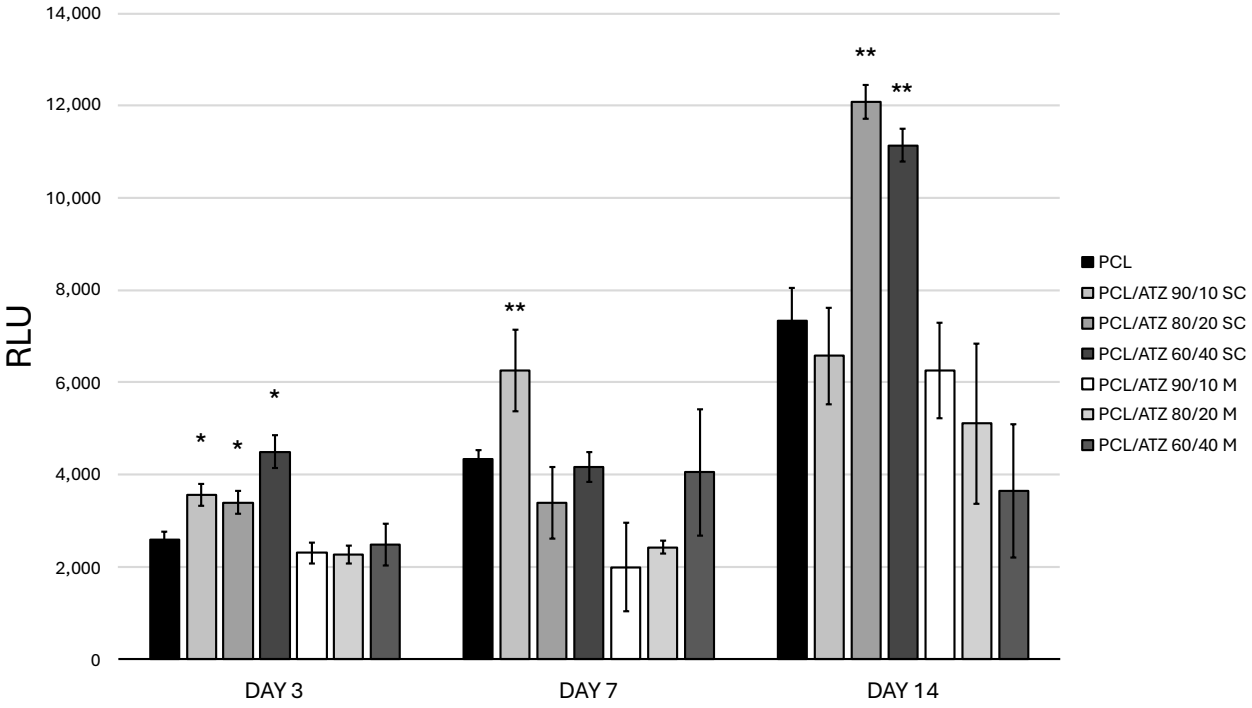

Figure 28. RLU values of ASCs after 3, 7 and 14 days ((*) for $p < 0.05$ and (**) for $p < 0.01$).

4. Discussion

This thesis aimed to investigate PCL composite materials suitable for the fabrication of bone substitutes and usable in the field of regenerative medicine. The PCL was mixed with two different types of fillers.

The first typology is silica-based bioactive glass [80], SBA3, and its counterpart doped with copper, SBA3_Cu. In this case, PCL/SBA3(Cu) blends were produced with 10 wt.% of filler by solvent-casting and samples were manufactured through 3D printing.

The second filler was ATZ, and the resulting composite material was used to test the differences between two mixing methods: solvent casting with chloroform (our gold standard) and solid mixing with impact mill [63]. PCL-ATZ mixtures were prepared at three different filler concentrations, 10, 20, and 40 wt.% both for solvent casted and solid mixed materials. Similar to the bioactive glass samples, the PCL-ATZ specimens were also produced using 3D printing.

In microscopic analysis, the general aspect of sample PCL/SBA3 90/10 and PCL/SBA3_Cu 90/10 were similar, where the filler particles on the surface seemed well dispersed in their individual state mixed throughout their respective polymer matrix. Nevertheless, in the case of the copper-doped one (PCL/SBA3_Cu 90/10), some small filler aggregates were occasionally observed, probably due to the higher electrostatic presence of Cu-doped bioactive glass particles [91]. EDX results indicated that the samples exhibited the expected composition and demonstrated especially a clear difference between undoped SBA3 and copper-doped bioactive glass models. A higher amount of sodium, silicon, and calcium in PCL/SBA3_Cu 90/10 than in PCL/SBA3 90/10 could be due to higher aggregation and surface exposure on the particles, as already reported elsewhere in the literature [92].

The morphological study of PCL/ATZ composites indicated that samples produced through solvent casting showed a more uniform distribution of filler in the polymer matrix. The presence of aggregates was primarily seen in dry-mixed specimens, even when the filler content was relatively low. However, although dry mixing is advantageous in terms of both economy and environment (reduced involvement of solvents and decreased processing time), efficient dispersion of the fillers does not necessarily occur, as also reported in previous papers [93,94]. Notably, SEM images of the solvent-casted PCL/ATZ composites presented residues of filler stripes, particularly in 90/10 and 80/20 PCL/ATZ formulations oriented parallel to the printing direction. This effect may be attributed to the behaviour of the polymer in swelling during extrusion and cooling down [95,96], with this swelling process influencing the volume as well as viscosity of the filler-enhanced region, favouring agglomeration at the interface between two adjacent printed strands. As found in Bellini [97] and Shofner et al. [98], the degree of swelling depends on the intrinsic properties of the material and the geometry of the extrusion nozzle. In the context of this, it is a tendency that inappropriate die swell

was decreased in cases of stiff fillers such as ceramics. This has also been seen for PCL/ATZ 60/40 composite material, but there were no stripes due to the lower polymer content in the material and the resulting greater surface uniformity.

Regarding surface roughness, the incorporation of silica-based bioactive glass into the PCL matrix resulted in a slight decrease in the average surface roughness, as indicated by Sa parameter. A statistically significant difference was observed only between neat PCL and the PCL/SBA3_Cu 90/10 composite. Overall, the Sa values (show samples with a very smooth surfaces were detected) obtained ranging from 0.077 μm for neat PCL to 0.063 μm for PCL/SBA3_Cu 90/10 classified all the samples as having very smooth surfaces. More pronounced variations were detected through linear roughness measurements: Ra values decreased from neat PCL to PCL/SBA3_Cu 90/10, while Rz values ranged from 0.157 μm to 0.055 μm, indicating that the copper-doped composite featured smoother peaks and valleys compared with the pristine polymer. However, caution is required when interpreting these parameters. Since Ra and Rz describe roughness along a single line, they may not fully capture the 3D topographical variations of the surface. In contrast, parameters such as Sa provide a more comprehensive representation of roughness by accounting for variations across the entire surface area. Despite the fact that such a smooth topography may not be ideal for clinical bone substitute applications where moderate roughness can enhance osseointegration it is particularly advantageous for in vitro experiments focused on isolating and evaluating the biological response to the chemical composition of the material [99].

The low dispersion quality of the filler observed in PCL/ATZ *M* samples may also explain their Ssk values. The presence of pits in these materials is likely related to the formation of weak interfaces caused by the aggregation of filler particles, which can persist even after the 3D printing process. For the solvent casted PCL/ATZ composites, the Sz parameter increased progressively with filler content, in agreement with the expectation that neat PCL would display the smoothest surface. Among all the tested formulations, the PCL/ATZ 60/40 composite exhibited the highest roughness values (Ra, Sa, Rq, and Sq), indicating a marked topographical modification induced by the ceramic filler. The addition of ATZ also influenced the skewness (Ssk) of the surface profile (like in the case of PCL/ATZ *M* specimens): values ranged from negative for PCL/ATZ 90/10 (−1.049) to positive for PCL/ATZ 60/40 (1.515), with the intermediate composition (PCL/ATZ 80/20) displaying a value close to zero. This trend suggests that the surfaces of the 90/10 and 60/40 composites were characterized by an asymmetrical distribution of valleys and peaks predominantly valleys in the former and peaks in the latter while the 80/20 composite presented a more balanced topography. Interestingly, the PCL/ATZ 80/20 formulation displayed somewhat unpredictable behaviour in terms of surface roughness. It exhibited Sa values roughly half those of the other samples but showed an exceptionally high kurtosis (Sku = 1400.3 ± 1223.8), almost an order of magnitude greater than that of the other specimens. Such a high Sku value indicates the presence of extremely sharp and narrow peaks on the surface, reflecting a highly irregular but localized topographical pattern.

As derived from contact angle measurements, both SBA3(Cu) composites showed much higher hydrophilicity (lower hydrophobicity) than neat PCL according to previous work [100]. The total SFE did not differ significantly from one sample to another. However, the polar and dispersive parts of SFE indicated slight differences in preference toward hydrophilic or lipophilic media of the materials.

In the same way, wettability analyses of PCL/ATZ composites showed a surface moderately hydrophilic (contact angle dH_2O CA around 67°) showing a general tendency toward lipophilic media not far from other polymer systems [101]. This tendency seemed to be enhanced by the presence of the filler, even though a statistically significant difference was found only between neat PCL (CA = 41°) and PCL/ATZ 80/20 (CA = 23°). Consistent with these findings, the total surface energy (γ) of neat PCL and PCL/ATZ 90/10 were slightly higher than those of composite samples containing more ATZ, even though not in a relevant way. This can be related to the well-known hydrophobic behaviour of ATZ [102], which may cause its inclusion in the polymer matrix to result in an increase in its dispersive component of surface energy, although this is not statistically significant either.

BSA protein adsorption onto SBA3(Cu) materials shows a clear tendency to increase the amount of protein adsorbed on the samples despite the high standard deviation. Neat PCL has the least affinity and PCL/SBA3_Cu 90/10 has the greatest affinity in terms of interaction with biological molecules [103]. Higher surface free energies and greater wettability contribute to increased levels of the adhesion and proliferation of cells on these surfaces, as has been demonstratively verified by many researchers [104–106]. In addition, interactions between dispersive components and polar components can alter the shape of adsorbed protein molecules. These changes then affect the way cells behave after they have stuck to the surfaces: how readily they adhere, how directly they spreads, and consequently proliferate [107].

In the case of PCL/ATZ composites, a higher ATZ content also favoured protein adsorption. The PCL/ATZ 60/40 sample, for example, showed a threefold increase in protein adsorption over neat PCL. Since all the sample materials were based on the same PCL matrix, this enhancement must be ascribed to the presence of more ATZ particles at the surface. This enabled binding sites for protein attachment to be made available.

Bioactive glass blends were studied on alpha-MEM cell culture medium in order to improve the comprehension of biological response. After 1, 3, and 7 days of samples incubation times at 37 °C, the concentration of selected chemical elements phosphorus, calcium, aluminium, boron, silicon, and copper released in the medium was evaluated by ICP-OES. Aluminium was not detected throughout, but the detection of phosphorus and calcium was masked by their high levels in alpha-MEM (26 and 62 mg/L). Therefore, field experiments were focused on copper, silicon, and boron, which were revealed to be the most important elements potentially interacting with living organisms within the study.

GPC studies were carried out to analyse the influence of mixing on degree of degradation and molecular weight of PCL, before and after the 3D printing process. The molecular weight of PCL after 3D printing is less than that of unprinted PCL. It has also been observed that dry mixing leads to a higher loss of PCL molecular weight as opposed to solvent casting method, more precisely, those concentrations of ATZ on the polymer material show larger losses of molecular weight. As no molecular weight reduction is observed for the neat printed PCL after milling, it can be assumed that such a decrease in polymer molecular weight is due to degradation induced by dry mixing and prompted by the presence of ATZ. In general, an increased filler loading causes a reduced distance between the filler particles, thereby enhancing their agglomeration and reducing the matrix/filler interface area. This effect basically reduces the thermal stability of the polymer matrix and renders it prone to degrade.

The mechanical behaviour of tensile load was typical in three stages: involving the initial linear elastic stage, a plateau where plastic deformation occurred, and a final phase of densification or crystallization associated with a sharp increase in stress. The neat PCL scaffold possessed an elastic modulus, strength at yield and elongation correlated to the printing conditions employed during manufacturing [108,109]. Thanks to its intrinsically superior deformability, PCL can accommodate very extensive deformations without failure through brittle fracture that qualifies it especially for flexible and resilient applications. When SBA3, either undoped and copper-doped particles were added in the PCL matrix, there was a significant increase in the elastic modulus and also in elongation at yield. In contrast, the strength a yield and crack decreased only minimally. Several mechanisms can be responsible for the observed enhanced elongation at yield. Finely dispersed particles of bioactive glass may have played a role in enabling stress rollover to occur more uniformly throughout the matrix (which slowed down strain localization and macroscopic yield) [110]. On the other hand, a degree of weak interfacial bonding between glass and polymer could also enable dissipation mechanisms (e.g., glass pull-out and interfacial sliding) that dissipate energy and accommodate deformation prior to reaching the yield point in such a way as not to undergo complete fracture. All of these effects resulted in the elongation of an elastic/plastic zone and an added deformability of the composites, which was incorporated with hard fillers. It is noteworthy that, although stiff and brittle glass particles were added into it, the ductility or yielding-like behaviour of neat polymer was preserved for PCL-based composites. This is primarily due to the inherent toughness properties and high elongation at break of PCL matrix which still controls post-yield deformation behaviour in moderately (10 wt%) bioactive glass filled systems. Moreover, the interfacial adhesion of the polymer to the bioactive glass seems to be well balanced: strong enough so as not to mis-load and at the same time weak enough so that it does not significantly hinder polymer plastic deformation. Therefore, the addition of bioactive glass contributed to improving the stiffness of the material while maintaining its ductility. This balance between stiffness and flexibility renders these glass-reinforced PCL composites a potential candidate for

applications requiring good mechanical properties, such as load-bearing bioresorbable scaffolds. In addition, the homogeneity of the ceramic particles distributed in the flexible polymeric matrix somewhat mimics the composite nature of natural bone tissue. While their elastic moduli are still lower than those of cortical bone, this structural similarity indicates a future use in bone tissue engineering for clinical applications. The homogeneous distribution of bioactive glass in the PCL matrix and the good interface adhesion between two phases that resist the micro-voids [111] were also corroborated by hardness data. Specifically, the Vickers hardness values significantly increased with bioactive glass formulation, verifying the strengthening effect of the inorganic phase.

Conversely, the mechanical properties of PCL/ATZ composites were poorer and mainly due to polymer degradation as a result of the dry mixing process. In the final mechanical behaviour, both the distribution of filler and molecular weight of polymer matrix are important. Also, compounds obtained through impact milling presented fewer mechanical properties than the solvent casted ones, indicating that processing-induced degradation and inadequate filler dispersion could highly contribute to compromising the overall performance of the composites.

The biological response of the developed materials was investigated through a series of assays performed with several cell types: adipose-derived stem cells (ASCs), representing a mesenchymal stem cell model of osteoblast progenitors [112], and human microvascular endothelial cells (HMEC-1), used as a model for micro vessels [113]. Both cell types are crucial in the colonization of bone substitutes, as they play complementary roles in bone regeneration and vascularization. These two cell types were used to test PCL/SBA3(Cu) composite materials. Their behaviour on the tested materials, therefore, provides valuable insights for future applications. During the initial adhesion assay, where cells were allowed to attach for 20 minutes, ASCs and HMEC-1 exhibited clearly different adhesion patterns. While ASCs showed no statistically significant differences in adhesion among the substrates, HMEC-1 demonstrated a marked preference for the PCL/SBA3 90/10 and PCL/SBA3_Cu 90/10 composites over neat PCL. Such cell-type-dependent adhesion behaviours are consistent with findings previously reported for various substrates [114]. Morphometric analyses were performed after 24 hours of culture using immunofluorescence microscopy to assess the spreading and morphology of both cell lines. Interestingly, HMEC-1 cultured on neat PCL appeared more spread than on the composites, displaying the largest aspect ratio, mean area, and perimeter along with the lowest roundness values. In contrast, HMEC-1 on PCL/SBA3_Cu 90/10 showed smaller areas and perimeters, lower aspect ratios, and higher roundness, suggesting a more compact and less spread morphology. For ASCs, segmentation analysis revealed that cells on neat PCL exhibited the highest perimeter and aspect ratio, indicating greater elongation and filopodia formation. The largest mean area, however, was measured on PCL/SBA3 90/10, while the smallest area and highest roundness were found on PCL/SBA3_Cu 90/10. These results collectively suggest that neat PCL supported ASC elongation and cytoskeletal organization more efficiently than the composites, whereas copper-

doped materials induced a more restrained spreading behaviour. The relevance of these morphological trends became more apparent when examining cell viability at 1, 3, and 7 days, in correlation with ion release data. Despite the initial "difficulties" observed in HMEC-1 cultured on PCL/SBA3_Cu 90/10 at 24 hours, this effect was completely mitigated at later time points, when both composites significantly outperformed neat PCL in promoting cell proliferation. This behaviour aligns with literature reports on the pro-angiogenic effects of copper doping [115,116], suggesting that HMEC-1 cells experienced an adaptation phase to the ion-releasing environment. Moreover, the Cu concentration measured in the culture medium after 7 days remained below toxic levels [117].

For ASCs, both composites stimulated higher proliferation than neat PCL, but the cells displayed a clear preference for the SBA3-based material over its copper-doped counterpart. This response can be attributed to the differential release of boron and silicon ions. PCL/SBA3 90/10 released more boron than PCL/SBA3_Cu 90/10 at both day 1 and after 7 days, in line with Akdere et al., who observed enhanced ASC proliferation at non-toxic boron concentrations [118]. Similarly, silicon release was consistently higher in PCL/SBA3 compared to the copper-doped composite, which released roughly half those amounts. Since silicon is known to stimulate osteogenesis and cell proliferation in bone substitute materials [119,120], these results support the superior bioactivity of SBA3 over SBA3_Cu in sustaining both stem cell and endothelial cell growth.

Complementary experiments on the PCL/ATZ series revealed analogous patterns. In samples produced via solvent casting, cell viability assays showed a progressive increase in proliferation across all materials, with PCL/ATZ 80/20 *SC* displaying significantly higher RLU values after 14 days compared to PCL/ATZ 60/40 *SC*. Conversely, for solid mixed samples, cell proliferation initially increased with filler loading up to day 7 but decreased by day 14 in samples with higher ATZ content suggesting that solid mixed materials, though simpler to prepare, offered weaker cell-material interactions than solvent casted composites or neat PCL.

Subsequent biocompatibility tests on solvent casted PCL/ATZ samples using additional cell types PF and SG were designed to simulate the oral peri-implant mucosal environment. In early adhesion assays, PF cells displayed adhesion patterns that mirrored surface skewness (Ssk), a novel observation not previously reported. No correlation was found with kurtosis (Rku or Sku), contrasting with Frias Martinez et al. [121], who linked higher Rku values with increased fibroblast adhesion. These results reinforce earlier findings on the influence of topographical parameters like skewness and kurtosis in guiding cell differentiation [122]. Morphological analyses revealed that increasing ATZ content promoted PF cell spreading, with cells showing larger areas, higher numbers of filopodia, and reduced orientation along the printing direction. The most favourable conditions for PF spreading were observed on PCL/ATZ 90/10 and 80/20 surfaces. Interestingly, PCL/ATZ 80/20 also exhibited topographical features (low Sa, high Sku, and balanced Ssk) that supported early adhesion of SG cells, which adhered most strongly to this surface. SG morphology was notably rounder on neat PCL, while

surfaces presenting ATZ provided more favourable anchoring sites, although excessive filler loading (PCL/ATZ 60/40) slightly reduced adhesion. At 3 days, PCL/ATZ 80/20 continued to outperform the other samples in promoting proliferation, while at 7 days all ATZ composites showed superior cell viability compared to neat PCL, corroborating previous findings [123]. PF cells, however, exhibited a delayed reduction in proliferation on higher ATZ-loaded samples, possibly due to differentiation cues rather than cytotoxicity. Notably, PCL/ATZ 80/20 supported the highest number of focal adhesions per PF cell, indicating its strong potential for facilitating early adhesion in both models. Finally, the divergent proliferation behaviours observed between PF and SG are not surprising, as different cell types often interact uniquely with the same material surface [124]. This discrepancy may arise from distinct adhesion mechanisms fibroblasts rely on classical focal adhesion complexes, whereas epithelial cells such as SG attach via a basal lamina that requires specific proteins like laminins [125].

5. Conclusion

This project investigated the synthesis, characterization, and biocompatibility of polymer matrix composite materials for the construction of bone and soft tissue constructs. The formulations of PCL with various inorganic fillers illustrated that the tailor-made composition, processing route, and microstructuring approach can largely shape the resulting biomaterials' performance.

Regarding the PCL/SBA3 and PCL/SBA3_Cu systems, the addition of bioactive glass into the PCL matrix efficiently improved the physicochemical/biological performances of scaffolds without a negative impact on their inherent flexibility. Endothelial cell proliferation was promoted in the presence of copper-modified glass particles, possibly as stimulated via the release of angiogenic ions, and un-doped SBA3 contributed towards higher levels of mesenchymal stem cell growth. These results confirm the potential of these composites for concurrent osteogenic-angiogenic induction.

Long-term studies with 3D scaffolds on osteogenic differentiation of ASCs and the vessel-like organization of HMEC-1 implantation under dynamic culture conditions should be focused on in continued investigation. This advanced test-bed would allow the identification of the optimum formulation in terms of elemental composition, release kinetics, and filler loading, as well as to evaluate how these parameters determine their mechanical performance. Finally, in vivo preclinical investigations with large bone defect animal models will be necessary prior to clinical application to confirm the angiogenic and osteogenic properties of these biomaterials.

The work also contributed to the problem of environmentally friendly and sustainable disposal of composites. Two different manufacturing routes, solvent casting and impact milling (solvent-free process), were compared in order to evaluate the influence of mixing technique on mechanical and biological behaviours of PCL/ATZ composites. The results showed that the solvent casting led to scaffolds with a better mechanical performance than those obtained employing the solid mixing process. However, with higher ATZ contents in the impact-milled samples, molecular weight decreased and mechanical strength as well as biological response became less favourable. Of the formulations evaluated, PCL/ATZ 80/20 produced by solvent casting exhibited the most balanced properties, with high cell proliferation and reasonable mechanics. These results demonstrate that both processing conditions play a crucial role in determining the eventual function of composites, as well as warranting further investigations to evaluate the biological response of 3D printed structures prepared by using solvent casting.

Lastly, the PCL/ATZ composites demonstrated remarkable biological properties that render them suitable for applications other than bone tissue regeneration. Protein adsorption and adhesion of cells were enhanced by the incorporation of ATZ, which also affected cell spreading and viability in PF and SG

conditions. From this perspective, PCL/ATZ 80/20 showed the best results, with a suitable interface for SG cells and good adhesion and viability for PF cells. These findings indicate that this quite distinctive formulation may be a promising shield for functionalizing the transmucosal part of dental implants, enabling an improved mucosal seal and thus leading to less peri-implantitis.

Overall, in this thesis, a multifaceted approach of using polymeric matrices filled with bioactive and ceramic fillers portrayed an interesting scenario in controlling the mechanical, physicochemical, and biological responses of the composite biomaterials. By rational design and optimizing the processes, such systems are tailor-made for different purposes, from bone regeneration to integration into soft tissue, thereby promoting further multifunctional materials for regenerative medicine.

Bibliography

1. Amini, A.R.; Laurencin, C.T.; Nukavarapu, S.P. Bone Tissue Engineering: Recent Advances and Challenges. *Crit. Rev. Biomed. Eng.* **2012**, *40*, 363–408, doi:10.1615/CritRevBiomedEng.v40.i5.10.
2. Ho-Shui-Ling, A.; Bolander, J.; Rustom, L.E.; Johnson, A.W.; Luyten, F.P.; Picart, C. Bone Regeneration Strategies: Engineered Scaffolds, Bioactive Molecules and Stem Cells Current Stage and Future Perspectives. *Biomaterials* **2018**, *180*, 143–162, doi:10.1016/j.biomaterials.2018.07.017.
3. Giannoudis, P.V.; Dinopoulos, H.; Tsiridis, E. Bone Substitutes: An Update. *Injury* **2005**, *36*, S20–S27, doi:10.1016/j.injury.2005.07.029.
4. Laurencin, C.; Khan, Y.; El-Amin, S.F. Bone Graft Substitutes. *Expert Rev. Med. Devices* **2006**, *3*, 49–57, doi:10.1586/17434440.3.1.49.
5. Vacanti, J.P.; Langer, R. Tissue Engineering: The Design and Fabrication of Living Replacement Devices for Surgical Reconstruction and Transplantation. *The Lancet* **1999**, *354*, S32–S34, doi:10.1016/S0140-6736(99)90247-7.
6. Pourhajrezaei, S.; Abbas, Z.; Khalili, M.A.; Madineh, H.; Jooya, H.; Babaeizad, A.; Gross, J.D.; Samadi, A. Bioactive Polymers: A Comprehensive Review on Bone Grafting Biomaterials. *Int. J. Biol. Macromol.* **2024**, *278*, 134615, doi:10.1016/j.ijbiomac.2024.134615.
7. Langer, R.; Tirrell, D.A. Designing Materials for Biology and Medicine. *Nature* **2004**, *428*, 487–492, doi:10.1038/nature02388.
8. Hutmacher, D.W. Scaffolds in Tissue Engineering Bone and Cartilage. *Biomaterials* **2000**, *21*, 2529–2543, doi:10.1016/S0142-9612(00)00121-6.
9. Ansari, M.; Darvishi, A. A Review of the Current State of Natural Biomaterials in Wound Healing Applications. *Front. Bioeng. Biotechnol.* **2024**, *12*, 1309541, doi:10.3389/fbioe.2024.1309541.
10. Kamoun, E.A.; Kenawy, E.-R.S.; Chen, X. A Review on Polymeric Hydrogel Membranes for Wound Dressing Applications: PVA-Based Hydrogel Dressings. *J. Adv. Res.* **2017**, *8*, 217–233, doi:10.1016/j.jare.2017.01.005.
11. Chinta, M.L.; Gandam, P.K.; Parcha, S.R. Natural Polymer Based Hydrogel Systems for Wound Management. In *Natural Polymers in Wound Healing and Repair*; Elsevier, 2022; pp. 129–165 ISBN 978-0-323-90514-5.
12. Sulaeva, I.; Henniges, U.; Rosenau, T.; Potthast, A. Bacterial Cellulose as a Material for Wound Treatment: Properties and Modifications. A Review. *Biotechnol. Adv.* **2015**, *33*, 1547–1571, doi:10.1016/j.biotechadv.2015.07.009.
13. Ahmed, J.; Gultekinoglu, M.; Edirisinghe, M. Bacterial Cellulose Micro-Nano Fibres for Wound Healing Applications. *Biotechnol. Adv.* **2020**, *41*, 107549, doi:10.1016/j.biotechadv.2020.107549.
14. İnal, M.; Mülazımoğlu, G. Production and Characterization of Bactericidal Wound Dressing Material Based on Gelatin Nanofiber. *Int. J. Biol. Macromol.* **2019**, *137*, 392–404, doi:10.1016/j.ijbiomac.2019.06.119.
15. Buruaga-Ramiro, C.; Valenzuela, S.V.; Valls, C.; Roncero, M.B.; Pastor, F.I.J.; Díaz, P.; Martinez, J. Development of an Antimicrobial Bioactive Paper Made from Bacterial Cellulose. *Int. J. Biol. Macromol.* **2020**, *158*, 587–594, doi:10.1016/j.ijbiomac.2020.04.234.
16. Ferreira, A.M.; Gentile, P.; Chiono, V.; Ciardelli, G. Collagen for Bone Tissue Regeneration. *Acta Biomater.* **2012**, *8*, 3191–3200, doi:10.1016/j.actbio.2012.06.014.

17. Kisling, A.; Lust, R.M.; Katwa, L.C. What Is the Role of Peptide Fragments of Collagen I and IV in Health and Disease? *Life Sci.* **2019**, *228*, 30–34, doi:10.1016/j.lfs.2019.04.042.
18. Kareva, I.; Abou-Slaybi, A.; Dodd, O.; Dashevsky, O.; Klement, G.L. Normal Wound Healing and Tumor Angiogenesis as a Game of Competitive Inhibition. *PLOS ONE* **2016**, *11*, e0166655, doi:10.1371/journal.pone.0166655.
19. Ullah, S.; Chen, X. Fabrication, Applications and Challenges of Natural Biomaterials in Tissue Engineering. *Appl. Mater. Today* **2020**, *20*, 100656, doi:10.1016/j.apmt.2020.100656.
20. Kulig, K.M.; Luo, X.; Finkelstein, E.B.; Liu, X.-H.; Goldman, S.M.; Sundback, C.A.; Vacanti, J.P.; Neville, C.M. Biologic Properties of Surgical Scaffold Materials Derived from Dermal ECM. *Biomaterials* **2013**, *34*, 5776–5784, doi:10.1016/j.biomaterials.2013.02.055.
21. Sackett, S.D.; Tremmel, D.M.; Ma, F.; Feeney, A.K.; Maguire, R.M.; Brown, M.E.; Zhou, Y.; Li, X.; O'Brien, C.; Li, L.; et al. Extracellular Matrix Scaffold and Hydrogel Derived from Decellularized and Delipidized Human Pancreas. *Sci. Rep.* **2018**, *8*, 10452, doi:10.1038/s41598-018-28857-1.
22. Sullivan, D.C.; Mirmalek-Sani, S.-H.; Deegan, D.B.; Baptista, P.M.; Aboushwareb, T.; Atala, A.; Yoo, J.J. Decellularization Methods of Porcine Kidneys for Whole Organ Engineering Using a High-Throughput System. *Biomaterials* **2012**, *33*, 7756–7764, doi:10.1016/j.biomaterials.2012.07.023.
23. Luc, G.; Charles, G.; Gronnier, C.; Cabau, M.; Kalisky, C.; Meulle, M.; Bareille, R.; Roques, S.; Couraud, L.; Rannou, J.; et al. Decellularized and Matured Esophageal Scaffold for Circumferential Esophagus Replacement: Proof of Concept in a Pig Model. *Biomaterials* **2018**, *175*, 1–18, doi:10.1016/j.biomaterials.2018.05.023.
24. Hashimoto, Y.; Funamoto, S.; Kimura, T.; Nam, K.; Fujisato, T.; Kishida, A. The Effect of Decellularized Bone/Bone Marrow Produced by High-Hydrostatic Pressurization on the Osteogenic Differentiation of Mesenchymal Stem Cells. *Biomaterials* **2011**, *32*, 7060–7067, doi:10.1016/j.biomaterials.2011.06.008.
25. Zhong, C. Industrial-Scale Production and Applications of Bacterial Cellulose. *Front. Bioeng. Biotechnol.* **2020**, *8*, 605374, doi:10.3389/fbioe.2020.605374.
26. Nie, Z.; Wang, X.; Ren, L.; Kang, Y. Development of a Decellularized Porcine Bone Matrix for Potential Applications in Bone Tissue Regeneration. *Regen. Med.* **2020**, *15*, 1519–1534, doi:10.2217/rme-2019-0125.
27. Chuah, Y.J.; Kuddannaya, S.; Lee, M.H.A.; Zhang, Y.; Kang, Y. The Effects of Poly(Dimethylsiloxane) Surface Silanization on the Mesenchymal Stem Cell Fate. *Biomater. Sci.* **2015**, *3*, 383–390, doi:10.1039/C4BM00268G.
28. Zhao, Y.; Sun, Y.; Hang, R.; Yao, R.; Zhang, Y.; Huang, D.; Yao, X.; Bai, L.; Hang, R. Biocompatible Silane Adhesion Layer on Titanium Implants Improves Angiogenesis and Osteogenesis. *Biomater. Adv.* **2022**, *139*, 213033, doi:10.1016/j.bioadv.2022.213033.
29. Minati, L.; Migliaresi, C.; Lunelli, L.; Viero, G.; Dalla Serra, M.; Speranza, G. Plasma Assisted Surface Treatments of Biomaterials. *Biophys. Chem.* **2017**, *229*, 151–164, doi:10.1016/j.bpc.2017.07.003.
30. Dettin, M.; Conconi, M.T.; Gambaretto, R.; Pasquato, A.; Folin, M.; Di Bello, C.; Parnigotto, P.P. Novel Osteoblast-adhesive Peptides for Dental/Orthopedic Biomaterials. *J. Biomed. Mater. Res.* **2002**, *60*, 466–471, doi:10.1002/jbm.10066.

31. Zhang, Z.; Zeng, J.; Groll, J.; Matsusaki, M. Layer-by-Layer Assembly Methods and Their Biomedical Applications. *Biomater. Sci.* **2022**, *10*, 4077–4094, doi:10.1039/D2BM00497F.
32. Sahebalzamani, M.; Ziminska, M.; McCarthy, H.O.; Levingstone, T.J.; Dunne, N.J.; Hamilton, A.R. Advancing Bone Tissue Engineering One Layer at a Time: A Layer-by-Layer Assembly Approach to 3D Bone Scaffold Materials. *Biomater. Sci.* **2022**, *10*, 2734–2758, doi:10.1039/D1BM01756J.
33. Yamane, K.; Sato, H.; Ichikawa, Y.; Sunagawa, K.; Shigaki, Y. Development of an Industrial Production Technology for High-Molecular-Weight Polyglycolic Acid. *Polym. J.* **2014**, *46*, 769–775, doi:10.1038/pj.2014.69.
34. Zha, S.; Utomo, Y.K.S.; Yang, L.; Liang, G.; Liu, W. Mechanic-Driven Biodegradable Polyglycolic Acid/Silk Fibroin Nanofibrous Scaffolds Containing Deferoxamine Accelerate Diabetic Wound Healing. *Pharmaceutics* **2022**, *14*, 601, doi:10.3390/pharmaceutics14030601.
35. Kouketsu, A.; Shimizu, Y.; Nogami, S.; Yamada-Fujiwara, M.; Nagai, H.; Yamauchi, K.; Miyashita, H.; Saito, H.; Odashima, K.; Yanagisawa, Y.; et al. Wound Healing Effect of Autologous Fibrin Glue and Polyglycolic Acid Sheets in a Rat Back Skin Defect Model. *Transfus. Apher. Sci.* **2021**, *60*, 103144, doi:10.1016/j.transci.2021.103144.
36. Kinoshita, Y.; Udagawa, H.; Tsutsumi, K.; Ueno, M.; Nakamura, T.; Iizuka, T.; Matsuda, M.; Hashimoto, M.; Sawada, T.; Watanabe, G.; et al. Bacteriological Study of Autologous Cryoprecipitate-derived Fibrin Glue as the Operative Sealant. *Transfus. Med.* **2005**, *15*, 429–433, doi:10.1111/j.1365-3148.2005.00604.x.
37. Bento, C.; Katz, M.; Santos, M.M.M.; Afonso, C.A.M. Striving for Uniformity: A Review on Advances and Challenges To Achieve Uniform Polyethylene Glycol. *Org. Process Res. Dev.* **2024**, *28*, 860–890, doi:10.1021/acs.oprd.3c00428.
38. D'souza, A.A.; Shegokar, R. Polyethylene Glycol (PEG): A Versatile Polymer for Pharmaceutical Applications. *Expert Opin. Drug Deliv.* **2016**, *13*, 1257–1275, doi:10.1080/17425247.2016.1182485.
39. Engebretson, B.; Sikavitsas, V.I. Long-Term In Vivo Effect of Peg Bone Tissue Engineering Scaffolds. *J. Long. Term Eff. Med. Implants* **2012**, *22*, 211–218, doi:10.1615/JLongTermEffMedImplants.2013006244.
40. Koupaei, N.; Karkhaneh, A.; Daliri Joupari, M. Preparation and Characterization of (PCL -crosslinked- PEG)/Hydroxyapatite as Bone Tissue Engineering Scaffolds. *J. Biomed. Mater. Res. A* **2015**, *103*, 3919–3926, doi:10.1002/jbm.a.35513.
41. Tyler, B.; Gullotti, D.; Mangraviti, A.; Utsuki, T.; Brem, H. Polylactic Acid (PLA) Controlled Delivery Carriers for Biomedical Applications. *Adv. Drug Deliv. Rev.* **2016**, *107*, 163–175, doi:10.1016/j.addr.2016.06.018.
42. Grémare, A.; Guduric, V.; Bareille, R.; Heroguez, V.; Latour, S.; L'heureux, N.; Fricain, J.; Catros, S.; Le Nihouannen, D. Characterization of Printed PLA Scaffolds for Bone Tissue Engineering. *J. Biomed. Mater. Res. A* **2018**, *106*, 887–894, doi:10.1002/jbm.a.36289.
43. Middleton, J.C.; Tipton, A.J. Synthetic Biodegradable Polymers as Orthopedic Devices. *Biomaterials* **2000**, *21*, 2335–2346, doi:10.1016/S0142-9612(00)00101-0.
44. Cha, Y.; Pitt, C.G. The Biodegradability of Polyester Blends. *Biomaterials* **1990**, *11*, 108–112, doi:10.1016/0142-9612(90)90124-9.

45. Dash, T.K.; Konkimalla, V.B. Poly-ϵ-Caprolactone Based Formulations for Drug Delivery and Tissue Engineering: A Review. *J. Controlled Release* **2012**, *158*, 15–33, doi:10.1016/j.jconrel.2011.09.064.
46. Sawyer, A.A.; Song, S.J.; Susanto, E.; Chuan, P.; Lam, C.X.F.; Woodruff, M.A.; Hutmacher, D.W.; Cool, S.M. The Stimulation of Healing within a Rat Calvarial Defect by mPCL–TCP/Collagen Scaffolds Loaded with rhBMP-2. *Biomaterials* **2009**, *30*, 2479–2488, doi:10.1016/j.biomaterials.2008.12.055.
47. Jeong, S.I.; Kwon, J.H.; Lim, J.I.; Cho, S.-W.; Jung, Y.; Sung, W.J.; Kim, S.H.; Kim, Y.H.; Lee, Y.M.; Kim, B.-S.; et al. Mechano-Active Tissue Engineering of Vascular Smooth Muscle Using Pulsatile Perfusion Bioreactors and Elastic PLCL Scaffolds. *Biomaterials* **2005**, *26*, 1405–1411, doi:10.1016/j.biomaterials.2004.04.036.
48. Zhan, J.; Singh, A.; Zhang, Z.; Huang, L.; Elisseeff, J.H. Multifunctional Aliphatic Polyester Nanofibers for Tissue Engineering. *Biomatter* **2012**, *2*, 202–212, doi:10.4161/biom.22723.
49. Kim, H.-W.; Knowles, J.C.; Kim, H.-E. Hydroxyapatite/Poly(ε-Caprolactone) Composite Coatings on Hydroxyapatite Porous Bone Scaffold for Drug Delivery. *Biomaterials* **2004**, *25*, 1279–1287, doi:10.1016/j.biomaterials.2003.07.003.
50. Trujillo, N.A.; Popat, K.C. Osteogenic Differentiation of Adipose Derived Stem Cells on Polycaprolactone Nanowire Surfaces. *J. Biomater. Tissue Eng.* **2013**, *3*, 542–553, doi:10.1166/jbt.2013.1112.
51. Helaehil, J.V.; Lourenço, C.B.; Huang, B.; Helaehil, L.V.; De Camargo, I.X.; Chiarotto, G.B.; Santamaria-Jr, M.; Bártolo, P.; Caetano, G.F. In Vivo Investigation of Polymer-Ceramic PCL/HA and PCL/β-TCP 3D Composite Scaffolds and Electrical Stimulation for Bone Regeneration. *Polymers* **2021**, *14*, 65, doi:10.3390/polym14010065.
52. ShiraliPour, F.; Shafiei, S.S.; Nikakhtar, Y. Three-dimensional Porous Poly(E-caprolactone)/Beta-tricalcium Phosphate Microsphere-aggregated Scaffold for Bone Tissue Engineering. *Int. J. Appl. Ceram. Technol.* **2021**, *18*, 1442–1456, doi:10.1111/ijac.13770.
53. Vasita, R.; Katti, D.S. Nanofibers and Their Applications in Tissue Engineering. *Int. J. Nanomedicine* **2006**, *1*, 15–30, doi:10.2147/nano.2006.1.1.15.
54. Melchels, F.P.W.; Feijen, J.; Grijpma, D.W. A Review on Stereolithography and Its Applications in Biomedical Engineering. *Biomaterials* **2010**, *31*, 6121–6130, doi:10.1016/j.biomaterials.2010.04.050.
55. Melchels, F.P.W.; Bertoldi, K.; Gabbrielli, R.; Velders, A.H.; Feijen, J.; Grijpma, D.W. Mathematically Defined Tissue Engineering Scaffold Architectures Prepared by Stereolithography. *Biomaterials* **2010**, *31*, 6909–6916, doi:10.1016/j.biomaterials.2010.05.068.
56. Hersel, U.; Dahmen, C.; Kessler, H. RGD Modified Polymers: Biomaterials for Stimulated Cell Adhesion and Beyond. *Biomaterials* **2003**, *24*, 4385–4415, doi:10.1016/S0142-9612(03)00343-0.
57. Ma, Z.; Gao, C.; Gong, Y.; Shen, J. Cartilage Tissue Engineering PLLA Scaffold with Surface Immobilized Collagen and Basic Fibroblast Growth Factor. *Biomaterials* **2005**, *26*, 1253–1259, doi:10.1016/j.biomaterials.2004.04.031.
58. Siddiqui, N.; Asawa, S.; Birru, B.; Baadhe, R.; Rao, S. PCL-Based Composite Scaffold Matrices for Tissue Engineering Applications. *Mol. Biotechnol.* **2018**, *60*, 506–532, doi:10.1007/s12033-018-0084-5.

59. Krumov, N.; Atanasova, N.; Boyadzhieva, I.; Petrov, K.; Petrova, P. Biodegradation of Poly(ε-Caprolactone): Microorganisms, Enzymes, and Mechanisms. *Int. J. Mol. Sci.* **2025**, *26*, 5826, doi:10.3390/ijms26125826.
60. Guarino, V.; Gentile, G.; Sorrentino, L.; Ambrosio, L. Polycaprolactone: Synthesis, Properties, and Applications. In *Encyclopedia of Polymer Science and Technology*; Mark, H.F., Ed.; Wiley, 2017; pp. 1–36 ISBN 978-1-118-63389-2.
61. Mosca Balma, A.; Pedraza, R.; Orrico, C.; Meinardi, S.; Genova, T.; Gautier Di Confiengo, G.; Faga, M.G.; Roato, I.; Mussano, F. Poly(ε-Caprolactone)/Sodium Bicarbonate/β-Tricalcium Phosphate Composites: Surface Characterization and Early Biological Response. *Materials* **2025**, *18*, 2600, doi:10.3390/ma18112600.
62. Pedraza, R.; Mosca Balma, A.; Roato, I.; Orrico, C.; Genova, T.; Baima, G.; Berta, G.N.; Giura, A.; Ribotta, L.; Duraccio, D.; et al. Early Biological Response to Poly(ε-Caprolactone)/Alumina-Toughened Zirconia Composites Obtained by 3D Printing for Peri-Implant Application. *Polymers* **2024**, *16*, 2521, doi:10.3390/polym16172521.
63. Di Maro, M.; Pedraza, R.; Mosca Balma, A.; Gomez d'Ayala, G.; Poggetto, G.D.; Malucelli, G.; Roato, I.; Duraccio, D.; Mussano, F.; Faga, M.G. Influence of Dry-Mixing and Solvent Casting Blending Techniques on the Mechanical and Biological Behavior of Novel Biocompatible Poly(ε-Caprolactone)/Alumina-Toughened Zirconia Scaffolds Obtained by 3D Printing. *J. Compos. Sci.* **2024**, *8*, 194, doi:10.3390/jcs8060194.
64. Sinha, V.R.; Bansal, K.; Kaushik, R.; Kumria, R.; Trehan, A. Poly-ϵ-Caprolactone Microspheres and Nanospheres: An Overview. *Int. J. Pharm.* **2004**, *278*, 1–23, doi:10.1016/j.ijpharm.2004.01.044.
65. Ragaert, K.; De Somer, F.; Van De Velde, S.; Degrieck, J.; Cardon, L. Methods for Improved Flexural Mechanical Properties of 3D-Plotted PCL-Based Scaffolds for Heart Valve Tissue Engineering. *Stroj. Vestn. – J. Mech. Eng.* **2013**, *59*, 669–676, doi:10.5545/sv-jme.2013.1003.
66. Xu, S.; Xu, S.; Zhou, P.; Cheng, X.; Xie, Y.; Liang, C.; Li, C. Selective Laser Sintering Fabrication of Nano-Hydroxyapatite/Poly-ε-Caprolactone Scaffolds for Bone Tissue Engineering Applications. *Int. J. Nanomedicine* **2013**, 4197, doi:10.2147/IJN.S50685.
67. Mosca Balma, A.; Pedraza, R.; Roato, I.; Orrico, C.; Meinardi, S.; Bertinetti, S.; Genova, T.; Gautier Di Confiengo, G.; Faga, M.G.; Duraccio, D.; et al. Early Biological Response to Poly(ε-Caprolactone) PCL—Bioactive Glass Composites Obtained by 3D Printing as Bone Substitutes. *Polymers* **2025**, *17*, 2229, doi:10.3390/polym17162229.
68. Hutmacher, D.W.; Schantz, T.; Zein, I.; Ng, K.W.; Teoh, S.H.; Tan, K.C. Mechanical Properties and Cell Cultural Response of Polycaprolactone Scaffolds Designed and Fabricated via Fused Deposition Modeling. *J. Biomed. Mater. Res.* **2001**, *55*, 203–216, doi:10.1002/1097-4636(200105)55:2%3C203::AID-JBM1007%3E3.0.CO;2-7.
69. CSIRO Molecular Science, Bag 10, Clayton South MDC, Vic 3169, Australia; Gunatillake, P. Biodegradable Synthetic Polymers for Tissue Engineering. *Eur. Cell. Mater.* **2003**, *5*, 1–16, doi:10.22203/eCM.v005a01.
70. Hao, J.; Yuan, M.; Deng, X. Biodegradable and Biocompatible Nanocomposites of Poly(E-caprolactone) with Hydroxyapatite Nanocrystals: Thermal and

Mechanical Properties. *J. Appl. Polym. Sci.* **2002**, *86*, 676–683, doi:10.1002/app.10955.
71. Lam, C.X.F.; Hutmacher, D.W.; Schantz, J.; Woodruff, M.A.; Teoh, S.H. Evaluation of Polycaprolactone Scaffold Degradation for 6 Months *in Vitro* and *in Vivo*. *J. Biomed. Mater. Res. A* **2009**, *90A*, 906–919, doi:10.1002/jbm.a.32052.
72. Suzuki, M.; Tachibana, Y.; Oba, K.; Takizawa, R.; Kasuya, K. Microbial Degradation of Poly(ε-Caprolactone) in a Coastal Environment. *Polym. Degrad. Stab.* **2018**, *149*, 1–8, doi:10.1016/j.polymdegradstab.2018.01.017.
73. Hutmacher, D.W. Scaffolds in Tissue Engineering Bone and Cartilage. *Biomaterials* **2000**, *21*, 2529–2543, doi:10.1016/S0142-9612(00)00121-6.
74. Prasad, A.; Sankar, M.R.; Katiyar, V. State of Art on Solvent Casting Particulate Leaching Method for Orthopedic ScaffoldsFabrication. *Mater. Today Proc.* **2017**, *4*, 898–907, doi:10.1016/j.matpr.2017.01.101.
75. Sola, A.; Bertacchini, J.; D'Avella, D.; Anselmi, L.; Maraldi, T.; Marmiroli, S.; Messori, M. Development of Solvent-Casting Particulate Leaching (SCPL) Polymer Scaffolds as Improved Three-Dimensional Supports to Mimic the Bone Marrow Niche. *Mater. Sci. Eng. C* **2019**, *96*, 153–165, doi:10.1016/j.msec.2018.10.086.
76. Adel, I.M.; ElMeligy, M.F.; Elkasabgy, N.A. Conventional and Recent Trends of Scaffolds Fabrication: A Superior Mode for Tissue Engineering. *Pharmaceutics* **2022**, *14*, 306, doi:10.3390/pharmaceutics14020306.
77. Chen, Y.; Li, W.; Zhang, C.; Wu, Z.; Liu, J. Recent Developments of Biomaterials for Additive Manufacturing of Bone Scaffolds. *Adv. Healthc. Mater.* **2020**, *9*, 2000724, doi:10.1002/adhm.202000724.
78. Tsai, K.-Y.; Lin, H.-Y.; Chen, Y.-W.; Lin, C.-Y.; Hsu, T.-T.; Kao, C.-T. Laser Sintered Magnesium-Calcium Silicate/Poly-ε-Caprolactone Scaffold for Bone Tissue Engineering. *Materials* **2017**, *10*, 65, doi:10.3390/ma10010065.
79. Gao, Q.; Wang, L.; Wang, S.; Huang, B.; Jing, Y.; Su, J. Bone Marrow Mesenchymal Stromal Cells: Identification, Classification, and Differentiation. *Front. Cell Dev. Biol.* **2022**, *9*, 787118, doi:10.3389/fcell.2021.787118.
80. Mosca Balma, A.; Pedraza, R.; Roato, I.; Orrico, C.; Meinardi, S.; Bertinetti, S.; Genova, T.; Gautier Di Confiengo, G.; Faga, M.G.; Duraccio, D.; et al. Early Biological Response to Poly(ε-Caprolactone) PCL—Bioactive Glass Composites Obtained by 3D Printing as Bone Substitutes. *Polymers* **2025**, *17*, 2229, doi:10.3390/polym17162229.
81. Lindroos, B.; Suuronen, R.; Miettinen, S. The Potential of Adipose Stem Cells in Regenerative Medicine. *Stem Cell Rev. Rep.* **2011**, *7*, 269–291, doi:10.1007/s12015-010-9193-7.
82. Spasovski, D.; Spasovski, V.; Baščarević, Z.; Stojiljković, M.; Vreća, M.; Anđelković, M.; Pavlović, S. Intra-articular Injection of Autologous Adipose-derived Mesenchymal Stem Cells in the Treatment of Knee Osteoarthritis. *J. Gene Med.* **2018**, *20*, e3002, doi:10.1002/jgm.3002.
83. Roato, I.; Belisario, D.C.; Compagno, M.; Verderio, L.; Sighinolfi, A.; Mussano, F.; Genova, T.; Veneziano, F.; Pertici, G.; Perale, G.; et al. Adipose-Derived Stromal Vascular Fraction/Xenohybrid Bone Scaffold: An Alternative Source for Bone Regeneration. *Stem Cells Int.* **2018**, *2018*, 1–11, doi:10.1155/2018/4126379.
84. Kazemi, M.; Azami, M.; Johari, B.; Ahmadzadehzarajabad, M.; Nazari, B.; Kargozar, S.; Hajighasemlou, S.; Mozafari, M.; Soleimani, M.;

Samadikuchaksaraei, A.; et al. Bone Regeneration in Rat Using a Gelatin/Bioactive Glass Nanocomposite Scaffold along with Endothelial Cells (HUVEC s). *Int. J. Appl. Ceram. Technol.* **2018**, *15*, 1427–1438, doi:10.1111/ijac.12907.

85. Liu, X.; Zhao, N.; Liang, H.; Tan, B.; Huang, F.; Hu, H.; Chen, Y.; Wang, G.; Ling, Z.; Liu, C.; et al. Bone Tissue Engineering Scaffolds with HUVECs/hBMSCs Cocultured on 3D-Printed Composite Bioactive Ceramic Scaffolds Promoted Osteogenesis/Angiogenesis. *J. Orthop. Transl.* **2022**, *37*, 152–162, doi:10.1016/j.jot.2022.10.008.
86. Roato, I.; Orrico, C.; Meinardi, S.; Pedraza, R.; Mosca Balma, A.; Baima, G.; Genova, T.; Aimetti, M.; Mussano, F. The Pro-Angiogenic Potential of Periodontal Ligament Stem Cells and Dental Pulp Stem Cells: A Comparative Analysis. *Cells* **2025**, *14*, 864, doi:10.3390/cells14120864.
87. Miola, M.; Verné, E. Bioactive and Antibacterial Glass Powders Doped with Copper by Ion-Exchange in Aqueous Solutions. *Materials* **2016**, *9*, 405, doi:10.3390/ma9060405.
88. Waldner, C.; Hirn, U. Modeling Liquid Penetration into Porous Materials Based on Substrate and Liquid Surface Energies. *J. Colloid Interface Sci.* **2023**, *640*, 445–455, doi:10.1016/j.jcis.2023.02.116.
89. Piatti, E.; Miola, M.; Liverani, L.; Verné, E.; Boccaccini, A.R. Poly(E-caprolactone)/Bioactive Glass Composite Electrospun Fibers for Tissue Engineering Applications. *J. Biomed. Mater. Res. A* **2023**, *111*, 1692–1709, doi:10.1002/jbm.a.37578.
90. Di Maro, M.; Duraccio, D.; Malucelli, G.; Faga, M.G. High Density Polyethylene Composites Containing Alumina-Toughened Zirconia Particles: Mechanical and Tribological Behavior. *Compos. Part B Eng.* **2021**, *217*, 108892, doi:10.1016/j.compositesb.2021.108892.
91. Vecchio, G.; Darcos, V.; Grill, S.L.; Brouillet, F.; Coppel, Y.; Duttine, M.; Pugliara, A.; Combes, C.; Soulié, J. Spray-Dried Ternary Bioactive Glass Microspheres: Direct and Indirect Structural Effects of Copper-Doping on Acellular Degradation Behavior. *Acta Biomater.* **2024**, *181*, 453–468, doi:10.1016/j.actbio.2024.05.003.
92. Piatti, E.; Verné, E.; Miola, M. Synthesis and Characterization of Sol-Gel Bioactive Glass Nanoparticles Doped with Boron and Copper. *Ceram. Int.* **2022**, *48*, 13706–13718, doi:10.1016/j.ceramint.2022.01.252.
93. Duraccio, D.; Strongone, V.; Faga, M.G.; Auriemma, F.; Mussano, F.D.; Genova, T.; Malucelli, G. The Role of Different Dry-Mixing Techniques on the Mechanical and Biological Behavior of UHMWPE/Alumina-Zirconia Composites for Biomedical Applications. *Eur. Polym. J.* **2019**, *120*, 109274, doi:10.1016/j.eurpolymj.2019.109274.
94. Rahaman, M.; Aldalbahi, A.; Bhagabati, P. Preparation/Processing of Polymer–Carbon Composites by Different Techniques. In *Carbon-Containing Polymer Composites*; Rahaman, M., Khastgir, D., Aldalbahi, A.K., Eds.; Springer Series on Polymer and Composite Materials; Springer Singapore: Singapore, 2019; pp. 99–124 ISBN 978-981-13-2687-5.
95. Greiner, R.; Schwarzl, F.R. Thermal Contraction and Volume Relaxation of Amorphous Polymers. *Rheol. Acta* **1984**, *23*, 378–395, doi:10.1007/BF01329190.

96. N. Turner, B.; Strong, R.; A. Gold, S. A Review of Melt Extrusion Additive Manufacturing Processes: I. Process Design and Modeling. *Rapid Prototyp. J.* **2014**, *20*, 192–204, doi:10.1108/RPJ-01-2013-0012.
97. De Avila, E.; De Molon, R.; Palomari Spolidorio, D.; De Assis Mollo Jr., F. Implications of Surface and Bulk Properties of Abutment Implants and Their Degradation in the Health of Periodontal Tissue. *Materials* **2013**, *6*, 5951–5966, doi:10.3390/ma6125951.
98. Shofner, M.L.; Lozano, K.; Rodríguez-Macías, F.J.; Barrera, E.V. Nanofiber-reinforced Polymers Prepared by Fused Deposition Modeling. *J. Appl. Polym. Sci.* **2003**, *89*, 3081–3090, doi:10.1002/app.12496.
99. Vallée, A.; Faga, M.G.; Mussano, F.; Catalano, F.; Tolosano, E.; Carossa, S.; Altruda, F.; Martra, G. Alumina–Zirconia Composites Functionalized with Laminin-1 and Laminin-5 for Dentistry: Effect of Protein Adsorption on Cellular Response. *Colloids Surf. B Biointerfaces* **2014**, *114*, 284–293, doi:10.1016/j.colsurfb.2013.09.053.
100. Dziadek, M.; Dziadek, K.; Checinska, K.; Zagrajczuk, B.; Golda-Cepa, M.; Brzychczy-Wloch, M.; Menaszek, E.; Kopec, A.; Cholewa-Kowalska, K. PCL and PCL/Bioactive Glass Biomaterials as Carriers for Biologically Active Polyphenolic Compounds: Comprehensive Physicochemical and Biological Evaluation. *Bioact. Mater.* **2021**, *6*, 1811–1826, doi:10.1016/j.bioactmat.2020.11.025.
101. Puszka, A.; Sikora, J.W. New Segmented Poly(Thiourethane-Urethane)s Based on Poly(ε-Caprolactone)Diol Soft Segment: Synthesis and Characterization. *Materials* **2022**, *15*, 4940, doi:10.3390/ma15144940.
102. Carvalho, A.; Grenho, L.; Fernandes, M.H.; Daskalova, A.; Trifonov, A.; Buchvarov, I.; Monteiro, F.J. Femtosecond Laser Microstructuring of Alumina Toughened Zirconia for Surface Functionalization of Dental Implants. *Ceram. Int.* **2020**, *46*, 1383–1389, doi:10.1016/j.ceramint.2019.09.101.
103. Kapp, M.; Li, C.; Xu, Z.; Boccaccini, A.R.; Zheng, K. Protein Adsorption on SiO2-CaO Bioactive Glass Nanoparticles with Controllable Ca Content. *Nanomaterials* **2021**, *11*, 561, doi:10.3390/nano11030561.
104. Lim, J.Y.; Shaughnessy, M.C.; Zhou, Z.; Noh, H.; Vogler, E.A.; Donahue, H.J. Surface Energy Effects on Osteoblast Spatial Growth and Mineralization. *Biomaterials* **2008**, *29*, 1776–1784, doi:10.1016/j.biomaterials.2007.12.026.
105. Iwata, R.; Suk-In, P.; Hoven, V.P.; Takahara, A.; Akiyoshi, K.; Iwasaki, Y. Control of Nanobiointerfaces Generated from Well-Defined Biomimetic Polymer Brushes for Protein and Cell Manipulations. *Biomacromolecules* **2004**, *5*, 2308–2314, doi:10.1021/bm049613k.
106. Majhy, B.; Priyadarshini, P.; Sen, A.K. Effect of Surface Energy and Roughness on Cell Adhesion and Growth – Facile Surface Modification for Enhanced Cell Culture. *RSC Adv.* **2021**, *11*, 15467–15476, doi:10.1039/D1RA02402G.
107. Gittens, R.A.; Scheideler, L.; Rupp, F.; Hyzy, S.L.; Geis-Gerstorfer, J.; Schwartz, Z.; Boyan, B.D. A Review on the Wettability of Dental Implant Surfaces II: Biological and Clinical Aspects. *Acta Biomater.* **2014**, *10*, 2907–2918, doi:10.1016/j.actbio.2014.03.032.
108. Khajehmohammadi, M.; Azizi Tafti, R.; Nikukar, H. Effect of Porosity on Mechanical and Biological Properties of Bioprinted Scaffolds. *J. Biomed. Mater. Res. A* **2023**, *111*, 245–260, doi:10.1002/jbm.a.37455.

109. Soufivand, A.A.; Abolfathi, N.; Hashemi, A.; Lee, S.J. The Effect of 3D Printing on the Morphological and Mechanical Properties of Polycaprolactone Filament and Scaffold. *Polym. Adv. Technol.* **2020**, *31*, 1038–1046, doi:10.1002/pat.4838.
110. Carballeira, P.; Haupert, F. Toughening Effects of Titanium Dioxide Nanoparticles on TiO_2 /Epoxy Resin Nanocomposites. *Polym. Compos.* **2010**, *31*, 1241–1246, doi:10.1002/pc.20911.
111. Nukala, S.G.; Kong, I.; Patel, V.I.; Kakarla, A.B.; Kong, W.; Buddrick, O. Development of Biodegradable Composites Using Polycaprolactone and Bamboo Powder. *Polymers* **2022**, *14*, 4169, doi:10.3390/polym14194169.
112. Zuk, P.A.; Zhu, M.; Ashjian, P.; De Ugarte, D.A.; Huang, J.I.; Mizuno, H.; Alfonso, Z.C.; Fraser, J.K.; Benhaim, P.; Hedrick, M.H. Human Adipose Tissue Is a Source of Multipotent Stem Cells. *Mol. Biol. Cell* **2002**, *13*, 4279–4295, doi:10.1091/mbc.e02-02-0105.
113. Ades, E.W.; Candal, F.J.; Swerlick, R.A.; George, V.G.; Summers, Susan.; Bosse, D.C.; Lawley, T.J. HMEC-1: Establishment of an Immortalized Human Microvascular Endothelial Cell Line. *J. Invest. Dermatol.* **1992**, *99*, 683–690, doi:10.1111/1523-1747.ep12613748.
114. Roato, I.; Genova, T.; Duraccio, D.; Ruffinatti, F.A.; Zanin Venturini, D.; Di Maro, M.; Mosca Balma, A.; Pedraza, R.; Petrillo, S.; Chinigò, G.; et al. Mechanical and Biological Characterization of PMMA/Al2O3 Composites for Dental Implant Abutments. *Polymers* **2023**, *15*, 3186, doi:10.3390/polym15153186.
115. Lin, Z.; Cao, Y.; Zou, J.; Zhu, F.; Gao, Y.; Zheng, X.; Wang, H.; Zhang, T.; Wu, T. Improved Osteogenesis and Angiogenesis of a Novel Copper Ions Doped Calcium Phosphate Cement. *Mater. Sci. Eng. C* **2020**, *114*, 111032, doi:10.1016/j.msec.2020.111032.
116. Romero-Sánchez, L.B.; Marí-Beffa, M.; Carrillo, P.; Medina, M.Á.; Díaz-Cuenca, A. Copper-Containing Mesoporous Bioactive Glass Promotes Angiogenesis in an in Vivo Zebrafish Model. *Acta Biomater.* **2018**, *68*, 272–285, doi:10.1016/j.actbio.2017.12.032.
117. Cao, B.; Zheng, Y.; Xi, T.; Zhang, C.; Song, W.; Burugapalli, K.; Yang, H.; Ma, Y. Concentration-Dependent Cytotoxicity of Copper Ions on Mouse Fibroblasts in Vitro: Effects of Copper Ion Release from TCu380A vs TCu220C Intra-Uterine Devices. *Biomed. Microdevices* **2012**, *14*, 709–720, doi:10.1007/s10544-012-9651-x.
118. Akdere, Ö.E.; Shikhaliyeva, İ.; Gümüşderelioğlu, M. Boron Mediated 2D and 3D Cultures of Adipose Derived Mesenchymal Stem Cells. *Cytotechnology* **2019**, *71*, 611–622, doi:10.1007/s10616-019-00310-9.
119. Renaud, M.; Bousquet, P.; Macias, G.; Rochefort, G.Y.; Durand, J.-O.; Marsal, L.F.; Cuisinier, F.; Cunin, F.; Collart-Dutilleul, P.-Y. Allogenic Stem Cells Carried by Porous Silicon Scaffolds for Active Bone Regeneration In Vivo. *Bioengineering* **2023**, *10*, 852, doi:10.3390/bioengineering10070852.
120. Collart-Dutilleul, P.-Y.; Secret, E.; Panayotov, I.; Deville De Périère, D.; Martín-Palma, R.J.; Torres-Costa, V.; Martin, M.; Gergely, C.; Durand, J.-O.; Cunin, F.; et al. Adhesion and Proliferation of Human Mesenchymal Stem Cells from Dental Pulp on Porous Silicon Scaffolds. *ACS Appl. Mater. Interfaces* **2014**, *6*, 1719–1728, doi:10.1021/am4046316.
121. Martinez, M.A.F.; Balderrama, Í.D.F.; Karam, P.S.B.H.; De Oliveira, R.C.; De Oliveira, F.A.; Grandini, C.R.; Vicente, F.B.; Stavropoulos, A.; Zangrando,

M.S.R.; Sant'Ana, A.C.P. Surface Roughness of Titanium Disks Influences the Adhesion, Proliferation and Differentiation of Osteogenic Properties Derived from Human. *Int. J. Implant Dent.* **2020**, *6*, 46, doi:10.1186/s40729-020-00243-5.

122. Olivares-Navarrete, R.; Hyzy, S.L.; Berg, M.E.; Schneider, J.M.; Hotchkiss, K.; Schwartz, Z.; Boyan, B.D. Osteoblast Lineage Cells Can Discriminate Microscale Topographic Features on Titanium–Aluminum–Vanadium Surfaces. *Ann. Biomed. Eng.* **2014**, *42*, 2551–2561, doi:10.1007/s10439-014-1108-3.
123. Saberian, E.; Jenča, A.; Seyfaddini, R.; Jenča, A.; Zare-Zardini, H.; Petrášová, A.; Jenčová, J. Comparative Analysis of Osteoblastic Responses to Titanium and Alumina-Toughened Zirconia Implants: An In Vitro Study. *Biomolecules* **2024**, *14*, 719, doi:10.3390/biom14060719.
124. Nazarov, D.; Ezhov, I.; Yudintceva, N.; Shevtsov, M.; Rudakova, A.; Kalganov, V.; Tolmachev, V.; Zharova, Y.; Lutakov, O.; Kraeva, L.; et al. Antibacterial and Osteogenic Properties of Ag Nanoparticles and Ag/TiO2 Nanostructures Prepared by Atomic Layer Deposition. *J. Funct. Biomater.* **2022**, *13*, 62, doi:10.3390/jfb13020062.
125. Riivari, S.; Närvä, E.; Kangasniemi, I.; Willberg, J.; Närhi, T. Epithelial Cell Attachment and Adhesion Protein Expression on Novel in Sol TiO_2 Coated Zirconia and Titanium Alloy Surfaces. *J. Biomed. Mater. Res. B Appl. Biomater.* **2022**, *110*, 2533–2541, doi:10.1002/jbm.b.35111.